Universidad Carlos III de Madrid

Size Effects in LiF Plasticity: New Insights into the Lattice Resistance Contribution

Rafael Soler Arnedo

Supervisors:

Jon Mikel Molina Aldareguía

Javier Segurado Escudero

A thesis submitted for the degree of Doctor of Philosophy

Department of Materials Science and Engineering and Chemical Engineering

June 2014

Universidad
Carlos III de Madrid
www.uc3m.es

Tesis Doctoral

Size Effects in LiF Plasticity: New Insights into the Lattice Resistance Contribution

Autor: Rafael Soler Arnedo

Directores: Jon Mikel Molina Aldareguía
Javier Segurado Escudero

Firma del Tribunal Calificador:

Firma:

Presidente: Javier Gil Sevillano

Vocal: William J. Clegg

Secretario: Elena Gordo Odériz

Calificación:

Leganés, 16 de Junio de 2014

A mis padres

I would like to describe a field, in which little has been done, but in which an enormous amount can be done in principle. This field is not quite the same as the others in that it will not tell us much of fundamental physics (in the sense of, "What are the strange particles?") but it is more like solid-state physics in the sense that it might tell us much of great interest about the strange phenomena that occur in complex situations. Furthermore, a point that is most important is that it would have an enormous number of technical applications.

What I want to talk about is the problem of manipulating and controlling things on a small scale.

As soon as I mention this, people tell me about miniaturization, and how far it has progressed today. They tell me about electric motors that are the size of the nail on your small finger. And there is a device on the market, they tell me, by which you can write the Lord's Prayer on the head of a pin. But that's nothing; that's the most primitive, halting step in the direction I intend to discuss. It is a staggeringly small world that is below. In the year 2000, when they look back at this age, they will wonder why it was not until the year 1960 that anybody began seriously to move in this direction.

"There is Plenty of Room at the Bottom.
An Invitation to Enter a New Field of Physics"
Transcript of a talk given by Richard P. Feynman at the Annual meeting of the American Physical Society at California Institute of Technology (Caltech) on December 29^{th}, 1959.

Acknowledgements

I would like to express my most sincere gratitude to my supervisors, Dr. Jon Molina-Aldareguía and Dr. Javier Segurado. Thank you both, for all your help and support, for your valuable guidance, scholarly inputs and consistent encouragement. It has been a pleasure working with you. You made me discover my passion for science. Muchísimas gracias a los dos.

I would also like to extend my acknowledgement to Prof. Javier Llorca, director at IMDEA Materials Institute, for giving me the opportunity to joint a leading research institution and provide the resources to successfully carry out my research. I would also like to acknowledge the financial support of the Spanish Ministry of Science and Innovation through the program Size Matters (MAT2009-14396).

My sincere gratitude to Dr. Jeffrey M. Wheeler and Prof. Johann Michler for our fruitful collaboration on the elevated temperature experiments. Of justice is to acknowledge their co-authorship in Chapter 5. My thanks to Dr. Rosa I. Merino and Prof. Victor M. Orera for providing us the eutectic samples without which this thesis would not have been possible. I also thank Dr. Christoph Kirchlechner and Prof. Gehard Dehm for hosting me during my stay at The Erich Schmid Institute of Materials Science (ESI). Unfortunately, our exciting collaboration was finally not included in this thesis due to time constraints.

I would also like to express my most sincere gratitude to all the members of IMDEA Materials Institute, especially those of the Micro- and Nano-mechanics research group, for being excellent professionals and

better colleagues. Special thanks go to my fellow PhD students for the stimulating discussions, for the sleepless nights we were working together before deadlines, and for all the fun we have had in the last years. Thank you all.

Muchísimas gracias también a mi familia, por vuestro apoyo incondicional. A mi hermano, por enseñarme siempre el camino. A mi hermana, por cuidarme y animarme. A Meri, mi amor, por hacerme feliz.

Y finalmente a mis padres, porque sin duda son ellos los que más merecen mi agradecimiento. Mis logros son solo una pequeña muestra de los vuestros.

Resumen

Estudios previos del comportamiento mecánico de micropilares monocristalinos sometidos a compresión sugieren que la influencia del tamaño de la muestra en la tensión de fluencia del material es dependiente del tipo de material. El presente trabajo de investigación analiza el papel de la resistencia intrínsica de la red cristalina, una constante dependiente del tipo de material, en dicha dependencia. En particular, el principal objetivo de esta tesis es intentar caracterizar individualmente los distintos sistemas de deslizamiento de un sistema cristalino dado mediante ensayos de microcompresión y evaluar cómo el efecto del tamaño varía en función de la tensión crítica de fluencia de cada sistema de deslizamiento. Para ello, se eligió como material modelo el LiF. El LiF presenta una marcada anisotropía plástica, resultado de la gran diferencia en tensiones críticas de fluencia entre sus dos familias de sistemas de deslizamiento, el "blando" $\{110\}\langle 110\rangle$ y el "duro" $\{100\}\langle 110\rangle$. Además, permite activar independientemente cada familia de sistemas de deslizamiento a través del control de la orientación cristalográfica del micropilar. Inicialmente, la plasticidad del LiF se evaluó en función de la orientación cristalográfica del micropilar y la correspondiente activación de sus sistemas de deslizamiento por medio de simulaciones de Plasticidad Cristalina en Elementos Finitos (PCEF). El estudio se centró en el comportamiento plástico de dos orientaciones cristalográficas bien diferenciadas, la orientación [100] y la orientación [111], las cuales unicamente activan los sitemas de deslizamiento "blandos" y "duros", respectivamente. Además, se evaluó la influencia de tres posibles errores experiementales de medida asociados con el correcto alineamiento de los micropi-

lares: inclinación inicial del pilar, desorientación cristalográfica del pilar, y contacto irregular entre la punta plana del nanoindentador y el pilar; concluyendo que, a diferencia de los micropilares orientados en la dirección [100], los micropilares orientados en la dirección [111] son extremadamente sensibles a posibles imprecisiones introducidas durante la realización de los experimentos, y por tanto, a presentar errores de medida en los datos. También se estudió experimentalmente la resistencia a compresion de micropilares monocristalinos de LiF orientados en la dirección [111]. Micropilares de diferente diámetro (en el rango entre 1 y 5 μm) fueron obtenidos mediante un ataque químico de la matriz en compuestos eutécticos de NaCl-LiF y KCl-LiF, solidificados direccionalmente. Los ensayos iniciales de microcompresión realizados a temperatura ambiente no mostraron ningun efecto significativo del tamaño del pilar en la tensión de fluencia. Estos resultados fueron contrastados con un estudio previo de micropilares monocristalinos de LiF orientados en la dirección [100], que monstraron un fuerte efecto del tamaño en la tensión de fluencia (Nadgorny et al., 2008), confirmando observaciones previas que sugierían que la magnitud del efecto del tamaño en la tensión de fluencia escala con la magnitud de la resistencia intrínseca de la red cristalina. Para evaluar la influencia del daño inducido por la irradiación de iones asociada con la fabricación de micropilares por medio de microscopía de haces enfocados (método convencional para la fabricación de pilares en la escala micrométrica), varios de nuestros pilares orientados en la dirección [111] fueron expuestos a una irradiación altamente energética de iones de Ga^+. El principal objetivo fue evaluar el efecto de la irradiación de iones en la respuesta mecánica. La exposición a irradiación de iones condujo a incrementos de aproximadamente 30% en la resistencia a fluencia y en la resistencia máxima a compresión. Sin embargo, en esta ocasión tampoco se observó un efecto significativo del tamaño de la muestra en la tensión de fluencia del material. El rol de la resistencia intrínseca de la red fue analizado en mayor profundidad mediante ensayos de microcompresión a altas temperaturas,

llegando a temperaturas de hasta 250 °C. Los resultados muestran que los efectos de tamaño en micropilares de LiF orientados en la dirección [111] son extremadamente dependientes de la temperatura. Esta dependencia de los efectos tamaño con la temperatura se analizó mediante la comparación con la resistencia equivalente de LiF orientado en la dirección [111] para una muestra macroscópica o "bulk", confirmando que el efecto de tamaño aumenta a medida que la tensión de fluencia "bulk" disminuye. Finalmente, estas observaciones experimentales fueron comparadas con la tensión teórica necesaria para activar fuentes de dislocaciones truncadas (Parthasarathy et al., 2007), mostrando experimentalmente, por primera vez y en el mismo material, la validez del modelo para estimar el rol de la resistencia de la red cristalina en los efectos tamaño de pequeños monocristales.

Abstract

Previous studies on the mechanical response under compression of single-crystal micropillars suggest that the effect of sample size on the flow stress is material dependent. This investigation addresses the role of the intrinsic lattice resistance of the material on this dependency. In particular, the objective of this study is to ascertain whether different slip systems can be characterized individually using micro-compression and to see how size effects differ as a function of the bulk critical resolved shear stress of the operative slip system. For this, LiF was chosen as the model material as it presents a marked plastic anisotropy as a result of the large difference in the critical resolved shear stress between the "soft" $\{110\}\langle 110\rangle$ and the "hard" $\{100\}\langle 110\rangle$ active slip systems, and because their operative slip systems depend strongly on the micropillar crystallographic orientation. Plasticity in LiF was evaluated in terms of crystal orientation and slip system activation by means of crystal plasticity finite element simulations, focusing on the distinctive response of two micropillar crystallographic orientations, the [100]- and the [111]-orientation, where only the "soft" and the "hard" slip systems activate, respectively. Furthermore, the influence of three potential sources of experimental uncertainties associated with the alignment of the micropillars were assessed: geometrical tilts, lattice rotations, and misalignments between the surfaces of the flat punch and the head of the pillar, concluding that micropillars oriented in the [111]-direction are extremely sensitive to experimental uncertainties, thus to have artifacts present in the data. The compressive response of LiF single-crystal micropillars oriented in the [111]-direction was also studied experimentally.

Micropillars of different diameter (in the range 1-5 μm) were obtained by etching the matrix away in directionally-solidified NaCl-LiF and KCl-LiF eutectic compounds. Initial micro-compression tests carried out at room temperature did not show any significant effect of the micropillar diameter on the flow stress. These results were discussed to the light of previous results in LiF in the [100]-orientation, that showed a strong size effects on the flow stress (Nadgorny et al., 2008), confirming previous observations that suggest that the extent of the size effect on the flow stress scales with the intrinsic lattice resistance of the material. To evaluate the effect of the ion-irradiation induced damage associated with focused ion beam (FIB) fabrication of the micropillars (the conventional method to fabricate micropillars), selected [111]-oriented pillars were exposed to high-energy Ga^+ ions to ascertain the effect of ion irradiation on the mechanical response. Ion irradiation led to an increase of approximately 30% in the yield strength and the maximum compressive strength but no effect of the micropillar diameter on flow stress was found either. The role of the lattice resistance was further analyzed by performing elevated temperature micro-compression tests at temperatures up to 250 °C. Results showed that size effects on LiF [111]-oriented micropillars are strongly dependent on temperature. It was demonstrated that the size effect observed during micropillar compression comes about as a result of the relative weights of the size-independent (lattice resistance plus forest hardening) and size-dependent (operation of single arm dislocation sources) contributions to strength. The former dominated at room temperature (and no size effect was found) while both were of the same order at 250 °C for the micropillar diameters studied, leading to a strong size effect. Thus, the role of the lattice resistance on the size effect of micrometer-size single-crystals was demonstrated unambiguously for this first time. This result rationalizes the different values of power-law exponent for the size effect found in the literature for FCC and BCC metals as well as covalent and ionic solids.

Contents

List of Abbreviations and Acronyms

AFM	Atomic Force Microscope
BCC	Body Center Cubic
BSE	Back Scatter Electrons
CPFE	Crystal Plasticity Finite Element
CRSS	Critical Resolved Shear Stress
CSIC	Centro Superior de Investigaciones Científicas
CTT	Critical Thickness Theory
DSE	Directionally Solidify Eutectic
EPD	Etch Pit Density
FCC	Face Center Cubic
FEM	Finite Element Model
FE-SEM	Field Emission Secondary Electron Microscope
FIB	Focused Ion Beam
GCTT	Geometric Critical Thickness Theory
GND	Geometric Necessary Dislocations
HCP	Hexagonal Close Packed

LMIS	Liquid-Metal Ion Source
MEMS	Micro Electro Mechanical Systems
NEMS	Nano Electro Mechanical Systems
PID	Proportional Integral Derivative
SE	Secondary Electrons
SEM	Scanning Electron Microscope
SGP	Strain Gradient Plasticity
SSD	Statistically Stored Dislocations
TEM	Transmission Electron Microscope
UMAT	User Material subroutine

List of Figures

List of Tables

Nomenclature

Indexes α and β denote given slip systems.

A_0	Initial cross-sectional area
b	Burgers' vector
C	Micropillar compliance
C_{ij}	Elastic constants
ϵ	Strain
$\dot{\epsilon}$	Strain rate
E	Elastic modulus
$\mathbf{F}$	Deformation gradient
$\mathbf{F}_e$	Elastic deformation gradient
$\mathbf{F}_p$	Plastic deformation gradient
G	Shear modulus
$\dot{\gamma}$	Shear strain rate
$\dot{\gamma}_0$	Reference shear strain rate
Γ	Accumulated shear strain rate
$h_{\alpha\alpha}$	Hardening modulus
h_0	Initial hardening modulus
$\mathbf{L}$	Velocity gradient

$\mathbf{L}_p$	Plastic velocity gradient
L_0	Initial gauge length
$\bar{\lambda}_{max}$	Statistical average length of the weakest single arm dislocation source
$\mathbf{m}^\alpha$	Unit vector normal to the slip plane
m	Strain rate sensitivity exponent
μ	Anisotropic shear modulus
$q_{\alpha\beta}$	Latent hardening constant
ρ_m	Mobile dislocation density
ρ_{tot}	Total dislocation density
$\mathbf{s}^\alpha$	Unit vector in the slip direction
σ	Stress
τ	Shear stress
τ_{CRSS}	Critical resolved shear stress
τ_p	Peierls' stress
τ_0	Intrinsic bulk lattice resistance
τ_{bulk}	Bulk flow stress
τ_{size}	Size dependent flow stress
v	Average dislocation velocity
v	Attempt frequency
V	Activation volume

1 Introduction

1.1 Motivation for the Study of Mechanical Properties of Materials in Small Dimensions

Miniaturized mechanical devices are nowadays common in many of the technologies that we use on our daily lives, and they are certain to play an even more important role in future. Society is becoming more and more dependent on technology and continuously demands more sophisticated engineering devices and structures on a smaller and smaller scale. Nowadays, sensors and actuators based on MEMS and NEMS technologies are present in most electronic devices, from cell phones to cars, with some devices now reaching design specifications of just a few nanometers. The design, fabrication and operation of such a small devices and structures call for an understanding of the mechanical properties of materials at these small length scales, not only because these functional devices

are primarily load bearing structures, but also because mechanical durability and reliability are required for their successful operation.

In the last two decades, we have seen an explosion of research on the mechanical properties of materials in small dimensions. At the macroscale, the mechanical properties of materials are described by classical mechanics, that are independent of the size of the specimen. However, when the scale of the specimen is comparable to the microstructural features that control the mechanical properties, the classical laws break down and do not provide a correct description of the mechanical behaviour of materials. The development of new experimental methods to perform quantitative nano-/micromechanical tests for complex and miniaturized materials, together with the used of advanced microstructure characterization techniques to unravel the underlying deformation mechanisms from the micrometer level down to atomic dimensions, are fundamental aspects that have contributed to characterize this mechanical properties of the materials in these small dimensions, and thus to provide a rationale to establish new material laws valid in the micro- and nanoscale.

The seminal work of Uchic et al. (2004), which reported for the first time on the influence of the sample dimensions on the overall slip resistance of a material, supposed a major breakthrought on our understanding of the plastic behaviour of crystalline materials in confined dimensions. By developing a new methodology for performing uniaxial compression tests on samples having micron-size dimensions, the authors showed how the overall sample dimensions artificially limit the length scales available for plastic processes, resulting in a dramatic change in material strength as a function of the sample dimensions (see Figure 1.1). Since the publication of their pioneering work, many developments on the plastic behaviour of crystalline materials have followed, and nowadays plasticity mechanisms in the micron- and submicron scale are better understood, though still more definitive studies have to come in order to establish new material laws for the local and global mechanical behaviour.

For the future, engineering design of miniaturized devices and structures is beginning to demand structure-dependent models to enable a quicker transition of novel advanced materials. These models are envisaged to account for the variations in microstructural features and/or the geometric scales and provide

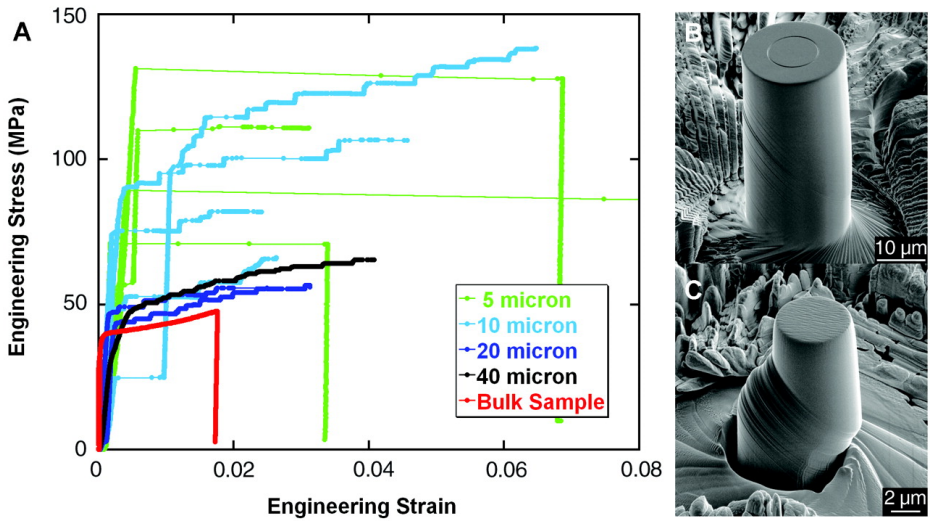

Figure 1.1: Mechanical behavior at room temperature for pure Ni microsamples having a ⟨134⟩ orientation. (A) Stress-strain curves for microsamples ranging in size from 40 to 5 μm in diameter, as well as the stress-strain curve for a bulk single crystal. (B) A scanning electron micrograph (SEM) image of a 20 μm diameter microsample tested to ∼4% strain. (C) A SEM image of 5 μm diameter microsample after testing, where the sample achieved ∼19% strain during a rapid burst of deformation that occurred in less than 0.2 sec (Uchic et al., 2004).

representations of their effects for engineering design. This probably is, from an engineering perspective, the main goal the study of mechanical properties of materials in small dimensions should ultimately contribute to address.

Nevertheless, the study of mechanical properties of materials in small dimensions has demonstrated useful in other, very different, applications. A good example is the work of Schaedler et al. (2011), where they proposed a novel methodology to fabricate a lattice of interconnected hollow-tubes with a wall thickness of ∼100 nm (see Figure 1.2). The material's architecture allowed unprecedented mechanical behavior for a metal, including a complete recovery from compression exceeding 50% strain and an extraordinarily high energy absorption, all with a density of only 0.9 mg/cm^3 (the worlds lightest material at that time). These unique mechanical properties are directly related to the

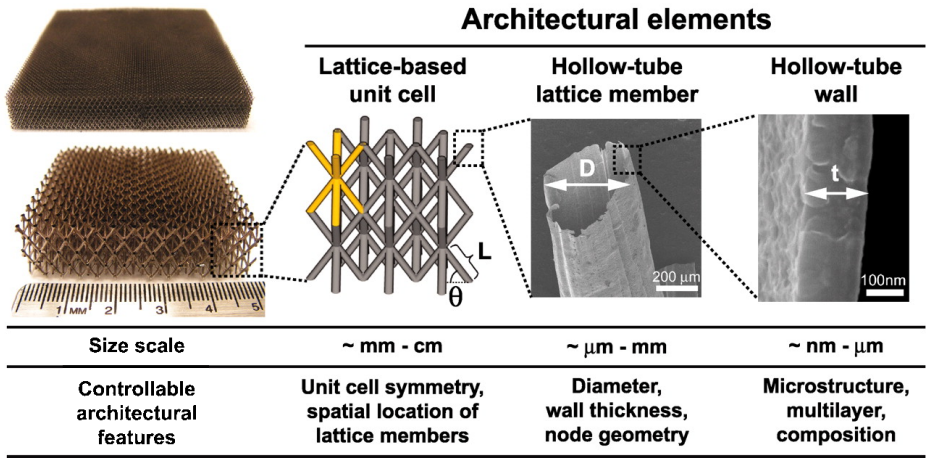

Figure 1.2: Cellular architecture of ultralight microlattices. Images of two as-fabricated Ni-P microlattices along with a breakdown of the relevant architectural elements (adapted from Schaedler et al. (2011)).

critical dimensions of some of the architectural elements, i.e. the thickness of the hollow-tube walls, that strengthen the material as the dimensions are reduced to the nanoscale. This novel celular material could be potentially used for battery electrodes and acoustic, vibration or shock energy absorption. This is just one example of the many scientific and technological developments the study of micro- and nano-mechanics will most provably contribute to achieve in the upcoming future.

1.2 "Smaller is Stronger": The Effect of Size in Material's Strength

1.2.1 Intrinsic Size Effects

Intrinsic size effects arise from microstructural, or intrinsic, constraints. It is well known that the mechanical properties of a material can be improved by modifying

its microstructure. Through the development and optimization of engineering processes, i.e. work hardening, solid solution hardening, precipitation, or grain size refinement, the strength of metallic alloys has been demonstrated to increase more than two orders of magnitude. Independently of the approach followed, strengthening in cristalline solids is achieved by increasing the density of obstacles that block or retard dislocations motion. The characteristic length scale of the obstacle, or particular microstructure feature, i.e. the precipitates spacing or the grain size, preventing dislocation motion has been proven to strongly influence the overall strength of the material. This type of strength-dependency with a characteristic microstructural length scale is a prime example of a size effect governed by an intrinsic constrain. The main strengthening mechanisms that give rise intrinsic size effect in crystalline solids are reviewed below.

Particle Strengthening

Particle strengthening is a method of strengthening materials by introducing obstacles to the motion of dislocations. It is based on the observation that obstacles impede dislocation movement and that the spacing between adjacent obstacles have an effect on how easily dislocations move across the crystal. So, by changing the obstacle spacing one can influence dislocation movement and yield strength.

Dislocations are line defects that are naturally present in the crystal. Dislocations are characterized by its Burgers' vector b that measures the plastic distortion introduced by the dislocation movement. Every single dislocation defect originates an elastic distortion in the lattice. Because of the lattice misfit, increasing the line length of a dislocation increases the overall energy of the system. To minimize this elastic lattice distortion, a line tension tends to straightened the dislocation. This line tension may be defined as the increase in energy per unit increase in length of a dislocation line. Assuming elastic isotropy, this line tension has the simplified form

$$T = \frac{Gb^2}{2} \tag{1.1}$$

where G is the shear modulus.

Let us consider now a dislocation that has attained a semicircular shape. If a shear stress τ is applied into the slip plane then a force τbl , where l is the initial dislocation length, is exerted on the dislocation line as a result of the shear stress. This force acts perpendicularly to the line, inducing the dislocation to lengthen and curve into an arc. For the dislocation to reach the semicircular shape, equilibrium forces between the line tension and the bending force must be satisfied, such that $2\,T = \tau bl$. We can now solve for the maximum bending, or minimum curvature diameter, a curved dislocation (or a dislocation loop) can adopt for a given shear stress. This diameter is given by

$$d(\tau) = \frac{Gb}{\tau} \tag{1.2}$$

Consider now a dislocation that is approaching an array of impenetrable obstacles. For the dislocation to pass through them it has to bow between the obstacles (see Figure 1.3). According to Orowan's formulation (Orowan, 1947) plastic deformation due to long range dislocation motion requires dislocations to fully bypass the obstacles. The bypass condition is achieved when the applied shear stress is sufficient to bow a dislocation to a diameter equal to the mean obstacle spacing L. Thus

$$d(\tau) = L \tag{1.3}$$

It is then straigth forward to obtain the bypass stress as a funtion of the obstacle spacing by combaining equations 1.2 and 1.3.

$$\tau = \frac{Gb}{L} \tag{1.4}$$

Equation 1.4 reflects how the flow stress of a dislocation-dominated material can be significantly altered by modifying a microstructural, or intrinsic, length scale, the obstacle spacing L. The formulation developed here assumes immobile

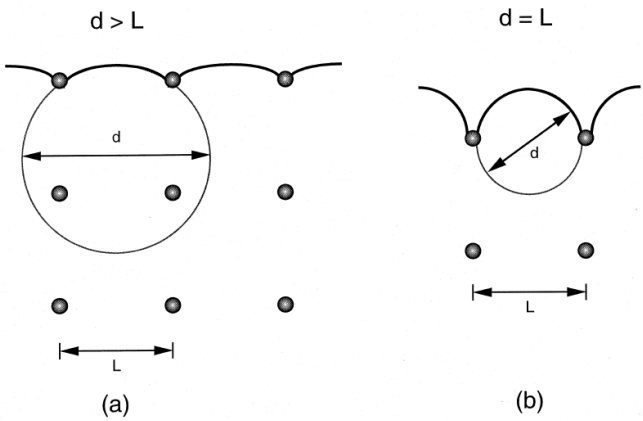

Figure 1.3: The onset of plastic flow controlled by obstacles, seen as a size effect. The intrinsic size parameter is the mean obstacle spacing L. Dislocatin loop diameter d is inversaly proportional to the shear stress (equation 1.2). Case a: $d > L$, dislocation does not propagate; case b: $d = L$, dislocation propagates (Arzt, 1998).

impenetrable obstacles, i.e. incoherent precipitates. To account for other type of non-impenetrable obstacles, i.e. forest dislocations that thread through the slip plane, solute atoms, or small second-phase precipitates, more sophisticated treatments need to be considered (Brown and Ham, 1971; Taylor, 1934). Nevertheless, they are all based on the same basic constitutive equations developed here.

Grain Size Effect - Hall-Petch Relation

Grain size refinement, also known as Hall-Petch effect, is a method of increasing the strength of polycrystalline materials by decreasing the average grain size. In the early 1950s Hall (Hall, 1951) and Petch (Petch, 1953) established in independently conducted works the same relationship between the grain size and the yield strength of the material. They found that the yield strength σ_y of polycrystalline iron and steel materials varies inversely with the square root of the mean grain diameter d. This empirical relationship, named after both scientists as the Hall-Petch effect, is classically expressed as

$$\sigma_y = \sigma_0 + kd^{-1/2} \tag{1.5}$$

where σ_0 is the friction stress and k is the Hall-Petch constant. k is considered to be a material-dependent constant, as observed elsewhere (Hansen, 2004; Janssen et al., 2006). However, the real physical mechanism underlaying this relationship remains unclear. Plastic deformation in polycrystalline materials involves a wide range of interaction phenomena between dislocations and grain boundaries, which are still subject of extensive research. Several physically-based models have been proposed in the literature: the dislocation pile-up model (Hall, 1951); the grain boundary source model (Li, 1963); the slip distance model (Chia et al., 2005); and the geometrically necessary dislocation (GND) model (Ashby, 1970).

The most commonly cited explanation of the grain size effect is the dislocation pile-up model. It is based on the observation that grain boundaries act as natural barriers to the movement of dislocations and that the amount of dislocations trapped within a grain directly influence how easily dislocations can cross grain boundaries and propagate into an adjacent grain. Let us consider a grain where a shear stress is acting into an slip system with sufficiency of mobile dislocations. Dislocations will move along the slip plane until they reach a grain boundary, where dislocations are blocked due to the barrier generated by the lattice orientation mismatch between adjacent crystals. As plastic activity takes place, more dislocations will pile-up against the grain boundary. Glissile dislocation generate repulsive stress fields on each other, so the more dislocations accumulate at the boundary the higher the repulsive force becomes, acting as a driving force to reduce the energetic barrier for propagation across the boundary. By decreasing the grain size the possible amount of dislocations pilling-up decreases, which increases the shear stress required to propagate a dislocation into an adjacent grain (see Figure 1.4). The higher the stress required to move a dislocation the higher the overall yield strength. Thus, by decreasing the mean grain size (a microstructural or intrinsic length scale) the yield strength of the material increases.

The Hall-Petch relation is well obeyed by a variety of structural alloys over

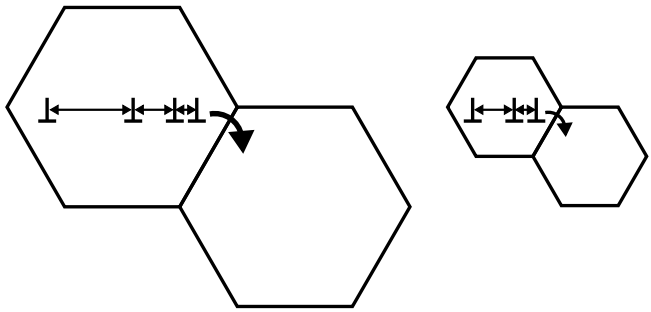

Figure 1.4: Dislocation pile-up, seen as a size effect. Larger grains are capable of holding more dislocation pile-ups, generating a higher driving force for dislocations to move into adjacent grains. Thus less force is required to move a dislocation from a larger than from a smaller grain, leading materials with smaller grains to exhibit higher yield stress.

several orders of magnitude in grain sizes (Meyers and Chawla, 1984). However, the relation breaks down for the finest grain sizes, as discussed in the following section, where alternative plastic deformation mechanisms dominate.

Inverse Hall-Petch Effect

The reverse or inverse Hall-Petch effect determines that, below a certain grain size threshold, the yield strength decreases with the grain size. It has been long theorized that there must be a lower limit in grain size for the Hall-Petch effect. It is inevitable that equation 1.5 must break down for very small grains. Otherwise, materials will become infinitely strong if the grains are made infinitely small. Chokshi et al. (1989) first reported experimental evidence of such a break down in the Hall-Petch relation. They found nanocrystalline Cu to manifest softening with decreased grain size below a critical grain size. Since then, similar observations have been made for different materials (El-Sherik et al., 1992; Fougere et al., 1992; Gertsman et al., 1994; Giga et al., 2006; Lu et al., 1990; Nieman et al., 1989; Sanders et al., 1997; Schuh et al., 2002). Nowadays, the so-called "inverse" Hall-Petch relation is a well established phenomenon.

However, the specific plasticity mechanisms operating in nanocrystalline ma-

terials are still controversial. A number of competing explanations have been proposed for the inverse Hall-Petch effect, like grain rotation, grain-boundary migration, or grain-boundary sliding (Farkas et al., 2008; Gianola et al., 2006, 2008a,b; Ke et al., 1995; Legros et al., 2008; Van Swygenhoven and Derlet, 2001; Van Swygenhoven et al., 2002; Wang et al., 2008; Yamakov et al., 2002; Yin and Whang, 2005). They all rely on the assumption that at such a small scale, grains can not longer accommodate multiple dislocations. Thus, alternative plastic deformation mechanisms based on the activation of grain boundary-mediated deformation processes need to take place. Regardless of the plastic deformation mechanism, there is a general agreement about the grain size regimes where dislocation-mediated versus grain-boundary mechanisms prevail, as shown in Figure 1.5. This transition regimen can initiate at a considerably large grain size $<$100 nm, but is usually expected to appear somewhere between 40-20 nm.

Although the plasticity mechanisms that give rise to the inverse Hall-Petch relation are still subject of rigorous investigations, the decrease in yield strength with grain size in nanocrystalline metals is nowadays a well established phenomenon. This "inverse" size effect regime must necessarily be controlled by a sub-grain-level length scale, i.e. the grain boundary thickness, but understanding of size effects at these small scales is not yet mature and is currently a topic of discussion.

1.2.2 Extrinsic Size Effects

Extrinsic size effects arise from dimensional, or extrinsic constraints. It has been recently seen that the strength of a material can be significantly enhanced when small volumes are strained. These extrinsic constraints might be due to small sample dimensions, i.e. thin film thickness, where plastic deformation mechanisms such as dislocation motion are affected by the presence of a surface or interface, or due to small strained volume, i.e. nanoindentation, where the dimensional constraint arises from the testing system. Common strengthening mechanisms caused by dimensional, or extrinsic, constraints in crystalline solids are reviewed below.

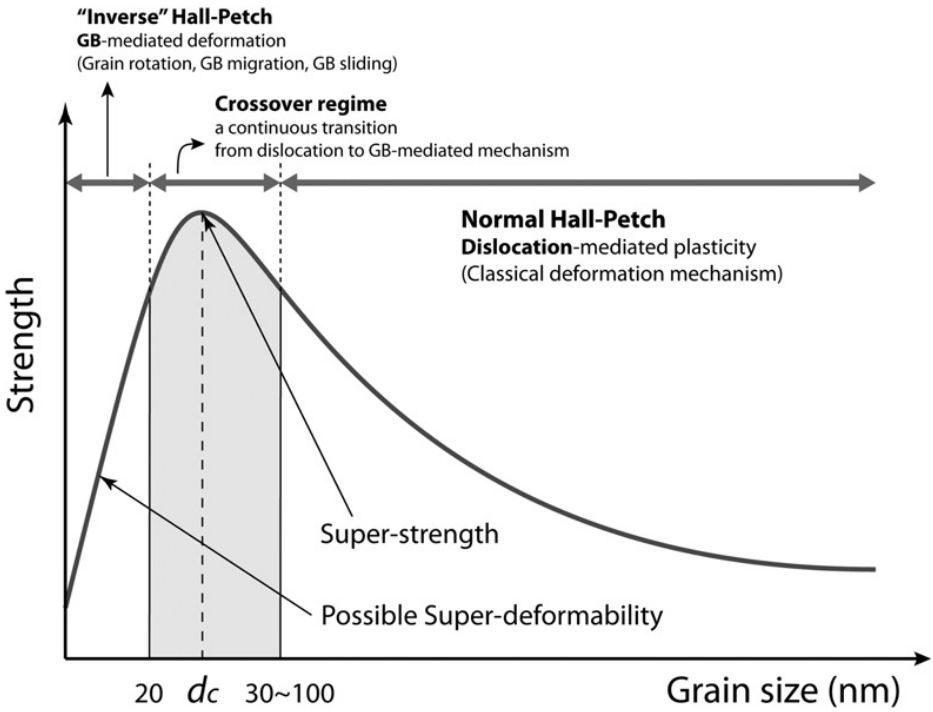

Figure 1.5: Strength of polycrystalline materials as a function of grain size: Hall-Petch relation and transition to "inverse" Hall-Petch (Greer and De Hosson, 2011).

Thin Films: The Thickness Effect

Thin films are, by definition, materials in which one dimension, the thickness, is several orders of magnitude smaller than the other two. Commonly, anything from fractions of a nanometer to several micrometers in thickness can be considered a thin film. The dimensional constraint, rather than the microstructure, has been found to control the mechanical properties of thin films. Yield strength in films with less than a micron in thickness have shown to scale inversely with the film thickness. Thus, it is the thin film thickness H the relevant size parameter controlling size effect in thin films.

It was in 1989 when Nix (1989) first applied the critical thickness theory

(CTT), originally develop by Matthews and Blakeslee (1974, 1975) to explain growth conditions in epitaxial semiconductor thin films, to characterize the mechanical properties of thin films. His theory predicted metal thin film strength to vary inversely with film thickness. The theory relays on the misfit dislocation channeling theory early introduced by Frank and van der Merwe (1949).

Consider a single-crystalline film attached to a bulk substrate and subjected to a bi-axial stress in the film plane. Due to the substrate constraint, misfit dislocation are generated at the film/substrate interface. Let us assume dislocations are confined to move only through the film, such that dislocation penetration into the substrate, or the film surface (i.e. because of the presence of a passivated layer), it is not possible. Dislocation are then constrained to propagate through "channels" via single dislocation loops (see Figure 1.6 (a)). In analogy with equation 1.3 plastic deformation requires dislocation loops to fit between bounding interfaces, such that

$$d(\tau) = H' \tag{1.6}$$

where $d(\tau)$ is again the characteristic loop diameter (equation 1.2) and H'=$H/\sin\theta$ is the channel thickness (where θ is the angle between the slip plane and the film plane). We can solve now the stress required to move a dislocation through the channel as a function of the film thickness by combining equations 1.2 and 1.6

$$\tau = \frac{G_{eff}b}{H'} \tag{1.7}$$

where G_{eff} is an effective shear modulus accounting for the necessary energy balance between the line energy consecutive misfit dislocations generated and the energy of an elastically strained interface. For more details see Nix (1989). In case the film surface is free, i.e. unpassivated, it is sufficient to fit half a loop into the film $d(\tau)$=$2H'$. So the stress required to propagate a dislocation decreases by a factor of two (see Figure 1.6 (b)). As shown elsewhere (Keller

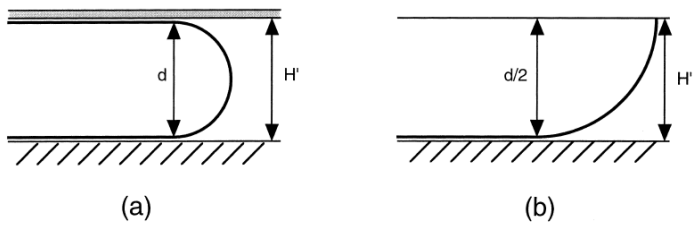

Figure 1.6: The dimensional constraint on plasticity in thin films: the yield stress can be estimated by requiring a dislocation loop to fit into the film ($d<H'$). H' depends on the film thickness H and the orientation of the slip plane. Case a: impenetrable film surface; case b: "free" film surface (Arzt, 1998).

et al., 1998), the model has shown to successfully account for strength differences on both passivated and unpassivated films.

Mechanical characterization of thin films by a variety of techniques have confirmed the yield strength dependency with thin film thickness proposed by Nix (1989). However, the model has been found to systematically underestimate the flow stress levels typically observed in the literature. Usually, thin films are expected to have polycrystalline microstructures with relatively fine grains with sizes comparable to the film thickness (Mullins, 1958). Though exceptions can be found when deposited epitaxially on single crystal substrates or heat treated in a way to encourage abnormal grain growth (Thompson, 1990). Thus, it is expected that microstructural size effects will also contribute to the overall strength, making computation of size effects in thin films more complex. Since its publication, much efforts have been put towards extending Nix's model to account for microstructural size effects associated to the grain size constrain. Thus, accounting not only for pure extrinsic size effects, but also for intrinsic ones. For more details see cited reviews (Arzt, 1998; Kraft et al., 2010) and references therein.

Uniform Deformation of Micro-size Samples: The Volume Effect

Uniform deformation of micro-size single-crystalline samples has attracted recently much interest. Unlike thin films, where the film is constrained by

a substrate, micro-size samples considered here are constrained-free volumes. Therefore, misfit dislocations mechanisms originated at the substrate/film interface no longer exits. Rather, plastic deformation is only constrained by the sample volume/geometry. Uniform deformation has been studied by both uniaxial micro-compression and micro-tensile tests. As will be reviewed in the next section, strain gradients are known to generate size effects. Thus, uniaxial tests are commonly used to achieve nearly uniform deformation states and isolate volume size effects from strain gradient plasticity effects. For a variety of crystalline materials, even in the absence of strong strain gradients, the yield strength has been repeatedly demonstrated to scale inversely with the sample size.

The study of unconstrained small scale specimens started with the pioneering work of Brenner (Brenner, 1956, 1957) on metallic whiskers. It was in the 1950's when Brenner impressively demonstrated that single-crystal filaments, few micrometers in diameter and presumably dislocation-free, can show very high strength (up to one third of the maximum theoretical strength). However, it has been in the last decade when mechanical characterization of small sample volumes has begun to increasingly attract scientific interest, in part thanks to the development of new technology-driven nanomechanical testing methodologies. In 2004 Uchic et al. (2004) presented a methodology for performing uniaxial compression tests on samples having micron-size dimensions. Sample fabrication was accomplished using Focused Ion Beam (FIB) milling to fabricate cylindrical specimens of uniform cross-section from bulk single crystals (see Figure 1.1 (b) an (c)). Uniaxial compression tests were carried out using a nanoindentation device outfitted with a flat punch tip. Few years later, in 2008 Kiener et al. (2008) extended the methodology to uniaxial tensile testing. Using FIB, samples were machined with a dovetail shape. The indenter was equipped with a counter-dovetail-shaped tip serving as sample gripper (see Figure 1.7). Both methodologies have been widely used to characterize the plastic response of samples at the micron scale, due to their readily interpretable tests, sample fabrication flexibility, and data collection precision.

Since the introduction of Uchic's work, tens of papers have been published on the uniaxial compression of micropillar samples (see reviews (Kraft et al., 2010; Uchic et al., 2009) and references therein). Micro-tensile tests are also increas-

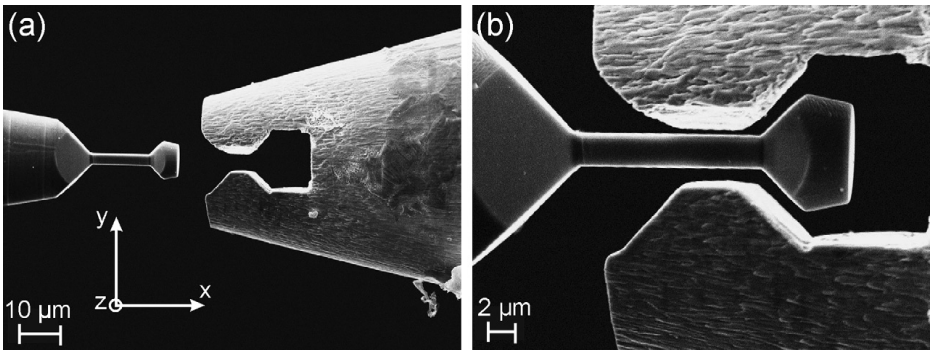

Figure 1.7: (a) SEM image showing a single-crystal copper tension sample and the corresponding tungsten sample gripper before the test at a low magnification. (b) Sample and gripper aligned prior to loading (Kiener et al., 2008).

ingly attracting attention, though sample fabrication is more costly, and consequently, the number of works published is still reduced. Nevertheless, Kiener et al. (2009) showed that material's strength does not change when switching between compression and tension within a single experiment. Collectively, both uniaxial tension and compression tests carried out in small single-crystalline samples have thoroughly demonstrate that crystalline materials are size-scale dependent and that occur in the absence of significant strain gradients. Usually, the effect of size is quantified in terms of a power law fit of the form

$$\tau = kd^{-n} \tag{1.8}$$

where τ is the flow stress, k is a constant, and d is the cross-section diameter. The power-law exponent n has been found to depend strongly on the system microstructure (i.e. dislocation density, Peierls barrier, etc.), with values ranging from 0.3 to 1.

Several attempts have been made to rationalize the dislocation based plastic mechanisms as a function of the sample volume, the three most commonly cited plastic mechanisms being:

Dislocation multiplication is a classical treatment of increase in yield stress caused by an increase of dislocation density, known as work hardening, or Taylor hardening (Taylor, 1934). Forest dislocations thread the slip plane acting as obstacles to the movement of mobile dislocations. With increasing dislocation density ρ, the average spacing between obstacles decreases in a power-law fashion $L{=}\rho^{-1/2}$. Requiring again that $L{=}d$ and substituting on equation 1.2, we obtain the classical Taylor equation for work hardening:

$$\tau = \alpha G b \sqrt{\rho} \tag{1.9}$$

where α (usually taken as 0.5) is a constant accounting for the fact that dislocations are not impenetrable obstacles. Thus, in large enough samples, where dislocations can interact and multiply before disappearing at the surface, the flow strength is not size dependent but rather dislocation multiplication-dependent with a bulk-like behavior.

Dislocation Source Truncation evaluates the effect of sample size on the source lengths, and on their operation strengths. Smaller sample volumes have statistically more double-ended sources upon operation interacting with the free surfaces and resulting in truncated single arm sources. Consequently, the mean source length necessarily has to decrease with sample size, as statistically demonstrated elsewhere (Parthasarathy et al., 2007). According to the line tension theory previously introduced, the shorter the dislocation length between pinned points the higher the shear stress required to operate the source. Thus, for small enough volumes, where truncated single arm sources begin to represent a significant fraction of the overall active dislocation sources, the flow strength becomes size dependent.

Dislocation starvation accounts for a change in the plastic deformation behavior with sample volume by examining the relative rates of dislocation multiplication and dislocation annihilation (Greer and Nix, 2006). The model postulates that for very small sample volumes dislocations have greater probabilities of annihilating at the free surface before interacting and multiplying with one another, which yields to a state of mobile-dislocation-density starvation. A sample with

eventually no mobile dislocations will accommodate plastic deformation by nucleation of new dislocations, and because dislocation nucleation requires a higher stress than dislocation glide, flow strength will rise with decreasing sample volume.

Although the three plastic mechanisms may co-exits and interact, each one of them is believed to dominate at a different length scale. For example, dislocation multiplication may dominate in large enough volumes, where dislocations have the chance to multiply and increase dislocation density, showing a bulk-like behaviour. Decreasing sample volume, source truncation with the free surfaces will become more likely, while dislocation multiplication phenomena gradually decrease, giving rise to a regime dominated by the sources' operation strength. Once a critical sample volume is reached, dislocation annihilation rate will exceed dislocation multiplication rate leading to a starved regime where dislocation nucleation-controlled regime may dominate.

So far, no scaling law with one universal power-law exponent has been found. Development of physically-based models is key to understand the complex interaction of these mechanisms and their underlying effects. However, besides sample volume, the behavior depends in a complex manner on other parameters, i.e. initial crystal orientation or surface state, which may not be captured in a simple power law.

Torsion and Bending of Micro-size Samples: The Strain Gradient Effect

Torsion and bending of micro-size samples are methods of inducing non-uniform deformation states by extrinsic (dimensional) constraints. When a sample is subjected to flexure (bending) or torsion it suffers from a deformation gradient necessary to accommodate differences in plastic strain between the neutral plane, where plastic strain is null by definition, and the surfaces, where it is $\gg 0$. When the sample volume is small the distances between the neutral plane and the surfaces decrease, increasing the strain gradient. Yield strength have been shown to scale with the strain gradient. Thus, it is the general dimensional length scale, i.e. the beam thickness in bending, or the wire diameter in twisting, the relevant

size parameter controlling size effects in strain gradient plasticity.

The study of strain gradient plasticity in micro-size samples began with the work of Fleck et al. (1994) on polycrystalline copper wires. Fleck carried out micro-torsion experiments on wires of 12-170 μm in diameter, observing a significant increase in yield strength with decreasing sample diameter. Similarly, Stölken and Evans (1998) observed a yield strength dependency with film thickness on bending experiments carried out on nickel foils 12.5-100 μm in thickness. These are the very first observations of size effects in which strain gradients were introduced by dimensional, or extrinsic, constraint.

The most commonly cited explanation of these size effects is the Strain Gradient Plasticity (SGP) theory. The fundamentals of SGP are based on Taylor's hardening model (Taylor, 1934). When a material is deformed, dislocations propagate, interact and multiply, building a network of trapping forest dislocations that increase the obstacles to further dislocation motion, resulting in hardening. A material that undergoes uniform strain will store randomly distributed dislocations, referred to as Statistically Stored Dislocations (SSDs) by Ashby (1970). On the other hand, a material that undergoes non-uniform strain will store, apart from the aforementioned SSDs, preferentially distributed dislocations, referred to as Geometrically Necessary Dislocation (GNDs), to accommodate the plastic strain gradient. As shown in Figure 1.8, the plastic strain ϵ_{pl} is zero along the axis of twist or at the neutral plane for both cylinder and beam deformation, respectively. However, $\epsilon_{pl} \gg 0$ at free surfaces. When the sample size is reduced, the plastic strain gradient increases, which causes a higher density of GNDs and hence enhance material strength.

The density of GNDs is directly related to the plastic strain gradient as (Fleck et al., 1994)

$$\rho_{gnd} = \eta_{pl}/b \tag{1.10}$$

where η_{pl} is the plastic strain gradient (which can be seen as the twist per unit length in torsion or the curvature of deformation in bending). Generally, in a strained body is defined as

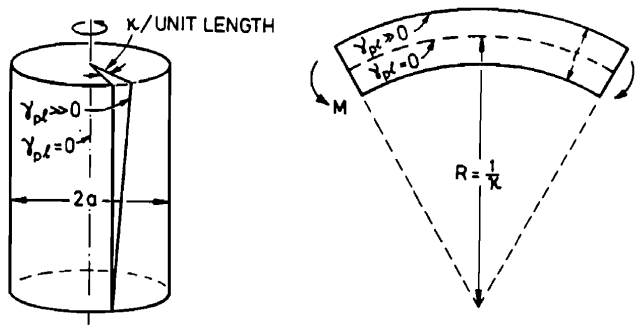

Figure 1.8: Plastic strain gradients caused by the geometry of deformation (Fleck et al., 1994).

$$\eta_{pl} = \epsilon_{pl}/l \tag{1.11}$$

Here, l denotes the general dimensional length scale, i.e. the wire diameter $2a$ in twisting and the beam thickness t in bending. Assuming total dislocation density ρ as the direct sum of SSDs and GNDs and substituting equations 1.10 and 1.11 into Taylor's hardening equation (1.9)

$$\sigma = \sigma_0 + A\alpha Gb\sqrt{\rho_s + \epsilon_{pl}/bl} \tag{1.12}$$

where A is a constant that relates shear stress and flow stress and ρ_s is the density of SSDs. Note SSDs is size-independent, but also contributes to the hardening evolution. Thus, according to SGP theory, the flow strength for a non-uniform deformation is proportional to a dimensional length scale: $\sigma \propto l^{-1/2}$.

SGP theory explains size effects by the increase of GNDs necessary to accommodate higher plastic strain gradients associated with smaller sample dimensions. However, it has been argued (Dunstan and Bushby, 2004) that SGP theory may not be representative of the plastic behaviour at the onset of plasticity, where plastic strain gradients, if any, are significantly small. Hence, GNDs

cannot be responsible for the observed size effects at the onset of plasticity.

The Geometric Critical Thickness Theory (GCTT) introduced by Dunstan and Bushby (2004) was developed to explain initial yield size effects. The model postulates that plasticity necessarily needs to take place in a finite volume rather than being continuous. Considering that the confined volume where dislocations interact decreases with sample volume, the stress required to produce yield necessarily has to rise at smaller samples. Because the model considers the finite volume length scale to be linearly related to the dimensional length scale l, at yield, $\sigma_y = E\epsilon_y \propto l^{-1}$. For more details on GCTT see Dunstan and Bushby (2004).

Nanoindentation of Bulk Samples: The Strain Gradient Effect Due to Small Strained Volume

Nanoindentation size effects arise not from small sample size but from limitation of the volume of material undergoing strain. When an indentation is performed a complex three-dimensional strain volume under the indenter, known as impression zone, undergoes plastic deformation. This plastic deformation changes dramatically from the contact point of the tip to the edge of the impression zone, generating a plastic strain gradient. When the indentation depth is small the impression zone decreases, increasing the strain gradient. As shown above, yield strength scales with the strain gradient. Thus, it is the impression zone the relevant size parameter controlling size effects in nanoindentation.

A full understanding of nanoindentation size effects depends on the characterization of the complex strain volume under the indenter. The impression volume is strongly dependent on the indenter tip geometry, reason why, a number of nanoindentation studies has been carried out under different tip geometries. First indentation size effects were reported in 1995 by Ma and Clarke (1995). Since then, studies on asymmetric (knife edge) indenters have been limited and incompletely characterized, particularly as concerns the constraint dimension (length or width). On the other hand, studies on symmetrical indenters, particularly spherical indenters, are better understood. Spherical indentation has the advantage that it induces a larger area of contact at small depth, which enables

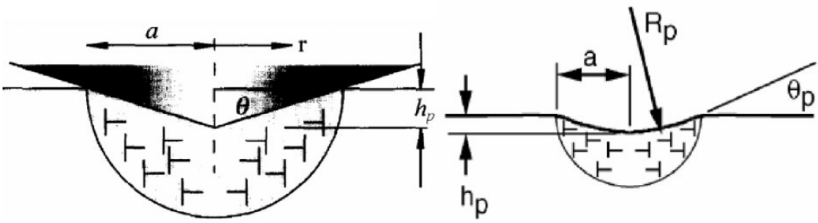

Figure 1.9: Schematic depiction of GNDs created by pointed and spherical indentation in strain volume under indenter (Johnson, 1985).

the entire stress-strain curve to be measured. They began with the work of Lim and Chaudhri (1999) on annealed copper, and nowadays nanoindentation size effects on spherical indenters is a well accepted phenomenon.

The original and most common cited explanation to rationalize indentation size effects is the SGP theory. Nix and Gao (1998) first calculated the density of GNDs under a symmetrical indenter as

$$\rho_{gnd} = \psi / V \tag{1.13}$$

where V is the impression zone volume and ψ the total length of GNDs. Under a symmetric indenter, the impression zone can be considered as a half-sphere of radius equal to the contact radius a, as shown in Figure 1.9. According to Nix and Gao (1998), ψ is defined as

$$\psi = \pi h_p a / b \tag{1.14}$$

where h_p account for the indentation depth and b for the Burgers' vector. Substituting equation 1.14 into 1.13

$$\rho_{gnd} = 3h_p / 2ba^2 \tag{1.15}$$

Following indentation strain definition given by Nix and Gao (1998)

$$\epsilon_{ind} = h_p/a \tag{1.16}$$

and assuming plastic strain as $\epsilon_{pl} = 0.2\ \epsilon_{ind}$ (Yang et al., 2006). The flow stress dependency on GND density given in equation 1.12 can be rewritten as

$$\sigma = \sigma_0 + A\alpha Gb\sqrt{\rho_s + 15\epsilon_{pl}/2ba} \tag{1.17}$$

where again the flow strength for a non-uniform deformation is proportional to a dimensional length scale. As for sharp indenters, a is proportional to h_p, i.e. in Berkovich indenter $a \approx 16h_p$. It can be concluded a is the relevant size parameter controlling size effects rather than h_p or R, such that: $\sigma \propto a^{-1/2}$.

Several model modifications (Backes et al., 2006; Gao et al., 1999) have been proposed that seem to improve model agreement with experimental data (Yang et al., 2006; Zong and Soboyejo, 2005). However, SGP predictions fail at very small penetration depths. Similarly to micro-bending and micro-torsion model, SGP theory is not able to capture the initial yield strength enhancement observed experimentally due to the absence of plastic strain gradients at the onset of plasticity. Attempts have been made to approach the computation of the initial yield size effect in spherical indentation by a GCTT model, as shown elsewhere (Spary et al., 2006). However, this theory is still under development.

Recently, Nix et al. (2007) also proposed a different type of indentation size effect for shallow indents. The model predicts that at lower loads the probability of finding a suitable dislocation source in the loaded volume is reduced, so the volume probed becomes eventually dislocation free. Hence, plastic deformation requires the nucleation of a dislocation source, with its corresponding increase in yield strength. Other groups (Gerberich et al., 2003, 2005; Zhang and Xu, 2002) have also explore nanoindentation size effects via an energy balance argument.

As for micro-bending and micro-torsion size effect models, each model proposed here may be valid under different circumstances. They may possibly co-

exits and interact at different scale regimes. Further investigations are required to fully understand their implications.

1.3 Size Effects in Micro-size Single-crystals Deformed in Compression

1.3.1 Micro-compression Methodology and Associated Concerns

Micro-compression testing methodology was briefly introduced in the previous section. Here we review in more detail the methodology, first proposed by Uchic et al. (2004), for the mechanical characterization of micro-size specimens in compression. The testing methodology is designed to mimic the experimental approach usually employed in macroscopic compression tests. Logically, sample fabrication and mechanical testing methods employed at the micro-scale imply some design reconsiderations motivated by the scale of the sample. The most significant difference is the fact that samples are not free standing specimens. In order to easily handle and manipulate such a small volumes, the sample is fabricated leaving attached one of its ends to the macroscopic (bulk) substrate. As a result, the substrate acts as a lower compression platen during the test, which among other concerns, adds an extra compliance to the system. Compression test are performed with standard instrumented nanoindentation systems adequately fitted with a flat punch tip. The performance of current commercial nanoindentation equipments allows load and displacement measurements with resolutions of nN and nm, respectively. In principle, systems with this specifications are well suited to measure samples at the micro- and sub-micro-meter regime, though this may depend on the strength of the material system tested.

Sample Fabrication Concerns

Since the introduction of the micro-compression test, several methods have been proposed for the fabrication of micro-compression samples. The most popular method is with no doubts focused ion beam (FIB) milling. The technique

combines both precision and flexibility, which allows sample fabrication into the surface of a bulk crystal with extreme control over the geometry and size of the sample. However, the technique also has some associated concerns. Other sample fabrication techniques proposed are lithography-governed processes (Greer and Nix, 2006; Moser et al., 2007) or selective etching of directionally solidified alloys (Bei et al., 2007).

Two types of sample geometries are generally produce by FIB milling depending to the sample fabrication method employed, namely annular and lathe milling (see Figure 1.10 (a) and (b), respectively). The former consist of milling consecutive concentric ring-shaped patterns of decreasing size (Greer and Nix, 2005; Greer et al., 2005; Ng and Ngan, 2008c; Shan et al., 2007; Volkert and Lilleodden, 2006). This method is commonly used owing to its easy to used procedure. By simply placing the desired bulk sample surface oriented perpendicularly to the incident ion beam, a serial of concentric annular patterns are milled. The method is easy, relatively fast, and straightforward. However, sample geometry obtained with this method lacks of a constant cross-sectional area. When milling, the beam tends to deflect, causing pillar diameter to increase with milling depth. As a consequence, micropillar samples always present some degree of taper. Depending on milling conditions, the taper angle usually varies between 2°-5° (Korte and Clegg, 2011; Shim et al., 2009; Zhang et al., 2006). The biggest concern with tapered pillars is the fact that this geometry leads to a non-uniform stress field within the sample, as shown elsewhere analytically (Shan et al., 2007) and numerically (Zhang et al., 2006). These studies showed that taper of the pillar results in artificial strain hardening, inaccuracies in determining the elastic modulus, and increase in the apparent yield point. The other mayor concern is the gauge length, which normally is not uniform and introduces inaccuracies in the determination of the aspect ratio (length-to-diameter ratio). Hence, quantitative data obtained from samples with this geometry should be assessed critically with respect to these sources of error.

The second type of sample fabrication method, known as lathe milling, is a more elaborated method developed to obtain taper-free pillars (Uchic and Dimiduk, 2005; Uchic et al., 2003, 2004). It consists of two steps. First a coarse annular milling is employed to obtain a gross tapered pillar. The second step

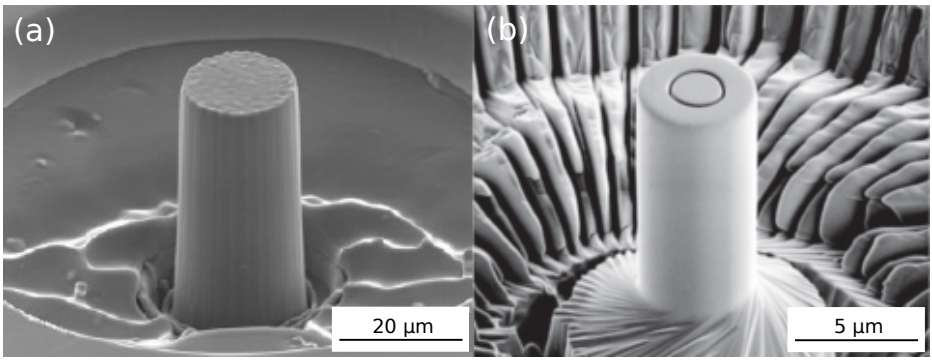

Figure 1.10: Scanning electron microscope (SEM) images of micro-compression samples fabricated by Focused Ion Beam (FIB). (a) Sample fabricated by annular milling technique. One can clearly observe a small degree of taper (from Lee et al. (2007)). (b) Sample fabricated by lathe milling technique. The circular pattern on the top surface of the sample is a fiducial mark used as part of the automated machining program for the FIB (from Dimiduk et al. (2005)).

involves tilting the sample so that the beam is at an oblique angle to the bulk sample surface. Once tilted, the ion beam can be used to mill away the visible taper of the sidewall along one side of the sample. The process must be repeated after rotating the sample in small angular increments (typically 5°-10°) until a loop is completed, in a manner similar to a lathe. This method allows accurate control of both gauge length and cross-section diameter, leading to a much better defined geometry. In addition, this approach is suitable for fabrication of polycrystalline samples, whereas annular milling may find problems with differential ion sputtering rates (Volkert and Minor, 2007), function of the chemistry, orientation, and local surface topology. The main drawback of this approach is the ion beam time-exposure, that besides making sample preparation significantly more costly, sensitively increases Ga ion implantation-damage.

Ga ion irradiation-damage may probably be the biggest concern associated with any sample fabricated by FIB, no matter the milling approach followed. FIB milling is known to generate an irradiation-damage layer caused by the highly accelerated incident ions. The extent of this damage layer depends on a number of factors, including the ion voltage, the dose, the angle of the incident beam, or

the target material, to name a few (Kiener et al., 2007; Williams et al., 2010). In some specific materials precipitation of Ga-containing phases may also be an issue (Yu et al., 2006).

Several attempts have been made to assess the effect of FIB-irradiation damage, using nanoindentation hardness measurements (Bei et al., 2007; Motz et al., 2005), micropillar compression tests (Greer and Nix, 2006; Greer et al., 2005), or in-situ TEM compression tests (Shan et al., 2007). Each approach has positively contributed to expand the still scarce knowledge on this topic. For example, nanoindentation hardness measurements on irradiated surfaces showed a strengthening effect due to ion implantation damage, while micropillar compression test on Au crystals prepared with four degrees of implantation damage (Greer and Nix, 2006; Greer et al., 2005) did not show any significant evidence of strengthening effect due to FIB-irradiation damage. On the other hand, TEM tests on Ni micropillars showed how irradiation defects even disappeared from sub-micrometer crystals upon loading. However, the number and variety of studies in this area is still insufficient and more definitive studies are needed to better understand the extend at which FIB-irradiation damage affects the strengthening of micro-compression test specimens.

Compression Testing Concerns

When performing compression tests on micro-size specimens few additional considerations have to be taken into account in order to carry out accurate experiments. Commercial nanoindentation systems are commonly classified into two classes, inherently displacement- or load-controlled systems. The choice of testing mode may significantly influence the stress-strain response of the sample. Unlike bulk-crystal, micro-size crystals are prone to show strain instabilities, i.e. strain bursts. A displacement-controlled system, where a constant displacement rate is imposed, will damp out strain bursts generating a serrated stress-strain response. Conversely, applying a constant load rate with a load-controlled system will enlarge strain bursts. Hence, a material showing frequent strain burst events may draw a completely different strain-hardening behaviour depending on the testing mode chosen, as exemplified in Figure 1.11). Nowadays, commer-

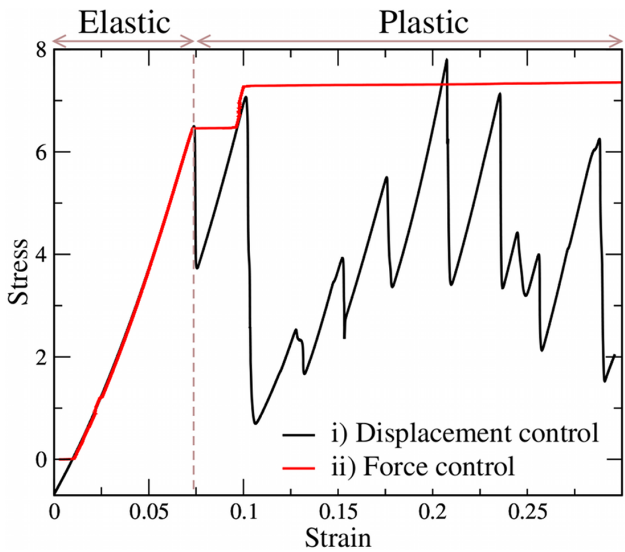

Figure 1.11: Strain-hardening response as a function of testing mode: i) a serrated flow stress response under displacement-control conditions, or ii) a staircase shaped behaviour under load-control conditions. The dashed line signals the location of the yield point (from Moretti et al. (2011)).

cial nanoindenters are predominantly load-controlled systems, although most of them incorporate proportional-integral-derivative (PID) controllers, to run experiments in displacement-controlled mode. In fact, most micro-compression experiments published to date were carried out at a constant strain rate. Thus, stress-strain response should be always assessed critically with regard to both, the testing mode employed, and the inherent testing mode of the system.

Other testing concerns are associated with the micropillar-substrate interaction. As mention above, micropillars are fabricated partially attached to the bulk substrate to facilitate their manipulation. As a consequence, the substrate acts as a lower compression platen, adding an extra compliance to the system. To correctly compute the stress-strain response of the pillar, this extra compliance needs to be subtracted. Several methods have been proposed to calculate the substrate deflection and correct the system compliance (Choi et al., 2007; Greer

et al., 2005; Zhang et al., 2006). Another influence of the substrate is its integral connection with the micropillar. In macroscopic compression tests, ensuring an adequate lubrication between both platens and the sample is a good experimental practice to minimize possible contact constraints and assure an uniform internal stress field. However, in micro-compression experiments boundary conditions necessarily differ. The micropillar is rigidly constrained at the base, which generates a triaxial stress state at the bottom. At the top of the pillar, boundary conditions become more complex, and are determined by both the lateral stiffness of the flat punch and the contact friction between pillar and punch. Recently, Shade et al. (2009) suggested after in situ observation that specimens do not slip against the flat punch, rather punch and specimen move jointly during deformation. Thus, triaxial stress states should be expected at both the contact and base of the pillar, affecting the uniformity of the stress field along the pillar.

Shade et al. (2009) assessed the extend at which lateral stiffness of the system influenced the mechanical response of the pillar, concluding that this constraint, besides affecting the uniformity of the stress field, affects the following phenomena: the measured flow stress, the observation of large strain bursts, and the strain-hardening behaviour. Hence, determination of the lateral stiffness of the testing system is another important factor to understand the observation or absence of a particular plastic phenomenon.

Another concern related to the lateral movement of the top of the pillar is plastic instability or buckling. Several works have shown that buckling can be prevented decreasing the micropillar's aspect ratio or constraining the specimen's lateral movement (Raabe et al., 2007; Zhang et al., 2006). Considering that changing the lateral stiffness of the system may not be an easy task, most scientists prevent from buckling by fabricating samples with small enough aspect ratios (ranging from 2:1 to 3:1). Smaller ratios should be avoided in order to minimize stress contributions originated at the bottom and top of the pillar due to boundary constraints.

An additional source of plastic instability is the presence of a contact misalignment between the flat punch and the head of the pillar. The misalignment effect has been studied using continuum (Zhang et al., 2006) and crystal-plasticity (Choi et al., 2007) finite element models (FEM). Both studies suggest that se-

tups with system misalignments greater than 1° are prone to shown test artifacts. Some attempts have been made to improve setup alignment (Uchic and Dimiduk, 2005), though further developments in this area are needed.

In summary, performing micro-compression experiments involve a number of testing challenges which influence the overall mechanical response of the sample. Much efforts have been directed towards identifying these challenges and understanding the kind of test artifacts they may introduce. Some of them are well-documented and nowadays are relatively easy to prevent, whereas others are still subject of controversy. In conclusion, experiments that do not attempt to account for these kind of experimental uncertainties are likely to have artifacts present in the data.

1.3.2 Size Effects in Different Material Systems

Face-centered Cubic Metals

Uniaxial compression of micrometer-scale single-crystals started with the pioneering work of Uchic et al. (2004) on Ni micropillars. Since then, a large number of studies have been published in a variety of materials, the vast majority focusing on face-centered cubic (FCC) metals. These simple metals, largely studied during decades, are the best understood in terms of dislocation processes and structures that result from plastic deformation. Moreover, there is extensive data available on the mechanical behaviour of both bulk samples and whiskers. Among the most widely studied FCC metals at the micro- and sub-micron scales are: Ni (Dimiduk et al., 2005; Frick et al., 2008a; Shan et al., 2007; Uchic et al., 2004), Au (Greer and Nix, 2005, 2006; Greer et al., 2005; Volkert and Lilleodden, 2006), Cu (Kiener, 2007; Kiener et al., 2006; Kraft and Volkert, 2006), and Al (Kraft and Volkert, 2006; Ng and Ngan, 2008c).

This studies have repeatedly demonstrated that at the micron- and sub-micron scales sample size dramatically influences material strength. All FCC metals tested in these scale regimes display several similarities in the stress-strain response. For large enough samples, bulk-like behaviour is observed with a relatively smooth stress-strain response, whereas for pillars approaching the micron scale strain bursts become increasingly distinctive causing a serrated-like

stress-strain curve. Moreover, on top of that the flow stress increases significantly with smaller specimens, with the smallest pillars of few hundred nanometers in diameter sometimes attaining a flow stress an order of magnitude higher than the bulk (see Greer and De Hosson (2011) and reference therein).

As introduced earlier, the flow strength dependency with sample size can be empirically described by a power law (equation 1.8). Generally, this relationship holds for samples that range from a couple hundred nanometers to tens of micrometers (Uchic et al., 2009). Using the pillar diameter d as characteristic length scale, the power-law exponent n for FCC metals has been found to vary between 0.6-1, depending on the study. Dou and Derby (2009) summarized the compressive strength data for FCC metals and proposed the existence of a universal law of the form

$$\frac{\tau_{CRSS}}{K_s} = A\left(\frac{d}{b}\right)^{-n} \tag{1.18}$$

where τ_{CRSS} is the critical resolved shear stress, K_s is the anisotropic shear modulus, d is the pillar diameter, and b is the magnitude of the Burgers' vector. A is a constant and n is the power-law exponent. Based on the existing data they found n to be 0.66. Concurrently, Uchic et al. (2009) proposed a different formulation for collapsing into a single band the FCC size-dependent data:

$$\frac{(\tau_{CRSS} - \tau_0)}{K_s}\frac{b_{Ni}}{b} = Ad^{-n} \tag{1.19}$$

which relates a normalized effective resolved shear stress (left-hand side of equation) as a function of the sample diameter d. The effective shear stress is normalized by the shear modulus on appropriate slip system K_s, and the relative ratio of the Burgers' vector of each metal to a reference (Ni in this case), b_{Ni}/b. As shown in Figure 1.12, the exponent n that best fits the data is $\sim$0.6. This exponent is very close to that reported by Dou and Derby (2009) and to all other FCC micro-compression studies, where the samples contain initial dislocations (i.e. not whiskers). The results of all of these reports show a very similar

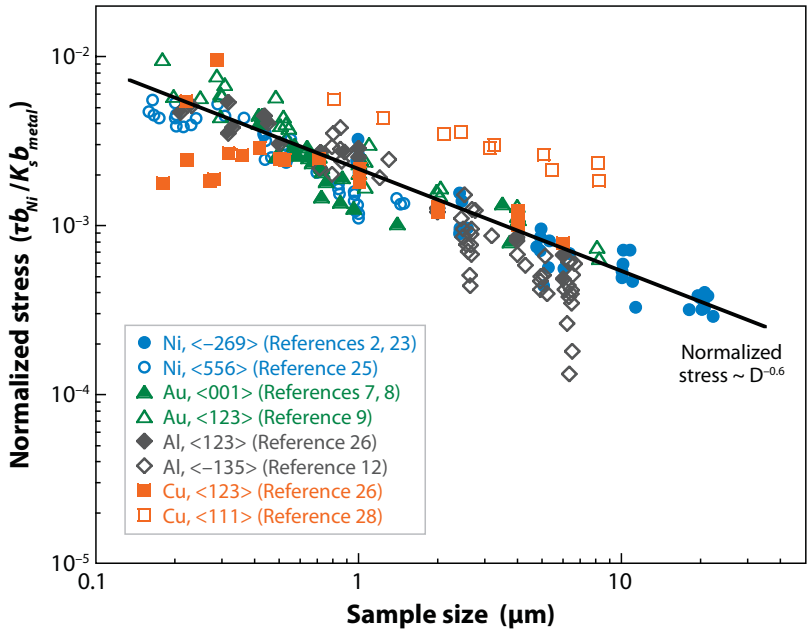

Figure 1.12: Composite plot of published microcrystal flow stress data as a function of sample diameter for FCC metals. Data in the plot have been normalized by the anisotropic shear modulus and Burgers' vector for each material, and the reference flow stress, τ_0, was considered negligible (Uchic et al., 2009).

power-law dependence between the flow stress and sample size, regardless of the scaling law formulation, implying that this relationship might be universal for FCC metals.

Body-centered Cubic Metals

To date the study of plasticity in small-scale volumes has been mainly focused on investigating face-centered cubic (FCC) metals, though the scientific community's interest is naturally swifting towards investigating different material systems, as demonstrated by the increasing number of works published on body-centered cubic (BCC) metals and other non-FCC metals. These works have shown that the size dependence of the yield stress differs fundamentally between

FCC and BCC metals. In both families of materials the yield strength σ_y scales inversely with some power of the pillar diameter d. In FCC metals we have shown how $\sigma_y \propto d^{-n}$, with n varying between 0.6-1, whereas BCC metals exhibit a less pronounced size effect, with n ranging between 0.21-0.48. Plasticity in BCC metals is much more intricate than that in FCC metals. The mechanical response generally have a strong thermal dependence, which has been argued (Schneider et al., 2009b) to be due to the temperature-dependent mobility of screw dislocations, known to govern the plastic deformation process. Besides, owing to the three-fold symmetry of the screw dislocations in BCC metals slip occurs simultaneously at various slip systems, causing non-planar screw dislocation cores, which results in a lower screw dislocation mobility (Argon, 2008).

The study of small-scale plasticity on BCC metals started with the work of Bei et al. (2007) on directionally solidified Mo-alloys. They introduced a new technique to produce defect-free single crystalline Mo solid-solution micropillars by selective etching of a two-phase euctectic, where the single crystalline Mo phase solidifies as aligned rods within the matrix phase. In a posterior study the bulk Mo-alloy were pre-strained prior to etching to introduce dislocations into the initial microstructure (Bei et al., 2008). By this method, specimens with three degrees of initial structural defects, 0%, 4%, and 11% pre-strain, were obtained and subsequently tested, providing significant insights into the size-effect dependency on the initial dislocation density. Intriguingly, either under dislocation-free conditions (0% pre-strain samples) or high enough initial dislocation density (11% pre-strain samples), the deformation behaviour was independent of the sample size. Only at the intermediate dislocation density (4% pre-strain samples) a size-dependent strengthening was observed. Moreover, contrary to the bulk-like behavior, the increase in dislocation density weaken the material. Defect-free pillars showed a extremely high yield stress, close to the theoretical value, whereas pillars with the highest starting dislocation density presented in average the softest response.

Few other BCC systems have been studied to add insight into the size-dependent plastic behaviour of BCC metals. Schneider et al. (2009b) studied the mechanical behavior of four different single-crystalline $\langle 001 \rangle$-oriented BCC metals (Mo, Nb, Ta, and W) at room temperature and found systematically a

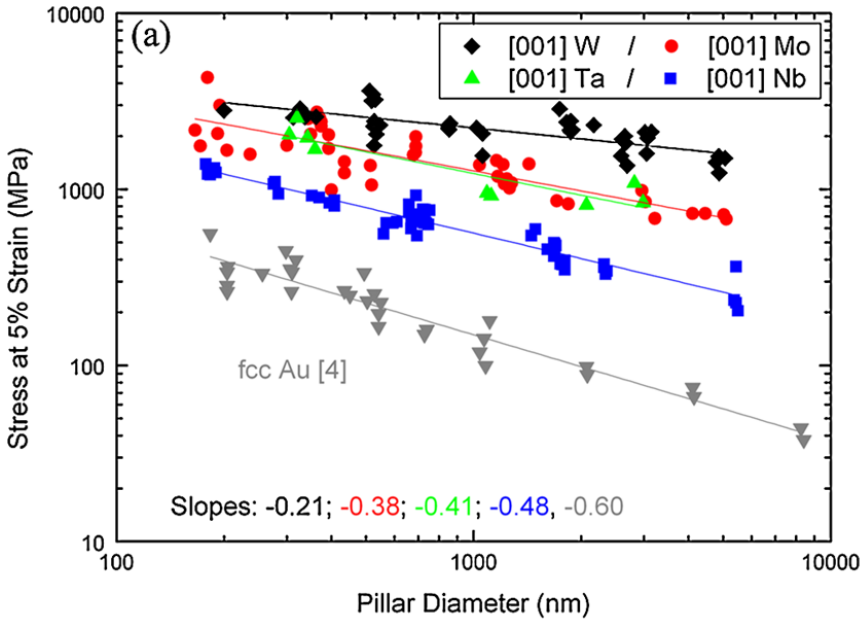

Figure 1.13: Comparison plot of stress measured at 5% strain versus pillar top diameter for [001] BCC pillars (W, Mo, Ta, and Nb). [001] Au pillar data is include from comparison (from Volkert and Lilleodden (2006)) (Schneider et al., 2009b).

lower size-effect strengthening than on FCC metals. By using a power law fit, slopes of -0.21, -0.38, -0.41, and -0.48 were obtained for W, Mo, Ta, and Nb pillars, respectively (Figure 1.13). This values contrast with the typical FCC behaviour, where values between -0.6- -1 have been reported. In addition, they also observed a power-law exponent dependency on the inverse of the critical temperature T_c for each material, suggesting that screw dislocation mobility (lower than edge dislocation mobility below T_c) may play a dominant role on the size-effect strengthening. Kim et al. (2010), who also studied the same four materials in uniaxial compression and tension, reported qualitatively the same results, with pillars tested in compression presenting power-law slopes $\sim$-0.44 (except for Nb, with -0.93). In tension, slope values diverge more, as suggested by the authors, due to the tension-compression asymmetry, which it is self size

dependent (Kim et al., 2010).

Other Materials

Beyond single-crystalline FCC and BCC metals, a variety of material systems are being explored in the context of small-scale plasticity. Some of them are: non-cubic single crystals (hexagonal close-packed (HCP) metals (Byer et al., 2010; Lilleodden, 2010; Sun et al., 2011; Ye et al., 2011; Yu et al., 2010), tetragonal metals (Lee et al., 2010, 2011), shape memory alloys (Frick et al., 2007, 2008b; Norfleet, 2007)), nanocrystalline metals (Jang and Greer, 2011; Jang et al., 2011; Rinaldi et al., 2008), nanolaminates composites (Mara et al., 2008a,b), ionic alkali halides (Nadgorny et al., 2008), or metallic glasses (Lai et al., 2008; Schuster et al., 2008; Volkert et al., 2008), to name a few. Some of these studies address the combined effect of intrinsic, i.e. microstructural, and extrinsic, i.e. sample dimensions, characteristic length scales. The interaction of dislocations (principal plasticity carriers) with other microstructural features, i.e. grain boundaries, at small-scale volumes is certainly a field that requires further research and will surely grow in the next years. Interesting developments have been also recently published in small-scale plasticity of metallic glasses, where plasticity is not controlled by dislocations but for extremely thin sheet-like shear bands within the amorphous microstructure (Zhang and Greer, 2006). However, the aim of this review is to gather together state of the art size-effect studies on single-crystalline materials deforming via crystallographic slip, where a priori, only sample dimension effects constrain plastic deformation.

Good examples of investigations in non-cubic metals are the few works carried out on single-crystalline HCP metals. For example, Byer et al. (2010) and Lilleodden (2010) concurrently published similar compression experiment on Mg $\langle 0001 \rangle$-oriented micropillars, though the two groups report diametrically opposite size-dependent strengths. Both studies concluded that deformation occurred via multiple slip on pyramidal planes. Unfortunately, neither works provide information of the starting dislocation densities, which may be the main reason for the differences in the size-effect strengthening. Most recently, Ye et al. (2011) reported the presence of strong size effects associated with two distinct plastic

mechanisms: basal plane sliding and extension twinning. Additionally, Yu et al. (2010) carried out micropillar compression of Ti alloy. These authors observed two size-dependent strength regimes: one dominating at the micro-scale (pillar diameters in the range 1 to 10 μm) and strongly dependent on the sample size, where deformation is accommodated by twinning; the other size-independent and controlled by crystallographic slip, for pillar diameters <1 μm. Contrary, Sun et al. (2011) did observed that single-crystalline Ti micropillars oriented for prismatic slip are prone to show size effects. Undoubtedly, more definitive studies are required to understand competing deformation processes on HCP metals and their interactions in confined dimensions.

Other interesting non-cubic metals that have been found to show other deformation mechanisms than traditional crystallographic slip are tetragonal metals. Lee et al. (2010, 2011) investigated the mechanical properties of In by micro-compression experiments and found that pillars felt into two categories: those with low flow stresses near that of bulk indium regardless of pillar diameter and deforming via extrusion; and those attaining very high strengths and deforming via crystallographic slip, showing a strong strengthening when decreasing sample size.

Interesting is the study of alkali halide LiF crystals carried out by Nadgorny et al. (2008). For the first time, they demonstrated that size effects are not confined to metals and alloys but are also typical for other type of solids, like LiF. They examined the compressive response of micro-size $\langle 100 \rangle$-oriented single-crystal pillars and found a strain-hardening behaviour that resembles that of the FCC metals, regardless of a low starting dislocation density (less than 10^9 m^{-2}). The power-law scaling exponent was found to be $\approx$0.8, slightly higher than most FCC, probably due to the low initial dislocation density. Alkali halides greatly differ from cubic metals in terms of internal structure, i.e. structure of dislocations, and somewhat surprising is the fact that plastic response overwhelms any of these differences. These findings opened up new areas for detailed investigation of non-metallic systems. However, more research is needed to conclusively determine whether this scaling behavior trend is real.

Concluding Remarks

Microcompression experiments have demonstrated to be a valuable method to the study of dislocation-based deformation processes. There is now clear evidence that size-scale effects exist independently of other known size-dependent strengthening effects such as the grain size effect or the presence of imposed strain gradients. The microcompression experiments discussed herein were largely performed on constrained-free single-crystal samples, thus removing complications associated with strengthening due to either grain boundaries or an underlying substrate —like in the case of thin films. However, there are still many open questions regarding these size-dependent strengthening phenomenon, such as the following:

- What intrinsic properties lead to the observed size effect dependency with material system?
- How do sample fabrication and testing methods influence the measurements?
- How do mechanisms such as thermal activation affect the size-dependent response?

1.4 Aim of the Study and Summary of the Work

This investigation was aimed at ascertaining the role of the intrinsic lattice resistance of the material on the size-dependent strengthening effect, in order to extend current knowledge on the observed size effect dependency with material system. In particular, the objective of this study was to see whether different slip systems can be characterized individually using micro-compression and to analyze how size effects differed as a function of the bulk critical resolved shear stress of the operative slip system. For this, materials with a marked plastic anisotropy are preferred due to their large difference in bulk critical resolved shear stress between slip systems. However, little was known on the kind of test artifacts single-crystal micropillars with a marked plastic anisotropy might present during micro-compression testing. Thus, the second objective of this work was to

expand the still scarce knowledge on this area by developing numerical tools based on crystal plasticity finite element simulations. Besides, there were other concerns associated with micro-compression tests. For example, several attempts were made to assess the focused ion beam (FIB) machining influence on the sample response. However, the number and variety of studies in this area was still insufficient. Thus, the third objective of this investigation was to contribute in this topic by studying micro-compression test specimens fabricated with and without the need of FIB milling. And finally, we also aimed to report for the first time on the role of temperature on the size effects, further discussing on the role of the lattice resistance and its reduction with temperature due to thermal activation.

In this work, we have contributed to solving these open issues by studying the size effect in flow stress of LiF single-crystal micropillars oriented in the [111]-direction. LiF was chosen as the model material as its lattice resistance depends strongly on the operative slip systems, and therefore on the crystallographic loading axis. We fabricated our LiF samples by chemically etching away the matrix of directionally solidified NaCl-LiF and/or KCl-LiF eutectics, obtaining micropillar with diameters in the range 1-5 μm and fabricated without the need of FIB milling. Plasticity in LiF was evaluated in terms of crystal orientation and slip systems activation by means of crystal plasticity finite element simulations, focusing on the response of two micropillar crystallographic orientations with very distinctive bulk critical resolved shear stress, the soft [100]- and the hard [111]-orientation, and the influence of three possible experimental uncertainties associated with the alignment of the micropillars: geometrical tilts, lattice rotations, and misalignments between the surfaces of the flat punch and the head of the pillar. Initial micro-compression test were carried out ex situ at room temperature, and size effects as a function of the lattice resistance were discussed to the light of previous results in the [100]-orientation (Nadgorny et al., 2008). To evaluate the effect of the ion-irradiation induced damage, selected [111]-oriented pillars were further exposed to the ion beam inside a FIB workstation and yield strength and maximum compressive strength were compared with previous obtained irradiation-free micro-compression data. Finally, micro-compression tests at elevated temperatures were carried out, and the observed size effect depen-

dency with temperature was quantitatively compared with the reduction of the lattice resistance due to thermal activation.

1.5 Outline of this Dissertation

In Chapter 2, the basis of the main experimental techniques and materials used in this work are reviewed. Specifically, we introduce a novel approach to fabricate micro-size single-crystalline LiF pillars and briefly review the nanoindentation instruments and the Dual-beam Focused Ion Beam (FIB)-Scanning electron microscope (SEM) (FIB-SEM) equipment used. In Chapter 3, a crystal plasticity finite element (CPFE) analysis of the challenges of compressing single-crystal micropillars with a marked plastic anisotropy is presented. The study covers the analysis of three experimental uncertainties which are representative of real micropillar compression testing challenges. Chapter 4 analyzes the flow stress dependency with the sample size as a function of the intrinsic lattice resistance of the material. The effect of FIB-machining on the compressive response is also discussed. To the light of previous results at room temperature, the role of temperature on the size effects is discussed in Chapter 5. Finally, the conclusions extracted from this investigation and some suggestions for future work are presented in Chapter 6.

2

Materials and Methods

2.1 Introduction

This chapter details the basis of the main experimental techniques and materials used in this work. A novel approach to fabricate micro-size single-crystalline pillars for micro-compression testing is introduced. Up to date, most micro-compression experiments have been performed on micropillars fabricated from the bulk by means of Focused Ion Beam (FIB) milling. The fabrication approach presented here shows how to obtain micro-size single-crystalline pillars from directionally solidified eutectics (DSE). Specifically, we show how to fabricate LiF micropillars from directionally solidified LiF-NaCl and LiF-KCl eutectics. The crystallography of the resulting LiF single-crystals is also analyzed. LiF is an ionic compound with a rock-salt (NaCl) structure. The plastic behaviour in this type of structures, and more specifically in LiF, is evaluated in terms of crys-

tal orientation and slip systems activation. Finally, the fundamental equipments used in this investigation are briefly introduced. The nanoindentation instrument is presented, and ex- and in-situ platforms used in this investigation are shown in more detail. The Dual-beam Focused Ion Beam (FIB)-Scanning electron microscope (SEM) (FIB-SEM) system employed for micro-sample fabrication and microscopy applications is also presented.

2.2 Plasticity in Rock-Salt Ionic Compounds: Lithium Fluoride

LiF is an ionic compound with a rock-salt (NaCl) structure. Examples of compounds with this structure include NaCl itself, along with almost all other alkali halides, and many divalent metal oxides, sulfides, selenides, and tellurides (Seitz, 1940). Rock-salt type materials are ionic compounds with a 1:1 stoichiometry ratio. Each ion is octahedrally coordinated by six counter-ions, and so this structure has a so-called (6,6)-coordination, where the first number refers to the coordination of the cation and the second to the anion. The structure is formed based on a FCC array of anions, coordinate positions (000, $\frac{1}{2}\frac{1}{2}0$, $\frac{1}{2}0\frac{1}{2}$, $0\frac{1}{2}\frac{1}{2}$), with the cations occupying all the octrahedral holes in the FCC lattice, coordinate position ($\frac{1}{2}\frac{1}{2}\frac{1}{2}$, $\frac{1}{2}00$, $0\frac{1}{2}0$, $00\frac{1}{2}$). However, it could also be seen as an FCC array of cations, with the anions in all the octahedral holes.

Plastic slip in these rock-salt type structures differ form that in the FCC metals. Slip in FCC metals occurs along the close packed planes. Specifically, the slip planes are of type $\{111\}$, and the directions are of type $\langle 110\rangle$. Given all combinations of slip planes and slip directions, FCC metals have 12 slip systems. However, for rock-salt type structures like LiF, slip on the $\{111\}$ close packed planes is not longer favored —$\{111\}$ planes are composed of either anions or cations, with each plane being adjacent to two other $\{111\}$ planes of opposite charge, which generates a strong preferential bonding force between the planes, and therefore prevents any plastic slip along them—. Instead, rock-salt compounds have two other sets of slip systems, the $\{110\}\langle 110\rangle$ and the $\{100\}\langle 110\rangle$. Given the permutations of the slip plane types and direction types, each set

of slip systems have 6 slip systems. Johnston and Gilman (Gilman, 1959a,b; Johnston and Gilman, 1959), who extensively studied the plastic deformation of LiF single crystals, see Figure 2.1, reported a critical resolved shear stress on the $\{110\}\langle 110\rangle$ slip systems at 10^{-3} s^{-1} strain rate and room temperature of the order of 8-15 MPa, depending on initial dislocation density. In the case of plasticity in the $\{100\}\langle 110\rangle$ slip systems, there are no data at room temperature for bulk crystals because of their brittle behavior. Extrapolation of high temperature results to room temperature points to ratios of the critical resolved shear stresses between the two sets of slip systems, $\tau_{\{100\}\langle 110\rangle}/\tau_{\{110\}\langle 110\rangle}$, of the order of 10-20 (Gilman, 1959b), which denotes the highly plastic anisotropy of LiF.

With such a large difference in critical resolved shear stress between the two sets of slip systems, it is straightforward to elucidate that as long as the softest slip systems are activated, most, if not all the plastic activity, will be accommodated by them. Only under very specific stress conditions, i.e. uniaxial stress; and under very specific crystal orientations, i.e. [111]-crystal orientation aligned parallel to the loading direction; the activation of the "soft" slip systems will be inhibited in favor of the "hard" slip systems. Table 2.1 shows the Schimd factors of all given slip systems for a LiF crystal subjected to uniaxial stress along two different crystal directions, the [100]- and the [111]-directions.

2.3 Fabrication of Micro-size Pillars for Micro-compression Testing

2.3.1 A Novel Micropillar Fabrication Approach for Micro-compression Testing

In the following section a novel approach is proposed to fabricate micro-size single-crystal pillars for micro-compression testing. Up to date, most micro-compression experiments are performed on micropillars fabricated by Focused Ion Beam (FIB). However, it is well known that FIB induces ion implantation damage on the surface of the machined specimen and the influence that this ion implantation damage may have on the mechanical response of the specimen is

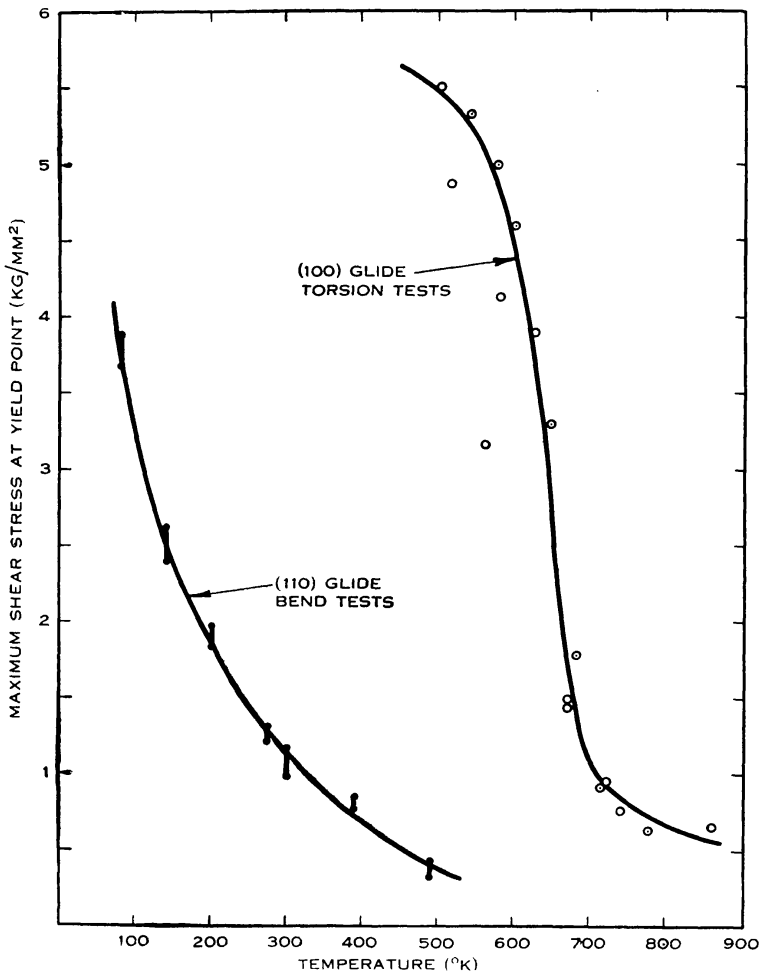

Figure 2.1: Comparison of stress for (100) glide with stress for (110) glide in LiF crystals (Gilman, 1959b).

Table 2.1: Schimd factors for a LiF crystal subjected to uniaxial stress along two different crystal directions, the [100]- and the [111]-directions.

Slip System	(hkl)[UVW]	Schimd factor [100]-direction	Schimd factor [111]-direction
	$(110)[1\bar{1}0]$	0.5	0
	$(1\bar{1}0)[110]$	0.5	0
"Soft"	$(011)[01\bar{1}]$	0	0
(6)	$(0\bar{1}1)[011]$	0	0
	$(101)[10\bar{1}]$	0.5	0
	$(10\bar{1})[101]$	0.5	0
	$(100)[011]$	0	0
	$(100)[0\bar{1}1]$	0	0.47
"Hard"	$(010)[101]$	0	0
(6)	$(010)[10\bar{1}]$	0	0.47
	$(001)[110]$	0	0
	$(001)[1\bar{1}0]$	0	0.47

still under debate. The micropillar fabrication approach presented here shows how to fabricate micropillars without inducing any damage into the specimen, which eventually allows to study the mechanical properties of the material in its as-grown state. Another major advantage of this approach is the large number of specimens (millions) that can be obtained from a DSE sample, which contrasts with the costly process of fabricating FIB-machined micropillars. On the other side, this technique also shows some important limitations —it lacks the FIB-machining flexibility— and only some materials, and at some specific crystal orientations, have been obtained up to date.

As-grown LiF single crystal micropillars were obtained by etching the matrix away in directionally solidified LiF-NaCl and LiF-KCl eutectics. Directionally solidified eutectics (DSE) are multiphase composites fabricated from the melt, which contain large amounts of minority phases distributed as lamellae or fibers

within a matrix phase (Orera et al., 2005). The single crystalline phases grow along well-defined crystallographic directions and orientation relationships are generally established between the component phases to minimize the interfacial energy. The basic microstructure of a simple regular eutectic consists of either single crystal rods or lamellae embedded in a single crystal matrix. When the volume fraction of the minority phase is below 30% it grows in the form of fibers rather than lamellae (Llorca and Orera, 2006).

Directionally solidified LiF-NaCl and LiF-KCl eutectics were produced by the research group led by Prof. Orera at Instituto de Ciencia de Materiales de Aragón, C.S.I.C.-U. Zaragoza. The research group has developed expertise in producing binary eutectic fluorides with well aligned fibrous microstructures. Large eutectic ingots were grown by directional solidification using the Bridgman method. This method involves heating the desired constituents above the melting point until the liquid state is reached and all the constituents are fully mixed. The melt solution is slowly cooled by passing the container through a temperature gradient zone and the material is progressively formed along the length of

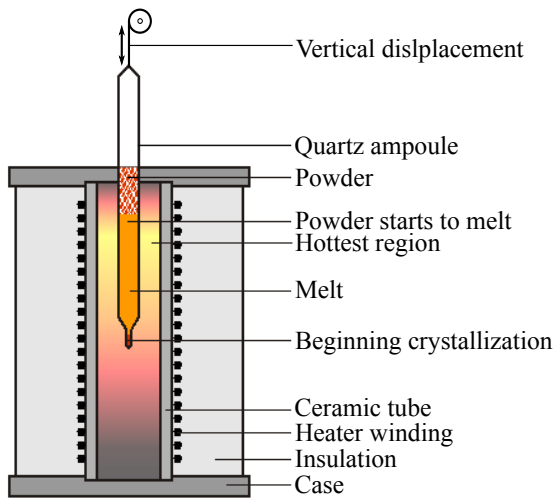

Figure 2.2: Bridgman method setup

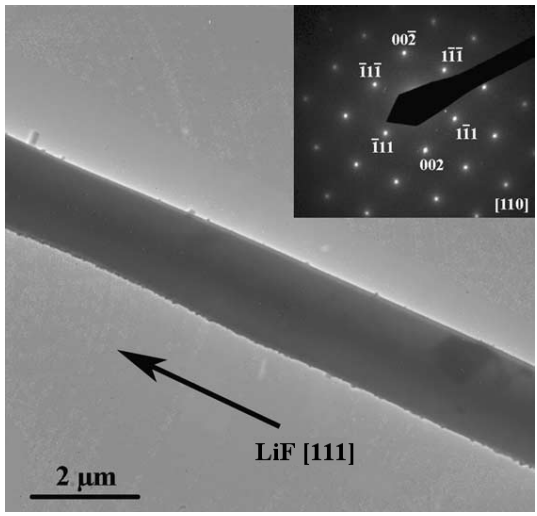

Figure 2.3: TEM image of a narrow LiF fiber obtained from a LiF-NaCl eutectic grown at 50 mm/h. Inset is the electron diffraction pattern showing the [111] orientation of the fiber (Llorca and Orera, 2006).

the container, as schematically shown in Figure 2.2. The eutectic compositions employed were 29 wt% LiF/71 wt% NaCl and 9 wt% LiF/91 wt% KCl. Coupled growth conditions produced a regular microstructure formed by LiF rods aligned parallel to the growth direction (Llorca and Orera, 2006). A representative TEM image and the corresponding electron diffraction pattern of a LiF fiber are given in Figure 2.3 (Orera and Larrea, 2005). The electron diffraction and TEM observations along the fiber length reveal that LiF fibers are indeed single crystals with a general [111] growth habit. The LiF rods occupied 25% and 7% volume fraction in LiF-NaCl and LiF-KCl eutectics, respectively, and were arranged in almost hexagonal pattern, as shown in Figure 2.4. The diameter of the LiF rods was determined by the growth rate, the rod diameter increasing as the growth rate decreased. Eutectics with LiF rods of 5 μm (LiF-NaCl solidified at 3 mm/h) (Orera and Larrea, 2005; Orera et al., 2005), 2.5 μm (LiF-KCl solidified at 10 mm/h), and 1 μm (LiF-KCl solidified at 50 mm/h) diameters were provided. LiF-KCl eutectic was chosen to produce the smallest LiF rods due to the lower

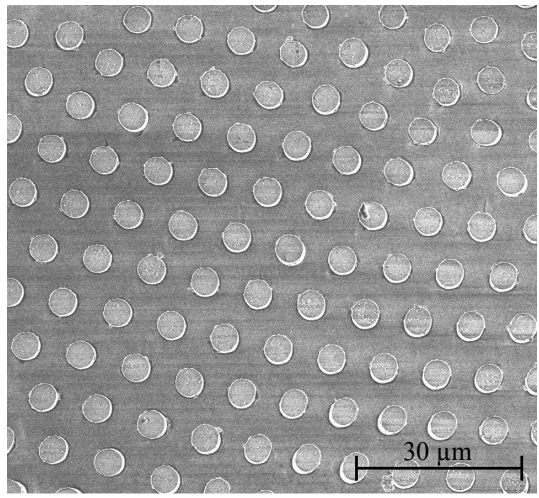

Figure 2.4: Cross-sectional area of a LiF-NaCl eutectic ingot, directionally solidified by the Bridgman method at 3 mm/h. The fibers, around 5 μm diameter, occupy 25% of the volume.

LiF volume fraction present in this eutectic, which generates a less dense and more spaced array of LiF rods, and consequently makes easier targeting single rods on further steps.

Each eutectic ingot was cut perpendicularly to its growth direction in slides of approximately two millimeters thickness, the sample surface being about 1 cm^2 section and containing hundreds of thousands of LiF fibers. Each sample surface was mechanically grounded and polished before etching the matrix away to ensure the smoothest possible fiber surface. As will be shown in the following sections, a good contact between the sample and the compression flat punch tool is critical to obtain successful results. Both, grounding and polishing were done under dry conditions to protect NaCl and KCl phases from dissolving with any aqueous solution (NaCl and KCl have a high reactivity with H_2O, 359 gr/L and 344 gr/L, respectively). Right after, both matrix compositions were etched away with methanol at room temperature. Methanol was chosen because its low reactivity with NaCl (14.9 gr/L) and KCl (5.6 gr/L), providing a very accurate

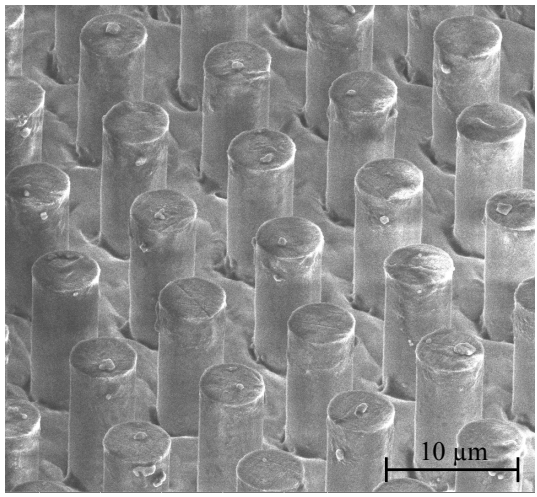

Figure 2.5: LiF-NaCl eutectic sample after matrix etching. LiF fibers are 5 μm in diameter and 10 μm in length.

control of the etching depth. Etching times (between 2 and 10 minutes, depending on the fiber diameter and the matrix chemical composition) were adjusted to obtain LiF micropillars with an aspect ratio (length to diameter ratio) in the range 2:1-2.3:1. This aspect ratio is short enough to suppress buckling during micropillar compression, and long enough to minimize the plastic contribution stress concentrations at the contact area and bottom of the micropillar might generate. The typical appearance of the LiF "forest" obtained after etching the matrix away is shown in Figure 2.5.

2.3.2 Micropillar Fabrication by Dual-Beam (FIB-SEM) System

A dual-beam system incorporates both a focused ion beam (FIB) and a scanning electron microscope (SEM) into a single system. This combination offers several advantages over a single-beam FIB or SEM systems, especially for sample preparation and microscopy applications, in which the ion beam can be used for site specific material removal and the SEM for non-destructive imaging and analysis.

A scanning electron microscope (SEM) is a type of electron microscope that produces images of a sample by scanning its surface with a focused beam of high-energy electrons. A beam of electrons is produced at the top of the microscope by an electron gun and focused toward the sample surface through electromagnetic lenses. When electrons hit the sample a variety of signals are produced that reveal information about the sample morphology, chemical composition, and crystalline structure and orientation of material constituents present in the sample. The types of signals produced by a SEM include: secondary electrons (SE) and back-scattered electrons (BSE) (used to produce SEM images); diffracted backscattered electrons (use to determine crystal structures and orientations); characteristic X-rays (for elemental analysis and continuum X-rays); visible light (cathodoluminescence); and heat. The most common use in SEM is morphology analysis. To obtain an image, the electron beam scans over a selected area of the sample, and the beam's position is combined with the detected signal (SE or BSE) to generate a 2-dimensional image that displays spatial variations in this signal. Modern SEM systems can achieve spatial resolution <1 nm. SEM analysis is considered to be a "non-destructive" technique; that is, electron interactions do not lead to volume loss of the sample, so it is possible to analyze the same area repeatedly without compromising the sample.

Focused ion beam (FIB) systems combine imaging capabilities similar to those of a scanning electron microscope (SEM) with a precision machining tool. The FIB system uses a finely focused beam of ions to scan over the sample surface in a similar way as the electron beam does in a SEM. Most FIB instruments use nowadays Liquid-Metal Ion Sources (LMIS), especially Ga ion sources, as beam source. Source ions are generally accelerated to an energy of 1-50 keV, and focused into the sample surface by electrostatic lenses. The ion beam generated hits the sample and sputters a small amount of material, as either neutral atoms or sputtered ions. The ion beam also produces secondary electrons. As the beam rasters on the sample surface, the signal from the sputtered ions or secondary electrons is collected to form an image of the surface of the sample. FIB systems can be operated at low beam currents for imaging or high beam currents for site specific sputtering or milling. At low beam currents, very little material is sputtered and modern FIB systems can easily achieve 5 nm imaging resolution

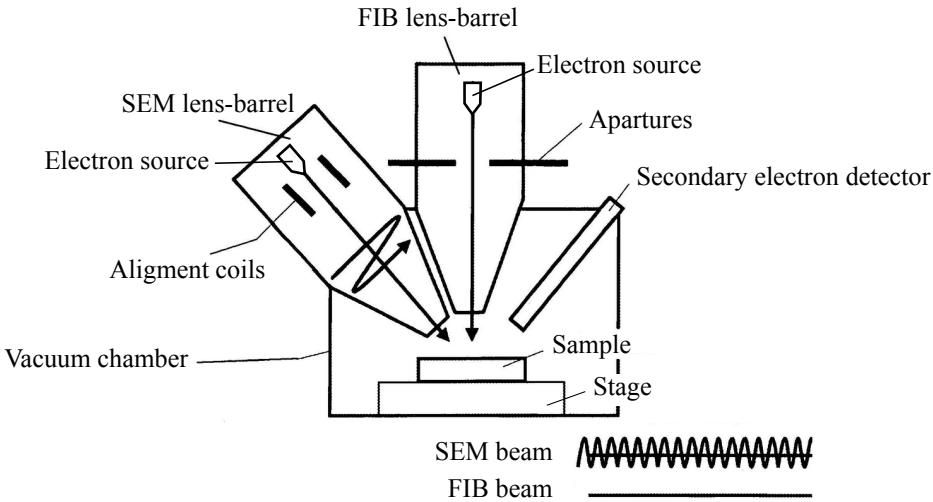

Figure 2.6: Schematic illustration of a dual-beam FIB-SEM instrument.

(Orloff, 1996). At higher currents, big amounts of material can be removed by sputtering, allowing precision milling of the specimen down to a sub micrometer or even a nano scale.

A number of different configurations have been proposed for combining FIB and SEM columns on a single system. Commercial systems began to appear more than 20 years ago. Nowadays, most commercial systems employ a Ga (LMIS) FIB column and a Field Emission SEM (FE-SEM) column. The most common column configuration is to have the electron column place vertically and the ion column tilted, normally 52° with respect to the electron column. The simpler and more compact electrostatic design of FIB columns usually makes it the easier column to mount tilted and still get optimum performance from both columns. Figure 2.6 shows a schematic illustration of a dual-beam FIB-SEM instrument with the ion beam tilted with respect to the vertical.

In this investigation, a Helios 650 dual-beam FIB-SEM system from FEI was used to carry out the sample fabrication process to compare as-grown LiF pillars with FIB-fabricated pillars. The system has a field emission SEM (FE-SEM)

column place vertically and a Ga FIB column tilted 52°. The FE-SEM delivers sub-nanometer resolution across the whole 1-30 kV range (∼0.8 nm). The FIB operates down to 500 V and up to 65 nA beam current.

2.4 Micro-compression by Instrumented Nanoindentation System

Instrumented systems used for micro-compression experiments are usually nanoindentation systems that have been adapted for micro-compression by simply substituting the regular indenter tip for a customize flat-end tip. Nanoindentation systems have been widely used for the mechanical characterization of materials since first nanoindentation equipments began to appear 25 years ago. Since then, the capabilities of this type of equipments has been improved considerably. Nowadays, thanks to the development of new sensors and actuators, the equipments used for nanoindentation testing are capable of measuring contact forces and displacements in the nN and nm range, respectively, in addition to positioning resolutions below 1 μm. The combination of all this capabilities has made nanoindentation a preferred technique for the mechanical characterization on submicron scales.

The most common use of nanoindentation is for the measurement of hardness and elastic modulus (Oliver and Pharr, 1992, 2004), and there has been considerable progress in the measurement of other mechanical parameters as well, including hardening exponents, creep parameters, and residual stresses. There are several reviews on the use of nanoindentation for property extraction (Cheng and Cheng, 2004; Fischer-Cripps, 2002; VanLandingham, 2003). Nanoindentation technology has also served to extend nanoindenter's capabilities to other mechanical tests. Increasing interest has attracted the use of nanoindentation systems for micro-compression testing (see reviews (Greer and De Hosson, 2011; Kraft et al., 2010; Uchic et al., 2009) and references therein).

The basic components of a nanoindentation system are the sensors and actuators used to apply the contact force and to measure the tip displacement, the positioning stage, and the indenter tip. By substituting the regular indenter tip

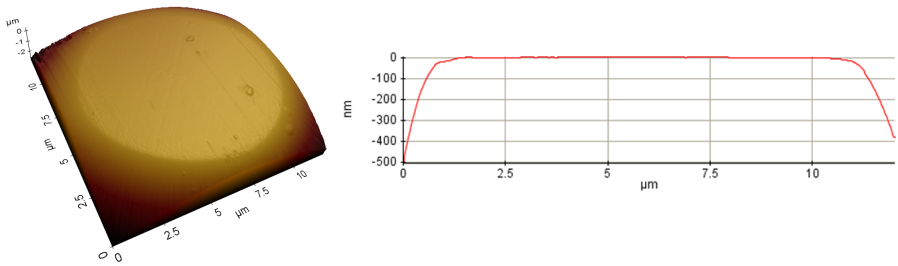

(a) (b)

Figure 2.7: (a) 3D AFM image of a 10 μm diameter flat punch tip. (b) Cross-section profile

for a customized flat punch, one can perform micro-compression test making use of a conventional nanoindentation system. Flat-ended tips are conventionally made of diamond. They are generally fabricated by polishing the apex of previously sharped needles. The quality of a flat punch tip stands for the flatness of its contact area and its alignment with the tip's axis. Figure 2.7 shows an atomic force microscope (AFM) image of a 10 μm diameter flat punch. The topography profile provides an idea of the level of precision achieved in commercial grade flat punch tips.

In this investigation, two types of nanoindentation systems have been used: ex-situ and in-situ systems. Ex-situ nanoindentation systems are self-contained, stand-alone platforms. Usually, instrumentation is held inside an environmentally dedicated enclosure where samples are thermally/acoustically isolated. Some systems have also atmospheric control capabilities, where reduced oxygen/purged conditions can be achieved. In-situ nanoindentation systems are compact test platforms designed to operate inside scanning electron microscopes (SEM) as well as other types of microscopes. Live SEM-imaging capabilities optimize positioning resolution while allowing in-situ materials characterization. The instrumentation on this kind of systems is usually simplified, but they need of third party equipments, like the SEM, to perform adequately. Details on the nanoindentation systems employed are given below.

Ex-situ Nanoindentation System

A commercial TriboIndenter® TI 950 nanoindentation system from Hysitron, Inc. (Minneapolis, MN) was used to carry out ex-situ micropillar compression experiments. The system is a self-contained, stand-alone platform. Instrumentation is held inside an environmentally dedicated enclosure where samples are thermally/acoustically isolated. The system is intrinsically load-displacement controlled. Force is applied electrostatically and displacement is measured capacitively by utilizing a patented design of a three-plate capacitive transducer. A schematic representation of the nanoindentation system set up is shown in Figure 2.8. The system consists of: an enclosure (A), which provides an isolated environment for the instrument; an active vibration isolation system (B), that isolated the equipment from any external vibrations; a rigid frame (C), where every part of the device is set on; a capacitative transducer (D), that transmits and records force and displacement; a positioning stage (E), for sample positioning; an indenter tip (F), which can be exchange depending on testing requirements; and the sample (G).

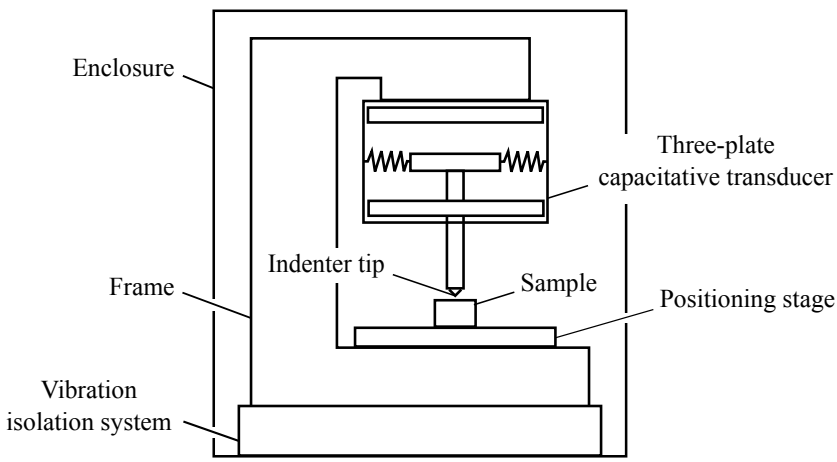

Figure 2.8: Schematic representation of the ex-situ nanoindentation system set up.

In-situ Elevated Temperature Nanoindentation System

The in situ, elevated temperature micropillar compression tests were carried out inside a Zeiss DSM 962 scanning electron microscope (SEM) with an Alemnis In-Situ Indenter, first developed by Rabe et al. (2004), and later modified for operation at elevated temperatures by Wheeler et al. (2013). The in-situ nanoindentation system is a miniaturized test platform for in-situ materials characterization at variable temperatures. It has been designed to operate inside SEM/FIB microscopes. The system is inherently displacement-controlled. Displacement is applied electromechanically by a piezoelectric actuator and force is measured capacitively by a transducer. Temperature is controlled by incorporating tip and sample heating on independent thermocouple-controlled feedback loops. A water-cooling system confines heat and protect sensitive parts from excessive heat flow. A schematic representation of the system set up is shown in Figure 2.9. The system consists of: a rigid frame (A), for mounting on top of the SEM/FIB positioning stage; a piezoelectric actuator (B), for applying tip displacement; a load cell (C), for measuring force; a positioning stage (D), for sample positioning; a sample heater and a tip heater (E), for independent temperature control; a water cooling channel (F), to confine heat flow; and an indenter tip (G) and a sample (H), both with independent thermocouples for temperature measurement.

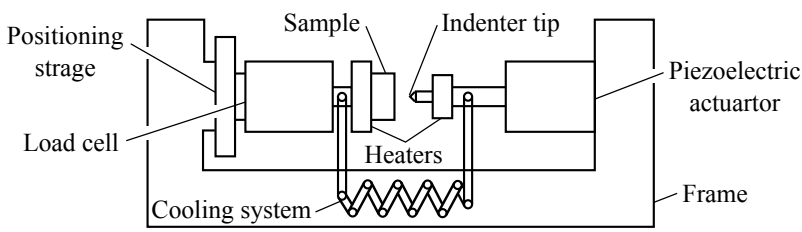

Figure 2.9: Schematic representation of the in-situ nanoindentation system set up.

3

Challenges in the Compression of LiF Single-crystal Micropillars: A Crystal Plasticity Finite Element Analysis

3.1 Introduction

This chapter introduces a numerical analysis of the challenges of compressing LiF single-crystal micropillars, associated to their strong plastic anisotropy. In particular, the study approaches the analysis of three experimental uncertainties which are representative of real micropillar compression tests. These uncer-

tainties are usually associated with the micropillar fabrication procedure or the testing setup: geometrical tilts, lattice rotations, and misalignments between the surfaces of the flat punch and the top of the pillar. The analysis was conducted by means of crystal plasticity finite element (CPFE) simulations. The simulations were carried out with an anisotropic, finite strain, rate-dependent single crystal plasticity formulation implemented in the commercial finite element analysis program ABAQUS (ABAQUS, 2008). The crystal plasticity model implemented follows a classical formulation, and the evolution of critical resolved shear stress (CRSS) is formulated in a phenomenological manner. The plastic properties of LiF were addressed in Section 2.2. The study analyzes two very differentiate crystal orientations, the [100]- and [111]-orientation. These orientations are representative of two extreme behaviors that can be expected in LiF due to its plastic anisotropy. Analyzing the mechanical response of LiF pillars oriented in these two crystal orientations provides valuable information about the plastic behaviour of highly plastic anisotropic materials, showing the influence crystal orientation has in the overall mechanical response of the material. Moreover, this study allows also to relate the extent of potential experimental uncertainties with the crystal orientation of the specimen. Finally, simulation results are compared with available experimental data on LiF [111]-oriented micropillars.

3.2 Experimental Background: Compressive Behaviour of LiF Single-crystals Oriented in the [111]-direction

The compressive response of LiF single-crystal micropillars oriented in the [111]-direction was initially approached experimentally. Micropillars of approximately 5 μm in diameter and 10 μm in length were tested. The micropillar were fabricated by etching away the matrix in NaCl-LiF eutectic compounds, as previously introduced in Section 2.3.1. Compression tests were carried out using a commercial Triboindenter TI 950 nanoindentation system from Hysitron, Inc. (Minneapolis, MN). A flat punch diamond tip of 10 μm diameter was used to apply

the load. The tests were performed under displacement control, with a feedback control loop of 78 kHz, and at a strain rate, $\dot{u}/L$, of approximately 10^{-3} s^{-1}.

Under the above mentioned experimental conditions, micro-compression tests were performed at multiple specimens. LiF micropillars presented a large scatter in mechanical response. Representative stress-strain curves are plotted in Figure 3.1. After the initial elastic region, one set of micropillars presented a non-linear region with continuous hardening until a plateau was reached (marked 1 in Figure 3.1 (a)). Another set of micropillars presented, however, a marked softening shortly after yielding (marked 3 in Figure 3.1 (a)). Finally, micropillars with an intermediate behavior (marked 2 in Figure 3.1 (a)) were also found, in which the softening region started at higher loads, after the micropillar had underwent significant plastic strain hardening. The origin of the differences in mechanical response was evident when the compressed micropillars were observed in the SEM, as shown in Figure 3.1 (b). Micropillars which presented continuous hardening until the maximum strength was attained remained straight upon deformation and two set of slip lines were visible running from the top of the micropillar. On the contrary, micropillars which presented marked softening also showed significant bending in addition to compression upon deformation. The bending component in these samples increased with the amount of softening. The experimental procedure was carefully revised to ensure that this behavior reflected the actual response of the micropillars. Consequently, the presence of bending have to be attributed to small misalignments in the crystal orientation resulting from instabilities during directional solidification (Llorca and Orera, 2006). It should be noted, however, that previous studies (Choi et al., 2007; Raabe et al., 2007) did not report such a large influence of micropillar misalignment on the compressive response, but these results were obtained in metallic crystals (much more isotropic). The hypothesis that the plastic anisotropy of LiF, as reviewed in Section 2.2, was responsible for the variability in the mechanical response and were not a result of experimental distortions motivated the Crystal Plasticity finite element analysis shown below.

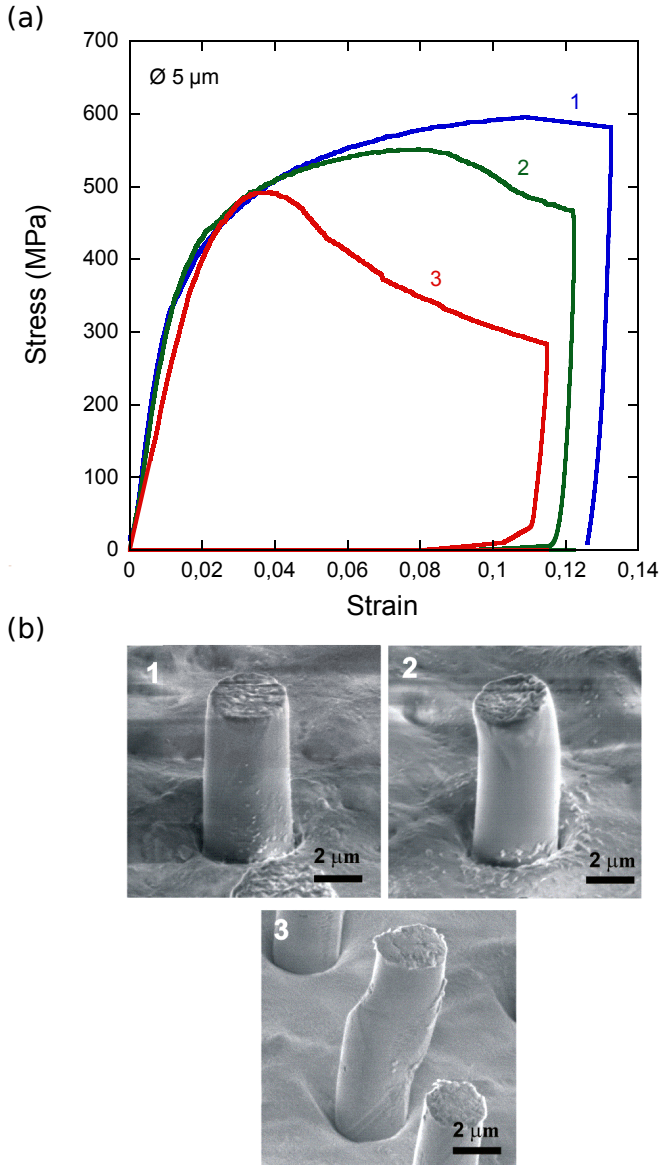

Figure 3.1: (a) Selected stress-strain curves showing the variability in the mechanical response of LiF micropillars oriented in the [111] direction. (b) SEM images of the compressed micropillars, corresponding to the stress-strain curves in (a), showing that bending of the pillar results in a reduced compressive resistance (see curves 2 and 3).

3.3 Crystal Plasticity Framework

3.3.1 Kinematics of Crystal Plasticity

The kinematics of the crystal plasticity model outline here are based on the classical work of Hill and Rice (Hill, 1966; Hill and Rice, 1972; Rice, 1971). Only a brief summary of it is presented here. For a more detailed formulation the reader is referred to their early work and to other classical reviews on crystal plasticity (Asaro, 1983; Roters et al., 2010).

A mathematical description of the crystal plasticity formulation usually starts with the definition of the velocity gradient, L=$(\partial v/\partial x)$, which can be expressed as

$$\mathbf{L} = \dot{\mathbf{F}}\mathbf{F}^{-1} \tag{3.1}$$

followed by the multiplicative decomposition of the deformation gradient, F, into its elastic F_e and plastic part F_p (see also Figure 3.2):

$$\mathbf{F} = \mathbf{F}_e\mathbf{F}_p \tag{3.2}$$

The plastic deformation gradient accounts for the sliding of the crystal lattice along well-defined crystallographic planes. The elastic counterpart, on the other hand, accounts for both the distortion and rigid rotation of the crystal lattice, which can be recovered upon complete unloading of the material. An expression for the plastic deformation gradient can be derived combining equations 3.1 and 3.2

$$\dot{\mathbf{F}}_p = \mathbf{L}_p\mathbf{F}_p \tag{3.3}$$

where the plastic velocity gradient in the intermediate configuration, L_p, is obtained by the sum of the shear rates, $\dot{\gamma}^\alpha$, for each slip system, α, according

to

$$\mathbf{L}_p = \sum_{\alpha} \dot{\gamma}^{\alpha} (\mathbf{s}^{\alpha} \otimes \mathbf{m}^{\alpha}) \tag{3.4}$$

where s^{α} and m^{α} stand for the unit vectors in the slip direction and the normal to the slip plane in the reference configuration, respectively.

3.3.2 Constitutive Model

This section describes the constitutive equations that define the shear rates for any given slip system as a function of the external stress and the microstructural state of the material. In the following, I present the constitutive model implemented in this work, which is based on a phenomenological approach previously introduce by Rice (Rice, 1971), Hutchinson (Hutchinson, 1976), Peirce et al. (Peirce et al., 1982, 1983) for fcc metallic crystals. In this framework the crystal is assumed to behave as an elasto-viscoplastic solid in which the plastic strain rate, $\dot{\gamma}^{\alpha}$, on a given slip system, α, follows a power-law hardening expressed as (Hutchinson, 1976):

$$\dot{\gamma}^{\alpha} = \dot{\gamma}_0 \left(\frac{\tau^{\alpha}}{\tau_c^{\alpha}} \right)^{1/m} \tag{3.5}$$

where $\dot{\gamma}_0$ is a reference shear strain rate and m the rate sensitivity exponent. τ^{α} stands for the resolved shear stress, obtained as the projection of the Kirchoff stress on the slip system α:

$$\tau^{\alpha} = \mathbb{C} \left[\left(\mathbf{F}_e^T \mathbf{F}_e \right)^{1/2} - \mathbf{I} \right] : \mathbf{s}^{\alpha} \otimes \mathbf{m}^{\alpha} \tag{3.6}$$

where $\mathbb{C}$ stands for the elastic stiffness tensor of the crystal, and where Biot strain measure has been chosen to compute elastic strains in the intermediate configuration.

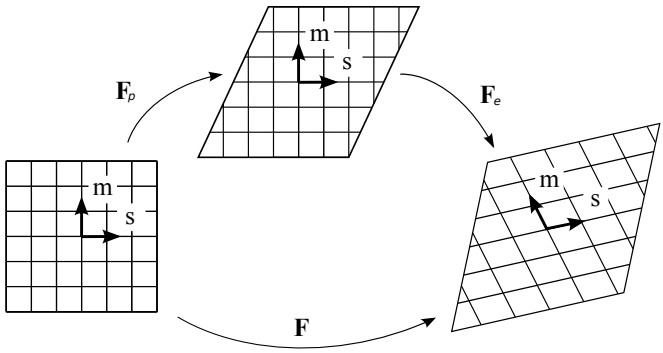

Figure 3.2: Decomposition of the total deformation gradient $\mathbf{F} = \mathbf{F}_e\mathbf{F}_p$.

The evolution of the material state is describe in terms of the critical resolved shear stress, τ_c. The evolution of the critical resolved shear stress, τ_c^α, for a given slip system α, is obtained using the classical hardening model of Peirce et al. (Peirce et al., 1982), formulated as function of the accumulated shear strain, Γ, and the shear rates of all active slip systems, $\dot{\gamma}$:

$$\tau_c^\alpha = h_{\alpha\alpha}(\Gamma)\dot{\gamma}^\alpha + \sum_{\beta\neq\alpha} q_{\alpha\beta}h_{\alpha\alpha}(\Gamma)\dot{\gamma}^\beta \tag{3.7}$$

The first term in the equation is referred as self hardening, and stands for the evolution of τ_c^α due to the interaction of dislocations with the slip system α. The second term is referred as latent hardening, where q is a latent hardening constant, and accounts for the evolution of τ_c^α due to the interaction of dislocations with any other slip system. $h_{\alpha\alpha}(\Gamma)$ is referred to as the hardening modulus,

$$h_{\alpha\alpha}(\Gamma) = h_0 sech \left| \frac{h_0\Gamma}{\tau_s - \tau_0} \right|^2 \tag{3.8}$$

which captures the micromechanical interaction among different slip systems. In

this formulation h_0 is the initial hardening modulus, τ_0 the initial yield stress, and τ_s the saturation yield stress. They are all slip hardening parameters, which are assumed to be identical among the same family of slip systems owing to the underlying characteristic dislocation reactions. Γ is the accumulated shear strain in all slip systems as given by,

$$\Gamma = \int_0^t \left(\sum_\alpha \dot{\gamma}^\alpha \right) dt \tag{3.9}$$

In the literature a number of variations of equations 3.5, 3.6, and 3.7 can be found. Some authors (Becker, 1991) use the sinh function instead of a power-law in equation 3.5, while others (Roters et al., 2010) follow other strain tensor formulations than Biot in equation 3.6, or use (Sarma et al., 1998) modified hardening laws such as a generalized Voce equation (Voce, 1948) instead of equation 3.7.

3.4 Finite Element Model for Micropillar Compression

3.4.1 Finite Element Model

Three-dimensional finite element simulations of the compressive response of highly anisotropic single-crystals were carried out with an anisotropic, finite strain, rate-dependent single crystal plasticity formulation implemented in the commercial finite element analysis program ABAQUS (ABAQUS, 2008). The details of the crystal plasticity formulation implemented were introduced in the previous section. The crystal plasticity code was written in Fortran language and implemented into ABAQUS by means of an ABAQUS User Material (UMAT) subroutine. Simulations were carried out using Abaqus/Standard and within the framework of the finite deformations theory with the initial unstressed state as reference.

Section 2.2 outlined the plastic properties of LiF, which is known to have a high plastic anisotropy due to the well differentiate properties of the two sets

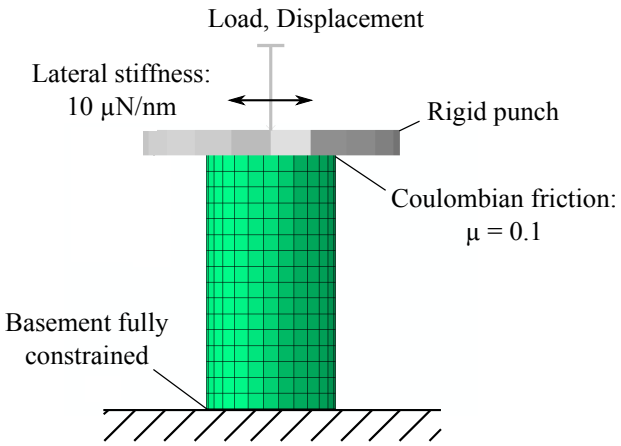

Figure 3.3: Finite element model configuration, showing the mesh and the boundary conditions. The indenter flat punch was modeled as a rigid surface, with a lateral stiffness of 10 μN/nm. A Coulombian friction model was assumed to model the flat punch-cylinder contact. The friction coefficient applied was 0.1.

of slip systems. For LiF, the ratio in critical resolved shear stress between the "hard" $\{100\}\langle 110\rangle$ and the "soft" $\{110\}\langle 110\rangle$ slip systems has being estimated to be between 10-20 (Gilman, 1959a). The study analyzed two different crystal orientations, the [100]- and [111]-orientation. These orientations show antagonistic plastic behaviours, and are representative of two extreme behaviors that can be expected in LiF due to its plastic anisotropy. The [100]-orientation activates 4 "soft" slip systems of the family $\{110\}\langle 110\rangle$, with a Schmid factor of 0.5. All the other slip systems —the remaining 2 slip systems from the "soft" set, and all the slip systems from the "hard" set— have a Schimd factor of zero and consequently are not activated. On the other hand, the [111]-orientation shows plastic activity on 3 of the 6 "hard" slip systems of the family $\{100\}\langle 110\rangle$, with a Schimd factor of 0.47, while non of the slip systems of the "soft" family are activated (see Table 2.1). The analysis of the mechanical response of these two crystal orientations provides valuable information about the plastic behaviour of highly plastic anisotropic materials, showing the influence crystal orientation have in

the overall mechanical response. Moreover, the model allows also to relate the extent of potential experimental uncertainties with the crystal orientation of the specimen.

The 3D finite element model configuration developed for the study was designed to mimic benchmark experimental setups. Micropillars for micro-compression testing are usually fabricated with aspect ratios (length to diameter ratio) of approximately 2:1. In our model, a cylinder of 10 μm in length and 5 μm in diameter was set as the reference configuration. Boundary conditions were fully constrained at the lower base of the cylinder and stress-free at the upper base, where contact will is applied. The flat punch was modeled as a rigid solid, with a lateral stiffness of 10 μN/nm (as encountered in many commercial indenter systems) (Shade et al., 2009). Coulombian friction was assumed to model the contact between the top surface of the cylinder and the flat punch, with a friction coefficient of 0.1. The cylinder was discretized with approximately 1000 eight-node quadratic elements (C3D8 in Abaqus). Figure 3.3 shows a 2-D scheme of the model configuration.

To assess the experimental challenges of compressing highly anisotropic single-crystal like LiF, three potential experimental uncertainties associated with the alignment of the micropillar were analyzed, which are representative of real micropillar compression testing challenges, and are usually associated with the micropillar fabrication procedure or the testing setup. Firstly, the effect of having a small lattice rotation with respect to the intended crystallographic orientation was studied on a geometrically straight micropillar. This is representative of a common inaccuracy found in FIB machined micropillars, as shown in Figure 3.5 (b), and originated at the FIBing stage due to a bulk sample misorientation. Secondly, a pillar with its longitudinal axis perfectly oriented along the intended directions (i.e. [100]- or [111]-direction) but that suffers a geometrical tilt with respect to the loading axis —keeping the head of the pillar parallel to the indenter flat punch— was considered, as schematically illustrated in Figure 3.5 (c). This is representative of micropillars extracted from directionally solidified eutectics, where small misalignments may happen between the fiber growth direction and the ingot solidification direction resulting from instabilities during directional solidification (Llorca and Orera, 2006). This results on both a lattice

rotation, as in Figure 3.5 (b), and a geometrical tilt with respect to the loading axis. Finally, a third case is considered, as shown in Figure 3.5 (d), where the pillar is geometrically tilted with respect to the loading axis, but where the head of the pillar is kept normal to the pillar's longitudinal axis. This is representative of alignment inaccuracies associated with the testing setup, and can be originated by a misalignment on the sample-stage mounting, a misalignment on the flat punch, etc.

3.4.2 Determination of Input Parameters and Finite Element Model Verification

The initial experimental campaign that motivated this numerical study (see section 3.2) was undertaken on LiF single-crystal micropillars. Consequently, the LiF [111]-oriented system was chosen to validate the CPFE model. The three elastic constants, C_{11}, C_{12}, and C_{44}, that define an orthotropic crystal —LiF have a cubic lattice with three orthogonal planes of symmetry (cubic symmetry)— were taken from literature (Hart, 1968) and can be found in Table 3.1. The viscoplastic law that defines the evolution of the plastic strain rate $\dot{\gamma}$ on a given slip system α, as expressed in equation 3.5, follows a power-law hardening. The reference strain rate and the rate sensitivity exponent were given by $\dot{\gamma}_0 = 1\ \mathrm{s}^{-1}$ and $m = 0.1$, respectively. In order to minimize strain rate effects, the applied strain rate $\dot{\epsilon}$ was chosen to be equal to $\dot{\gamma}_0$. The hardening model that defines the plastic evolution of each slip system, according to equations 3.7 and 3.8, was controlled by the parameters $q_{\alpha\beta}$, τ_0, τ_s and h_0. In order to reduce the number of adjustable parameters, the latent hardening coefficients, $q_{\alpha\beta}$, were all set to 1.0, which renders the hardening model isotropic. The rest of hardening parameters, τ_0, τ_s and h_0, are assumed identical for the same family of slip systems owing to the underlying characteristic dislocation reactions, reducing the number of variable by a factor of 6. Summarizing, from all input parameters required to run the model, only three parameters, τ_0, τ_s and h_0, all defining the slip hardening evolution of a given set of slip systems, were used as adjustable constants to fit the experimentally observed behaviour.

As discussed above, a LiF [111]-oriented system shows a very distinct plastic

Table 3.1: Elastic constants of LiF single crystal (Hart, 1968) and parameters that define the evolution of the critical resolved shear stress in each slip system according to equations 3.7 and 3.8 (fitted from experimental results).

Elastic constants			
C_{11} (GPa)	C_{12} (GPa)	C_{44} (GPa)	
114.2	47.9	63.6	

Crystal plasticity parameters			
Slip system	τ_0 (MPa)	τ_s (MPa)	h_0 (MPa)
$\{100\}\langle 110\rangle$	210	360	1400
$\{110\}\langle 110\rangle$	10.5	18	70

behaviour as compared with other LiF system orientations. In this particular orientation, only slip systems of the type $\{100\}\langle 110\rangle$ activate. By fitting our model with experimental data obtained in this [111]-orientation, the number of adjustable constants is reduced by a factor of 2 —from 6 adjustable constants (3 for each set of slip systems) to 3 adjustable constants— which significantly minimizes potential fitting artifacts. Experimental stress-strain curves were taken from micro-compression experiments on 5 μm micropillars. This micropillar size has proven to be large enough to inhibit any undesirable stochastic or jercky behaviour. Only data from micropillars that remained straight upon deformation were used to build a representative stress-strain curve. It is important to notice that initial loading stiffness showed systematically a more compliant response than that observed at the unloading segment (where pure elastic recovery happens), indicating that initial loading was not purely elastic. Figure 3.4 shows together the representative experimental stress-strain curve and the one obtained with the model. The simulated stress-strain curve shows the same initial loading stiffness than its unloading segment. This should be the expected behaviour in an ideal micropillar compression test, where boundary conditions are conside-

red perfect (i.e. perfect pillar-flat punch alignment, perfectly flat pillar surface, etc.). Nevertheless, apart from the initial loading stiffness mismatch, the model perfectly captures the hardening evolution of the material. The values obtained after the fitting were in good agreement with the expected bulk experimental value (Gilman, 1959a), with $\tau_0 = 210$ MPa for the $\{100\}\langle 110\rangle$ slip systems, very close to the 250 MPa estimated in this work, see Figure 2.1. The same constitutive law was assumed for the soft slip systems, but the critical resolved shear stress was reduced by a factor of 20, according to the literature (Gilman, 1959a). The model parameters are summarized in Table 3.1.

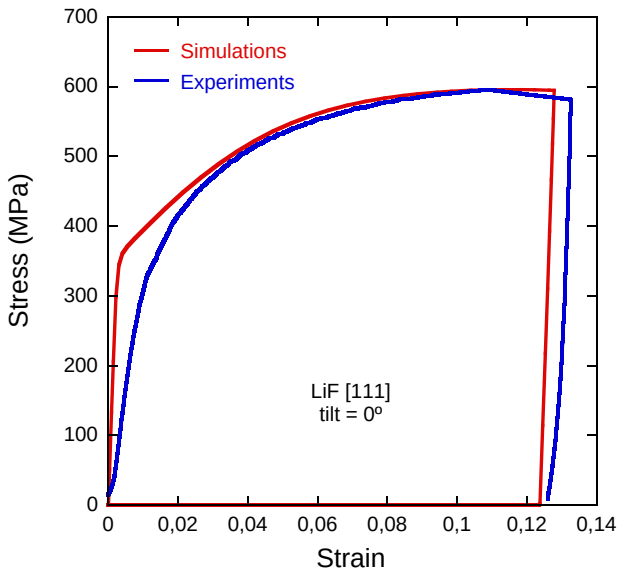

Figure 3.4: Stress-strain curve fitting. Blue line corresponds to a experimental data, red line to the simulation.

3.5 CPFE Analysis of the Compression of Highly Anisotropic Single-crystal Micropillars

3.5.1 Effect of the Crystal Lattice Rotation

The effect of small lattice rotations on a geometrically straight pillar were simulated by rotating the crystal lattice, as shown in Figure 3.5(b). The lattice rotation was varied between 0°, 2°and 5° and the micropillars were deformed up to an engineering strain of 12%. The stress-strain response of the micropillar oriented along the "hard" [111]- and the "soft" [100]-direction are shown in Figure 3.6 (a) and (b), respectively. These results show that small lattice rotations with respect to the intended crystallographic orientation of the pillar have a negligible influence on the compression response of the soft [100]-direction (Figure 3.6 (b)). The flow stress of the perfectly aligned [100] micropillar at 12% engineering strain was 33.9 MPa, indicative of plastic flow in the soft slip system. The flow stress increased less than 1%, up to 35 MPa, when the lattice rotation was 5°. On the contrary, the lattice rotation modified significantly the plastic response of the micropillars oriented in the hard [111]-direction (Figure 3.6 (a)). The initial response was much harder in all cases, indicative of the activation of plastic flow in the hard slip systems, as expected for pillars oriented close to the [111]-direction. However, the lattice rotations led to a dramatic reduction in the flow stress (and to the development of strain softening) in the tilted crystals for engineering strains larger than 4%.

The differences in the stress-strain response can be better understood by analyzing the contour plots of the accumulated plastic strain in three particular slip systems (Figure 3.5): one soft, the $[10\bar{1}](101)$, and one hard, the [110](001), for the [111]-oriented pillar; and one soft, the $[011](0\bar{1}1)$, for the [100]-oriented one. In the case of the micropillar oriented along the [100]-orientation, four symmetric soft slips systems were active, with a Schmid factor of 0.5 (Figure 3.5 (e)). Small lattice rotations decrease the Schmid factors slightly, resulting in the slight increase in the flow stress but without significant changes in the plastic response of the pillars (Figure 3.5 (f)). In the case of the [111]-oriented micropillar, three

symmetric hard slip systems were initially activated, all with a maximum Schmid factor of 0.47 (Figure 3.5 (m)), while the soft slip systems remained inactive because their Schmid factor was 0 irrespective of plastic strain (Figure 3.5 (i)). As a result, the compressed pillar remained initially straight during deformation and the stress-strain curve showed a continuous strain hardening, following the mechanical response of the "hard" slip system. However, a small lattice rotation away from the [111]-direction resulted in small resolved shear stresses on some of the "soft" slip systems that grew as the plastic strain increased. Initially, the Schmid factors in the active "hard" slip systems decreased to some extent, resulting in a slight increase of the flow stress up to certain plastic strain. At this point, even though the resolved shear stresses in the soft slip systems are much lower than in the hard ones, they became active due to the large difference in their critical resolved shear stresses. This occurred at decreasing plastic strains for larger tilt rotations, i.e. 7% and 4% for a lattice rotation of 2°and 5°, respectively. At this point, the micropillar started to bend significantly, leading to a marked reduction in the flow stress as the soft slip systems began to control the deformation of the pillar (Figure 3.5 (j) and (n)). It is worth noting that small lattice rotations did not modify significantly the initial loading stiffness.

The simulation results for the micropillars oriented in the "soft" [100]-direction were similar to previous data obtained in FCC metals (Ma et al., 2006; Zhang et al., 2006), which only showed variations of a few percent in the flow stresses with small lattice rotations. However, the simulation results in the "hard" [111]-direction indicated that small lattice rotations can lead to large variations in the flow stress and in the plastic deformation mechanisms. These results explain the dispersion in the experimental results and highlight the need to be very precise when fabricating single-crystal micropillars of highly plastic anisotropic materials, to ensure a proper crystallographic alignment —better than 2°—, especially when fabricating micropillars in crystallographic directions where "hard" slip systems activate preferentially.

3.5.2 Effect of the Geometrical Tilt

Small geometrical tilts of the pillar with respect to the loading axis were simulated by shearing the cylinder by an angle equal to the tilt, while the top of the pillar remained parallel to the surface of the flat punch, as shown in Figure 3.5 (c). The lattice orientation was assumed to remain aligned with the longitudinal axis of the pillar. Pillar tilts of 2° and 5° were considered and simulations were carried out up to an engineering strain of 12%. Figure 3.6 (c) and (d) depict the stress-strain curves of micropillars oriented in the "hard" [111]- and "soft" [100]-direction, respectively, as a function of geometrical tilt.

Similarly to the crystal lattice rotation case study, the results in the "soft" [100]-direction only depended slightly on the geometrical tilt. The flow stress at 12% engineering strain for a tilt of 5° was only 1% higher than for the perfectly aligned pillar. In contrast, the response in the "hard" [111]-direction was very sensitive to the tilt of the pillar, similarly to the response under pure lattice rotation shown above. The initial response was similar in all cases but the tilt led to a dramatic reduction in the flow stress in the 5° tilted pillar after reaching an engineering strain of 5%, a strain level 1% higher than the one observed above for the initiation of the "soft" slip systems activation at 5° lattice rotation. In contrast, geometrical tilt of 2° did not show any significant flow stress reduction, as did lattice rotation of 2°. In fact, after deforming up to 12% engineering strain, the 2° tilted pillar still maintained an overall straight shape, with "soft" slip systems almost not activated. The contour plots of accumulated plastic strain for the same above mentioned three representative slip systems are plot in Figure 3.5 (g), (k), and (o). Although the final deformed shapes are significantly different, in terms of activation of slip systems, results do not differ much from the ones shown above for the lattice rotation case study. All the description of the activation of different slip systems with the imposed strain applies directly as well in this case study. In addition, note that the geometrical tilt did not influence either the initial loading stiffness (Figure 3.6 (c) and (d)).

These results highlight that geometrical tilt uncertainties are less sensitive to misorientation than crystal lattice rotations ones. Taking LiF as reference material system, any geometrical tilt below 2° would not represent a big concern,

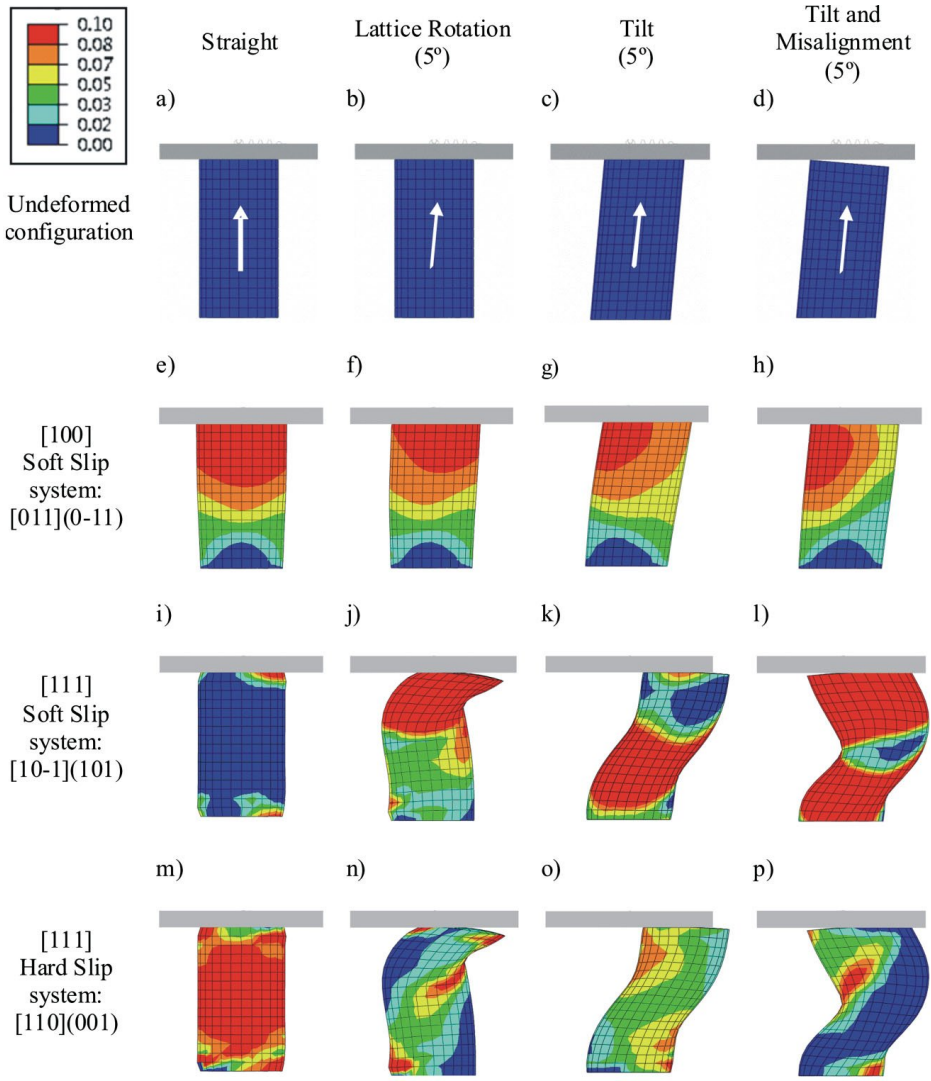

Figure 3.5: Contour plots of accumulated plastic strain in selected soft and hard slip systems after 12% engineering strain for the different case studies shown in (a) perfectly aligned pillar, (b) a lattice rotation of 5, (c) a geometrical tilt of 5 and (d) adding a contact misalignment. (e) to (h) correspond to the [011](011) "soft" slip system in [100]-oriented pillars. (i) to (l) correspond to the [101](101) "soft" slip system in [111]-oriented pillars. (m) to (p) correspond to the [110](001) "hard" slip system in [111]-oriented pillars.

with drops in the flow stress below 2%, a lower value than the expected experimental scatter in this type of experiments. Higher tilts, however, face the risks of a dramatic drop in the flow stress due to likely anisotropic, and consequently unsymmetrical, deformation processes.

3.5.3 Effect of the Contact Misalignment

The last case study simulates the effect of adding a contact misalignment between the top surface of the pillar and the flat punch on top of the geometrical tilt of the pillar. To model the contact misalignment the top surface of the pillar was kept normal to the pillar's longitudinal axis, as shown in Figure 3.5 (d). Thus, when imposing a geometrical tilt to the pillar, the same degree of misalignment in imposed to the contact. The lattice orientation was always assumed to remain aligned with the longitudinal axis of the pillar. Contact misalignment of 2°and 5° were simulated up to an engineering strain of 12%. The stressstrain curves as a function of tilt for [111]- and [100]-oriented pillars are plotted in Figure 3.6 (e) and (f), respectively. The curves showed the combined effect of the geometrical tilt, shown in the previous case, and the stress singularity that takes place at the contact between the top of the pillar and the flat punch. This results on the early plastification of the pillar head, as shown in the contour plots of Figure 3.5 (h), (l), and (p), leading to an apparent reduction of the initial loading stiffness, irrespective of the crystal orientation. The effects of the contact misalignment on the flow stress banish with plastic strain, and the behavior of the pillars resembled that found in the previous case for large plastic strains. Therefore, the "soft" [100]-orientation approaches the behavior of the perfectly aligned pillar for large plastic strains, while the "hard" [111]-orientation is affected by the activation of the soft slip systems, as shown in Figure 3.5 (l) and (p). This example illustrates the difficulty of determining the elastic modulus from the initial loading stiffness in micropillar compression experiments, as slight misalignments between the top of the pillar and the surface of the flat punch are realistically difficult to avoid. This limitation can be overcome by determining the elastic modulus from the unloading segment of the curve, which is not affected by the initial contact misalignments due to the early plastification of the pillar head.

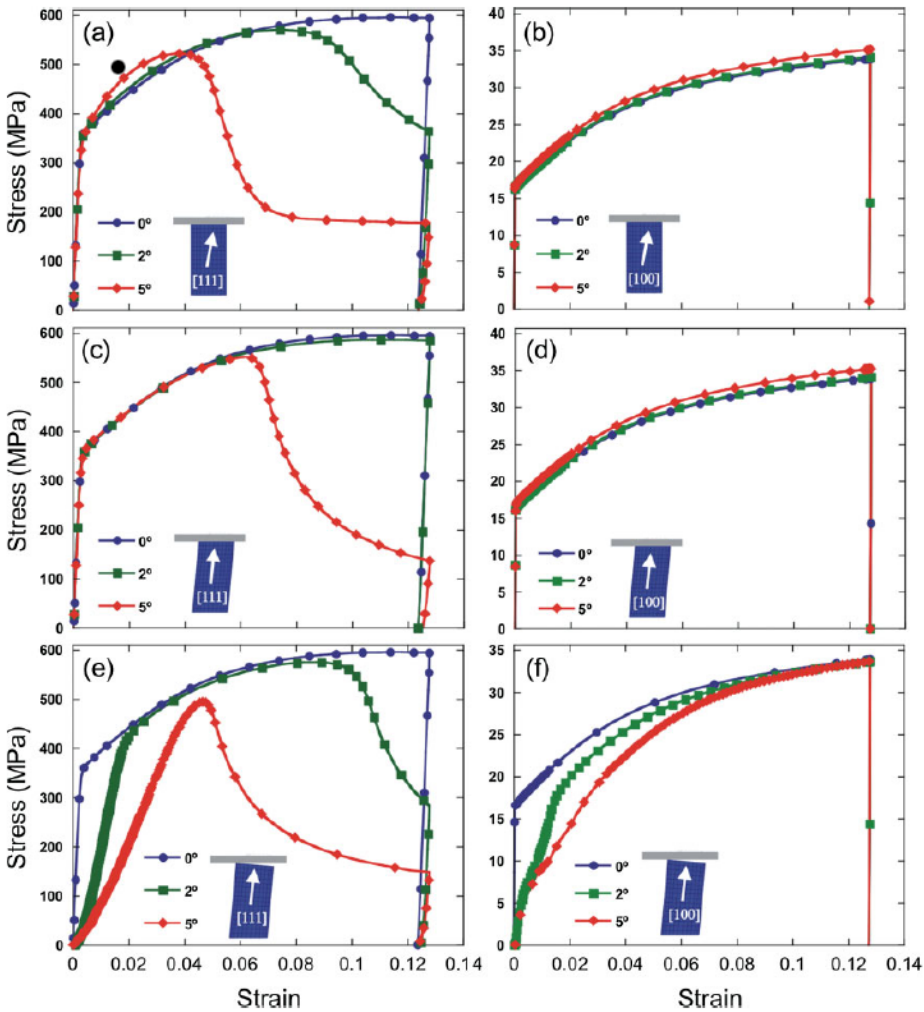

Figure 3.6: Simulated compressive stress-strain curves of LiF single crystals compressed along the [111] orientation, on the left, and the [100] orientation, on the right. ((a) and (b)) Effect of lattice rotation, ((c) and (d)) effect of crystallographic tilt, and ((e) and (f)) effect of crystallographic tilt and contact misalignment.

3.6 Discussion

Let us recover the initial experimental results that motivated the whole numerical analysis. Multiple micro-compression tests were performed on LiF single-crystal micropillars oriented in the [111]-direction. Initially, micropillars presented a large scatter in mechanical response. The origin of the differences in mechanical response was evident when post-morten specimens were analyzed in the SEM, as shown in Figure 3.1 (b). A cause-effect relationship between unsymmetrical pillar deformations and stress levels attained was established: micropillars which presented continuous hardening until the maximum strength was attained remained straight upon deformation; on the contrary, micropillars which presented marked softening also showed significant bending in addition to compression upon deformation and the bending component increased with the amount of softening. The origin of such a large scatter was related to the strong plastic anisotropy of LiF. However, the reason why "soft" slip systems would be activating was still not well understood.

To give insight into this problem, three sources of possible experimental uncertainties were approached by means of CPFE analysis: lattice misorientation, micropillar tilt, and contact misalignment. Direct conclusions extracted from the numerical analysis were that small lattice rotations can lead to large variations in the flow stress and in the plastic deformation mechanisms when highly plastic anisotropic crystal are compressed along directions where only "hard" slip systems are initially activated. This effect seems to be less noticeable when the lattice rotation follows a geometrical tilt of the same extend, having the lattice orientation aligned with the pillar's longitudinal axis. This type of uncertainty would admit small tilts, up to 2°according to the LiF system studied here, without any noticeable effect on the stress-strain response. It was also ascertained the contribution small contact misalignments have in the stress-strain response, decreasing the initial loading stiffness as the misalignment increases, due to the early plastification of the pillar head.

If we take now our initial experimental results and we analyze them again, but taking into account what has been learned from the simulated case studies,

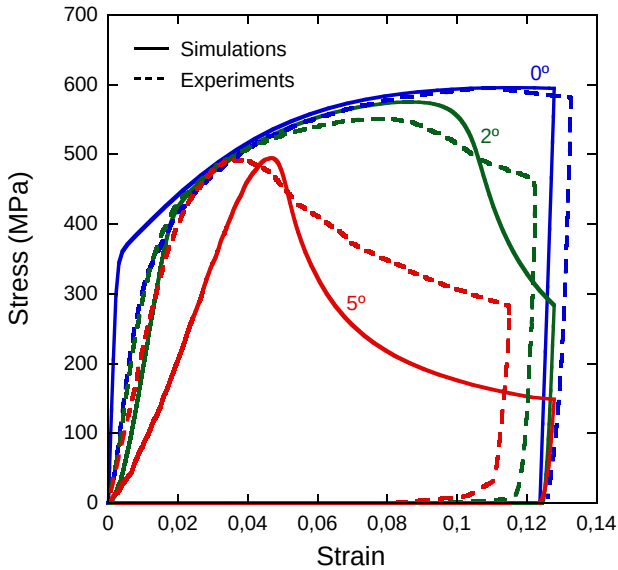

Figure 3.7: Simulated (solid lines) and experimental (dashed lines) compressive stress-strain curves of LiF micropillars. The simulated curves correspond to micropillars with an initial geometrical tilt and contact misalignment of 0°, 2° and 5°.

we can better understand the deformation mechanisms that lead to the different stress-strain responses. Figure 3.7 shows experimental stress-strain results (dashed lines), taken from Figure 3.1 (a), together with simulation results (solid lines) of the third case study, where geometrical tilt and contact misalignment are accounted for, taken from Figure 3.6 (e). This third case study was chosen because is the one that better represents all different plastic deformation mechanisms happening at the micropillar compression tests, as explain as follows.

The first conclusion we can extract from the comparison is that there was a contact misalignment between the micropillar's head and the flat punch. The initial loading stiffness was in all cases more complaint than the theoretically expected value. Previous simulations showed that a decrease in the initial loading stiffness can be originated by a contact misalignment. Moreover, by comparing

simulated and experimental initial loading slopes, we can also obtain an approximate value of what the initial contact misalignment was. According to Figure 3.7, we can estimate that our experiments had a contact misalignment of approximately 2°. Note, in the simulation the misalignment was assumed to happen at the pillar's head, but in the experiments, it may be originated at different places: the flat punch, the pillar's contact area, the stage, etc. Nevertheless, no matter the origin of the misalignment, its influence on the loading stiffness is envisaged to be very similar.

The second conclusion we can extract from the comparison is that when micropillars showed a drop in the stress hardening, no matter which level of strain attained, it was always consequence of an undesired deformation process, and consequently those curve should not be considered in further analysis. Simulation studies showed us how some experimental uncertainties, like small lattice rotations or pillar's tilts, can cause plastic activity on a priori inactive "soft" slip systems. When plastic slip happens at these "soft" slip systems, the strength of the material drops dramatically and specimens start to deform unsymmetrically, showing bending in addition to compression. Thanks to the simulation studies, we can now understand what is happening when a stress drop is registered experimentally: it means that at least one "soft" slip system has been activated. And we can also understand why this is happening: some experimental uncertainties, like small lattice rotations or pillar's tilts, may be present on the test. Thus, the experimental process can be carefully revised to correct, or to improve, those experimental uncertainties causing the scatter; i.e. by correlating experimental and simulated curves in Figure 3.7, we could estimate right after one single test how far the pillar was from being perfectly aligned. And, on top of that, allow us to improve the reproducibility by ruling out, based on well-founded arguments, any curve showing stress hardening drops.

These results highlight the experimental challenges associated with the micropillar compression test in materials which exhibit a marked plastic anisotropy, and provide a rationale to understand the origin of the experimental scatter observed.

3.7 Conclusions

The effect of lattice rotation, micropillar tilt, and contact misalignment on the compression of highly anisotropic single-crystal micropillars has been assessed by means of crystal plasticity finite element simulations. The study was focused in single crystals with a rock-salt (NaCl) crystal structure, like LiF, that present a very anisotropic plastic behavior as a result of the large difference in the critical resolved shear stress between the two sets of slip system, the "soft" $\{110\}\langle 110\rangle$ and the "hard" $\{100\}\langle 110\rangle$ slip systems. Single-crystal micropillars were oriented in two directions, [100]- and [111]-direction. In the former, plastic deformation only takes place on the "soft" $\{110\}\langle 110\rangle$ slip systems, while in the latter plasticity occurs in the "hard" $\{100\}\langle 110\rangle$ slip systems. The results of the numerical simulations showed that a contact misalignment between the micropillar top surface and the flat punch led to a marked reduction in the apparent initial stiffness for both crystal orientations, which was not significantly affected however by either a lattice rotation or a pillar geometrical tilt. From the viewpoint of the plastic response, none of the three cases analyzed led to noticeable differences in the flow stress when the single-crystals were oriented along the "soft" [100]-direction because the plastic deformation was always controlled by the "soft" $\{110\}\langle 110\rangle$ slip systems. On the contrary, all misalignment effects induced a marked reduction in the flow stress (and the development of strain softening) when the single crystal was oriented in the "hard" [111]-direction, due to the activation of the "soft" slip systems even if the Schmid factors were very small. These results highlight the experimental challenges associated with the micropillar compression test in materials which exhibit a marked plastic anisotropy, and provide a rationale to understand the origin of the experimental scatter observed.

4

Size Effects in LiF: The Role of the Intrinsic Lattice Resistance of the Material

4.1 Introduction

In this chapter, the flow stress dependence with the sample size is analyzed as a function of the lattice resistance of the material. The compression of as-grown LiF single-crystal micropillars oriented in the [111]-direction is studied. LiF is a rock-salt ionic compound with a strong plastic anisotropy, as showed in Section 2.2. It has two well differentiated sets of slip systems, one being between 10-20 times harder than the other (Gilman, 1959a). By compressing the crystal orien-

ted in the ⟨111⟩-direction, only the "hard" set of slip systems activates, which drives a material system with a very high slip resistance, of approximately 250 MPa according to Gilman (1959a). The stress-strain response of micropillars in the range 1-5 μm in diameter is studied. A description of the testing methodology employed is provided, together with the compliance correction model applied to compute stress and strain. The size effect in flow stress as a function of the sample diameter for this strong system is finally evaluated. Size effects in FIB-milled LiF micropillars oriented in the same [111]-direction are also studied. The influence of the FIB-milling technique on the size effect is analyzed by comparing both as-grown and FIB-milled micropillar compression results. Finally, these results on the [111]-orientation are compared with the work of Nadgorny et al. (2008) on LiF [100]-oriented, a crystal orientation where only the "soft" slip systems activate, which renders a material system with a slip resistance of approximately 20 MPa. Size effects in this two studies are evaluated as a function of the lattice resistance of the system. To conclude, the analysis is extended to other materials with different intrinsic lattice resistances found in the literature.

4.2 Size Effects in LiF [111]-oriented Single-crystal Micropillars

4.2.1 Micropillar Compression Tests

The challenges of compressing highly anisotropic single-crystals micropillars were addressed in Chapter 3. Initial experimental micro-compression tests conducted on LiF [111]-oriented single-crystal micropillars presented a large scatter in mechanical response, as earlier introduced in Section 3.2. In order to understand the origin of such a large scatter observed, crystal plasticity finite element simulations were conducted trying to mimic experimental tests. Numerical analysis showed the strong variability in mechanical response materials with a high plastic anisotropy may have under some likely experimental uncertainties, namely: geometrical tilt, lattice rotation, or contact misalignment between the flat punch and the top of the pillar. CPFE simulations showed to be a powerful tool to

understand the origin of the experimental scatter observed, providing us the necessary understanding to relate different stress-strain responses —driven by different deformation processes— with initial experimental setup uncertainties (see Figure 3.7). Thus, the experimental process was carefully revised to correct, or at least to improve, those experimental uncertainties causing the initial scatter.

Emphasis was put on improving the sample surface preparation, in order to obtain the smoothest possible sample contact area. The process was revised and polishing steps were adequately refined. Special attention was paid to maintaining eutectic cylindrical ingot parallelism between surfaces while grinding and polishing. Breaking this parallelisms may cause fibers to have a contact misalignment, or even to be mounted tilted with respect to the indenter axis. We also adopted a much more selective policy. Due to the as-grown nature of the micropillars, most of them presented some minor irregularities in terms of circular cross-section, surface roughness, ect. Only those micropillars with very minor irregularities were chosen for compression.

After implementing the improvements on the setup process the scatter was successfully reduced. Occasionally, some micropillars still showed marked softening, no matter the strain level attained. Those micropillars were not considered for the analysis. According to CPFE simulations, this stress-strain response is indicative of plastic slip on at least one of the "soft" slip systems, and should develop unsymmetrical deformation processes. These generates two undesired effects: the slip resistance of the material can not longer be considered high; strain gradients appear as a consequence of unsymmetrical deformation processes. Therefore, only micropillars which presented continuous hardening until the maximum strength was attained and that remained straight upon deformation were considered for the remaining of this investigation.

Compression test conditions were very similar to those on the preliminary experimental campaign (see Section 3.2). Compression tests were carried out using a commercial Triboindenter TI 950 nanoindentation system from Hysitron, Inc. (Minneapolis, MN). Two flat punch diamond tips of 3 and 10 μm diameter were used to apply the load, depending on the sample because the largest punch was too big to avoid contact with neighboring pillars in the samples with the

smallest LiF fibers. The tests were performed under displacement control, with a feedback control loop of 78 kHz, and at a strain rate, $(\partial u/\partial t)/L$, of approximately 10^{-3} s^{-1}. Micropillars of 5 μm, 2.5 μm, an 1 μm in diameter were tested. The micropillar fabrication technique employed to obtain the samples was previously introduced in Section 2.3.1. The initial dislocation density was measured by means of the etch pit density (EPD), calculated as the number of pits per unit area. Etch pit formation can be understood as the preferential nucleation of unit pits at dislocations due to the energy (core energy and elastic strain energy) that is localized there. According to Gilman et al. (1958), who extensively studied the dislocation etch pit formation in LiF, the best dislocation etch pits in LiF are obtained with a dilute aqueous solution of ferric fluoride (FeF_3) ($2{\cdot}10^{-8}$ mole fraction). The effect of ferric ions is to slow the motion of the edges of the pits across the crystal by complexing with fluoride ions of the crystal surface, so that steeper, more visible pits are produced (Gilman et al., 1958). The fibers were etched by soaking them in the etchant and stirring vigorously. After few seconds the fibers were removed and rinsed in alcohol. The EPD was found to be of the order of $2.5{\cdot}10^{13}$ m^{-2}. Figure 4.1 shows the EPD of a 5 μm LiF fiber.

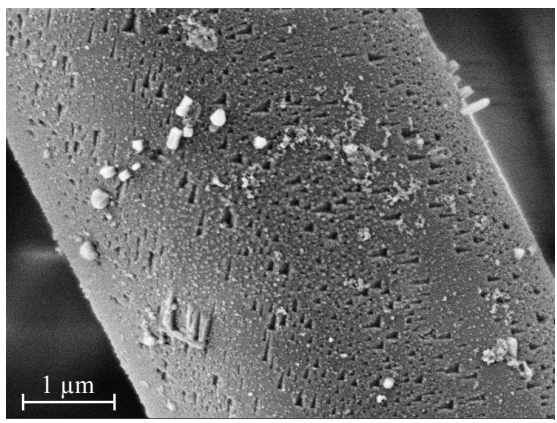

Figure 4.1: 5 μm LiF fiber after ecthing with an aqueous solution of FeF_3 ($2{\cdot}10^{-8}$ mole fraction). Etch pit density (EPD) $\approx 2.5{\cdot}10^{13}$ m^{-2}.

4.2.2 Stress-strain Computations: Necessary System Compliance Correction

When compressing a pillar which is partially embedded into another material, as shown schematically in Figure 4.2, the overall measured displacement reported by the nanoindetation instrument u accounts not only for the deformation taking place along the protruding part of the pillar, but also for the elastic deflection of the surrounding matrix material. Therefore, to correctly compute stress and strain at the pillar, the load-displacement curves reported by the nanoindetation instrument have to be corrected for the extra compliance associated with the elastic deflection of the matrix.

Previous investigations in micropillars manufactured by FIB machining (Greer et al., 2005) used the Sneddon correction (Sneddon, 1965) to account for the sink-in effect at the base of the pillar, assuming that the pillar behaves

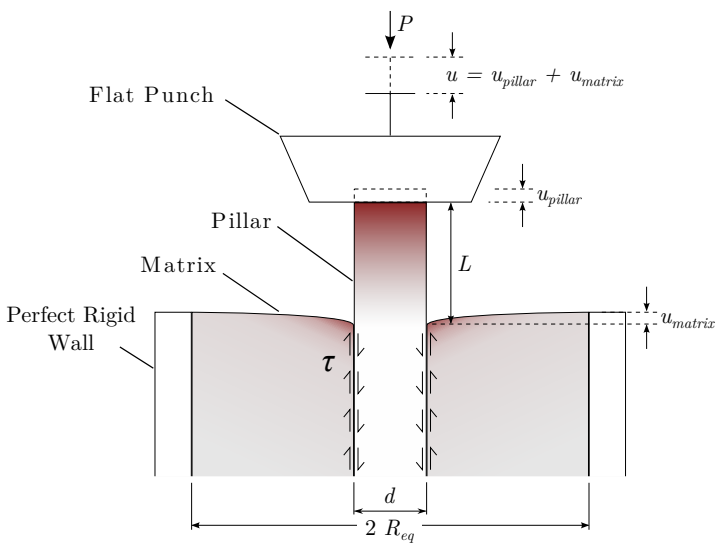

Figure 4.2: Micropillar sample system sketch. The red colored areas represent the relative displacement of the deforming bodies.

as a perfectly rigid flat punch indenting into the supporting substrate. However, this approximation is not valid in this study because the pillar is part of a continuous fiber that is embedded into another material and therefore the load transfer between the pillar and the supporting fiber-matrix composite behaves differently. In this case, the compliance correction was obtained using a standard shear lag model for load transfer between the fiber and the matrix, considering an isolated fiber being embedded into an infinite matrix (Cox, 1952). Assuming a perfect interface between pillar and matrix, the stress on the embedded part of the pillar σ is related to the shear stress at the interface τ according to

$$\frac{d\sigma}{dx} + \frac{4\tau}{d} = 0 \tag{4.1}$$

where d stands for the pillar diameter. Combining with Hooke's elastic law, equation (4.1) can be solved assuming a simple linear relationship between the shear stress τ and the displacement at the interface u_{matrix}, such that $\tau{=}k{\cdot}u_{matrix}$ (Cox, 1952). The overall displacement at the top of the pillar u subjected to a compressive load P is then given by

$$u = \frac{4P}{\pi d^2 E_{LiF}} \left(L + \sqrt{\frac{E_{LiF} d}{4k}} \right) \tag{4.2}$$

where L stands for the length of the protruding part of the pillar, E_{LiF} is the elastic modulus of the pillar, and k is expressed as

$$k = \frac{2G_{matrix}}{d \log\left(\frac{2R_{eq}}{d}\right)} \tag{4.3}$$

under the assumption that the pillar is embedded into a matrix cylinder where the vertical displacement of the matrix is 0 at a distance R_{eq} from the pillar center and where G_{matrix} is the shear modulus of the matrix. Therefore, the total compliance of the pillar can be written according to equation (4.2) as

$$C = \frac{4L}{\pi d^2 E_{LiF}} \left[1 + \frac{d}{L} \sqrt{\frac{E_{LiF} \log(2R_{eq}/d)}{8G_{matrix}}} \right] = \frac{4L}{\pi d^2 E_{LiF}} \left[1 + \frac{d}{L} n \right] \tag{4.4}$$

where n is a constant that depends on the micropillar and matrix elastic moduli ratio and on a geometrical factor R_{eq}. The first term in equation (4.4) corresponds to the compliance of the pillar itself while the second term reflects the elastic deflection of the matrix at the base of the pillar.

In order to test the validity of this model, several pillars were subjected to multiple loading-unloading compression tests to measure the evolution of the pillar's stiffness as a function of the applied displacement u. It was assumed that the volume of the pillar is conserved during deformation, with L being approximated as the difference between the initial pillar length L_0 and the imposed displacement u. Figure 4.3 shows one representative load-displacement curve together with the micropillar stiffness determined from the slope of each unloading segment. The linear increase in stiffness with the applied displacement is perfectly captured by equation (4.4), demonstrating the validity of the model. Note that the measured stiffness is lower than the theoretical value for very small displacements (<100 nm). This discrepancy can be attributed to an extra compliance during the first stages of the test until full contact is established between the flat punch and the top of the pillar, as further discussed in Chapter 3.

Thus, according to equation (4.4) the displacement contribution associated with the elastic deflection of the matrix u_{matrix} can be now calculated independently. The true displacement of the pillar u_{pillar} is obtained by subtracting u_{matrix} to the measured displacement u, such that $u_{pillar} = u - u_{matrix}$. Once the true displacement of the pillar u_{pillar} is known, pillar's true stress and true strain are obtained as

$$\sigma = \frac{P}{A_0} \left[1 - \frac{u_{pillar}}{L_0} \right] \quad and \quad \varepsilon = ln \left(\frac{L_0 - u_{pillar}}{L_0} \right) \tag{4.5}$$

where L_0 and A_0 are the pillar's inital length and cross-sectional area, respectively. For both as-grown and FIB machined micropillars, A_0 is taken as the top diameter of the pillar.

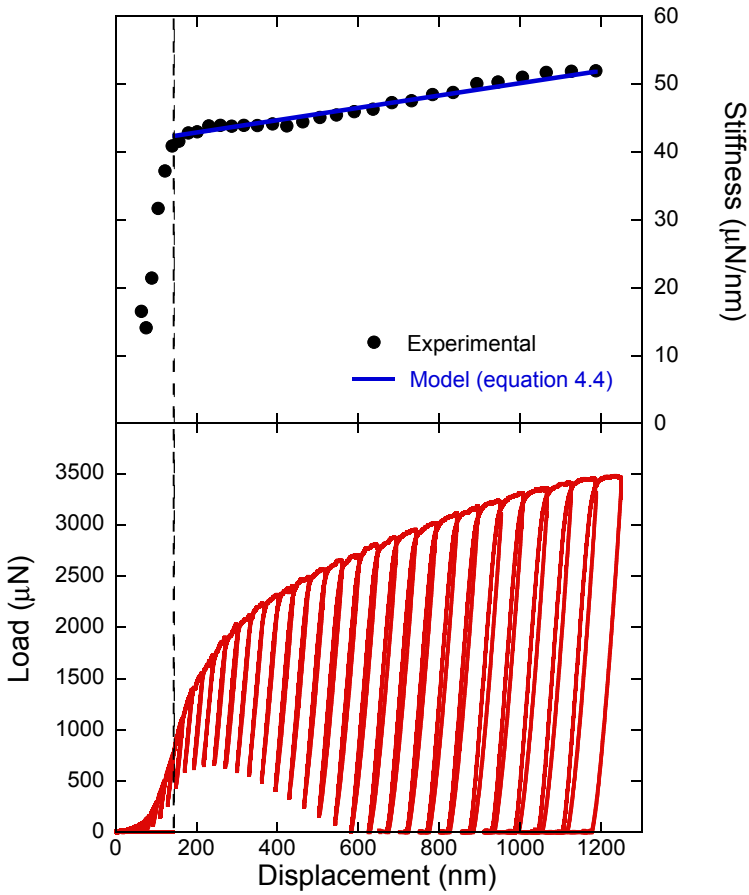

Figure 4.3: Evolution of the stiffness of a micropillar of 2.5 μm in diameter as a function of the applied compressive displacement. The experimental stiffness was determined from the slope of the of the load-displacement segment during unloading and is compared with the theoretical value given by equation (4.4).

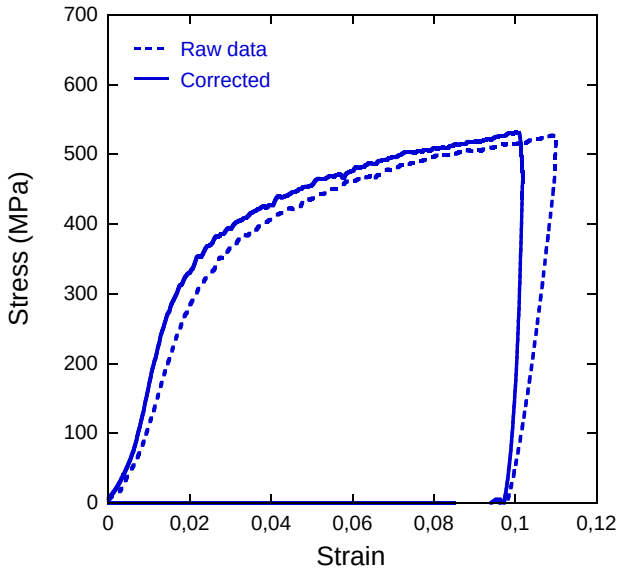

Figure 4.4: True stress-strain curve of a micropillar of 5 μm in diameter computed with and without including the matrix compliance correction.

It should also be noted that this stiffness correction has a marginal effect on the stress-strain curve, as shown in Figure 4.4. In fact, these curves demonstrate that the matrix behavior does not significantly influence the micropillar compression tests. Nevertheless, the stiffness correction is important for a precise determination of the micropillar elastic modulus from the unloading segment of the load-displacement curve, leading to values very close to 146.5 GPa, the reported value for LiF in the [111] direction (Hart, 1968). In most cases, the initial elastic loading segment (Figure 4.4) is more compliant than the final unloading one, very likely due to the contact issues mentioned above. This fact made difficult to establish a yield stress from the stress-strain curve. To overcame this problem, the flow stress at 5% strain, $\sigma_{5\%}$, is used throughout this investigation as the characteristic value to compare the compressive strength of different pillars, as it is commonly done in other micropillar compression studies.

4.2.3 Stress-strain Response as a Function of Sample Size

Under the above mentioned experimental conditions (see Section 4.2.1), micro-compression tests were performed on micropillars of 5 μm, 2.5 μm, and 1 μm in diameter. Multiple specimens were tested for each micropillar size. Chapter 3 showed us the influence initial tilt/misalignments have in the compression behavior of LiF [111]-oriented micropillars. As justified in Section 4.2.1, only those micropillars that presented continuous hardening until the maximum strength was attained were used for this investigation. This led to a very good reproducibility in the mechanical response for all micropillar diameters with a noticeable increase of the scatter for the 1 μm pillar diameter. Figure 4.5 (a)-(c) plots compressive stress-strain curves of as-grown micropillars of 5 μm, 2.5 μm and 1 μm in diameter, respectively. The evolution of the flow stress at 5% strain, $\sigma_{5\%}$, as a function of micropillar diameter is plotted in Figure 4.5 (d). The plots do not show any noticeable size effect on the mechanical response of LiF [111]-oriented micropillars in the range of pillar diameters studied. The flow stress at 5% strain was around 500 MPa in all cases.

The larger scatter, together with the more jerky behavior, of the stress-strain curves of the 1 μm pillars is consistent with the experimental evidence in metallic micropillars of a progresive exhaustion of dislocation sources (Ng and Ngan, 2008a,b,c; Ngan and Ng, 2010). The number of available dislocation sources decreases with the micropillar diameter, and a transition is found in the stress-strain curves for a critical micropillar size. Micropillars larger than the critical size present smooth stress-strain curves and limited scatter while the stress-strain curves of micropillars below the critical size present strain instabilities and more scatter. The former correspond to micropillars of 5 μm and 2.5 μm in diameter in Figure 4.5 (a) and (b), while the latter stands for the response of micropillars of 1 μm in diameter in Figure 4.5 (c). It should be noticed, however, that size effects were not observed in the range of pillar diameters studied (1-5 μm) in LiF micropillars compressed along the [111]-direction.

The fact that micropillar compression of LiF [111]-oriented yields plastic deformation and not fracture is an indication that the small size suppressed cracking, as shown elsewhere (Östlund et al., 2011), and highlights the benefit

of using micropillar compression to study plasticity in brittle materials without the need of using complex tests, like compression under confining pressure. The measured flow stress of ≈500 MPa leads to an estimation of the critical resolved shear stresses for the "hard" slip systems of the order of 250 MPa, which is reasonable for bulk LiF (Gilman, 1959a), although the exact value is very sensitive to impurities and dislocation density. This result is in agreement with the lack of a size effect on the flow stress of LiF [111]-oriented micropillars observed in this work.

4.3 Influence of FIB Machining on Size Effects

4.3.1 Fabrication of FIB-milled Micropillar

FIB-milled LiF micropillars were produced by further micro-machining by FIB of the previously obtained as-grown LiF micropillars. A few among the hundreds of thousands of as-grown micropillars produced (as those shown in Figure 2.5 (b)) were selected for FIB-milling. A FIB FEI Helios 650 Dual Beam system was employed for the milling. Standard working conditions, with a Ga^+ ion accelerating voltage of 30 keV and beam currents in the range 7.7-40 pA, were used. The milling technique employed to machined the micropillars was annular milling. In general, annular milling provides the ideal beam scanning strategy for any kind of circular structure down to the nanometer scale: the ion beam follows the circular shape of the nanostructure to be generated.

The fabrication process consists of two steps. First, the surface of the sample is oriented normal to the FIB column, and a pillar is located using FIB imaging, as shown in Figure 4.6 (a). With the pillar perfectly centered, a concentric annular milling pattern is used to make a coarse milling, as shown in Figure 4.6 (b). This step was performed using an ion current of 40 pA, since the goal was to quickly remove material. The second step consist of performing a finishing milling or fine milling. This step was performed using an ion current of 7.7 pA. These beam currents are comparable to the values reported in the literature for micropillar fabrication using FIB (Kiener et al., 2006; Korte and Clegg, 2011; Nadgorny et al., 2008; Ng and Ngan, 2008a,b,c; Östlund et al., 2011; Uchic and

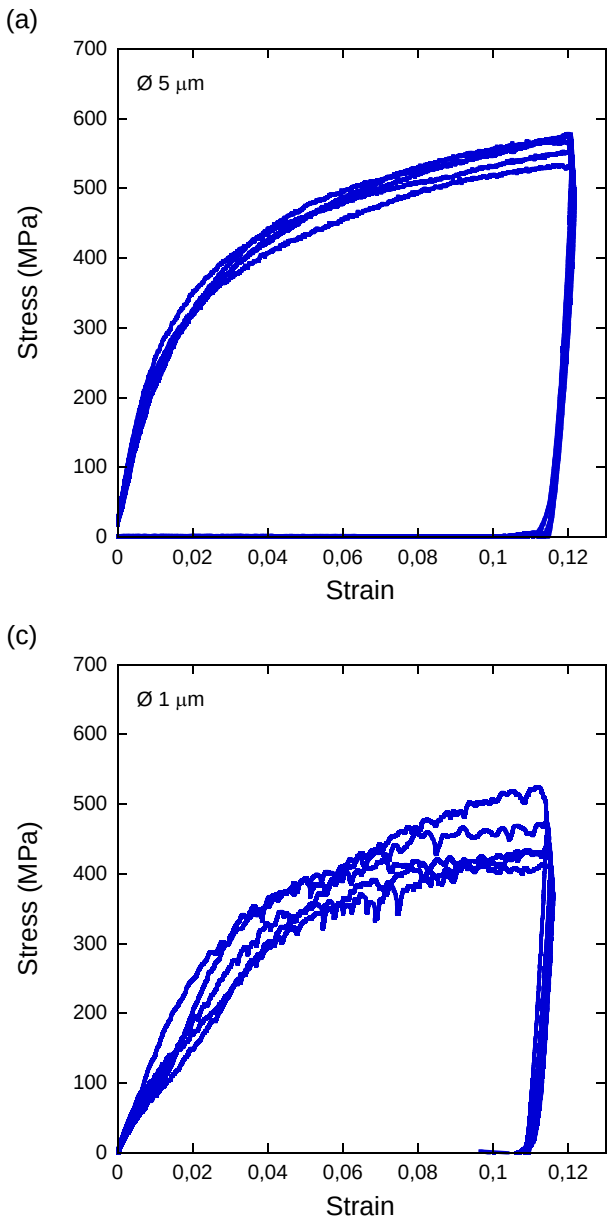

Figure 4.5: Compressive stress-strain curves of micropillars of (a) 5 μm, (b) 2.5 μm and (c) 1 μm in diameter, respectively. (d) Flow stress at 5% strain, $\sigma_{5\%}$, as a function

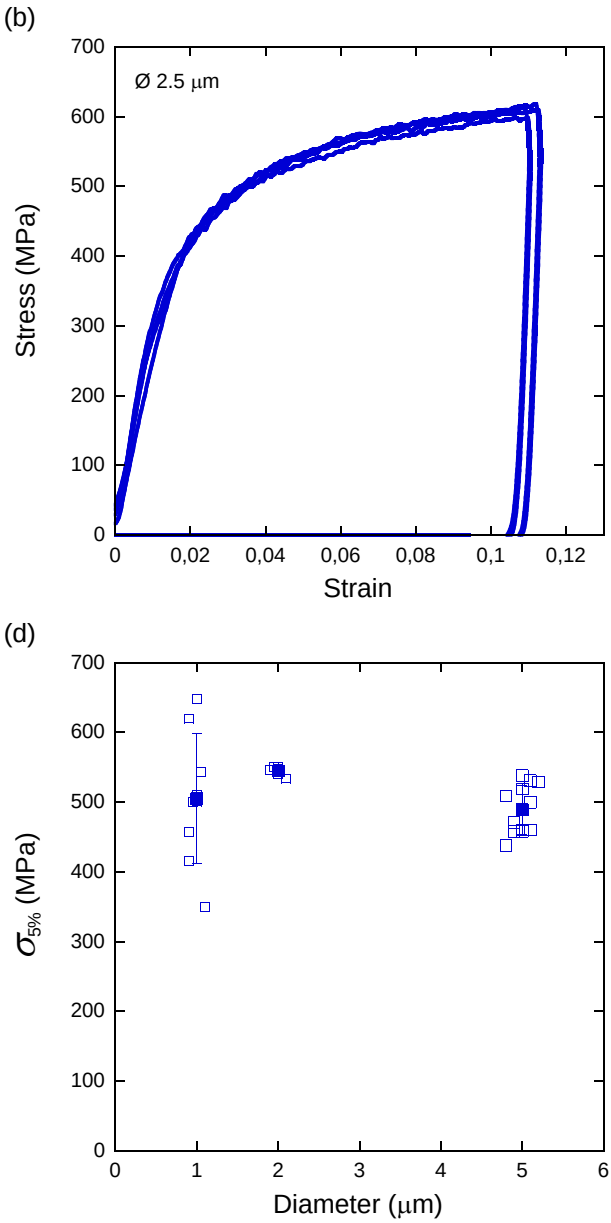

of micropillar diameter.

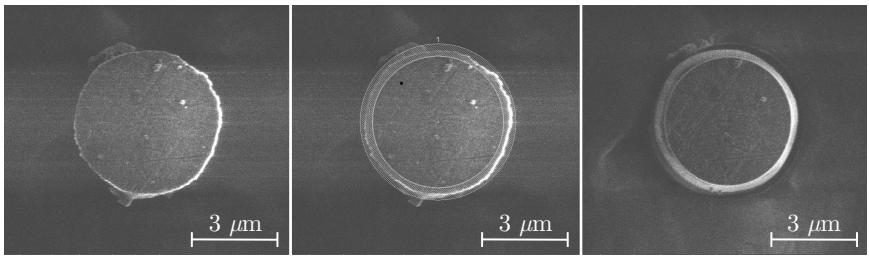

Figure 4.6: Annular milling process. Micropillar top view (FIB imaging): (a) before ion irradiation; (b) with the annular milling pattern used; (c) after ion irradiation.

Dimiduk, 2005). Note, with lower beam currents the spot size and lateral spread of the ion beam improve considerably, thus a better surface finishing can be obtained. The beam speed is directly related to the dwell time. Dwell times of 50 and 500 msec were used, for beam currents of 7.7 and 40 pA, respectively. The milling always started at the outer diameter and sequentially moved to smaller diameters. Milling times between 60 and 330 sec were obtained, depending on the milling step and pattern size. Live SEM- and FIB-imaging were used occasionally in order to ensure that the milling pattern was ideally located within the micropillar. Figure 4.6 (c) shows a pillar after ion irradiation using FIB imaging. All micropillars were imaged before and after ion irradiation in order to measured initial and final upper diameter, and tapering angle. Figure 4.7 shows SEM images of micropillars of 5 μm, 2.5 μm, and 1 μm in diameter, before and after ion irradiation. The FIB-milled micropillars present tapering angles of 2-3°, as expected from the annular milling process. These values are in agreement with the tapering angles published in the literature for micropillars manufactured by the annular milling technique (Korte and Clegg, 2011; Shim et al., 2009; Zhang et al., 2006).

4.3.2 Size Effects in FIB-milled Vs. As-grown LiF Micropillars

Micro-compression tests on FIB-milled LiF micropillars were performed following the same experimental conditions applied for the as-grown micropillars in

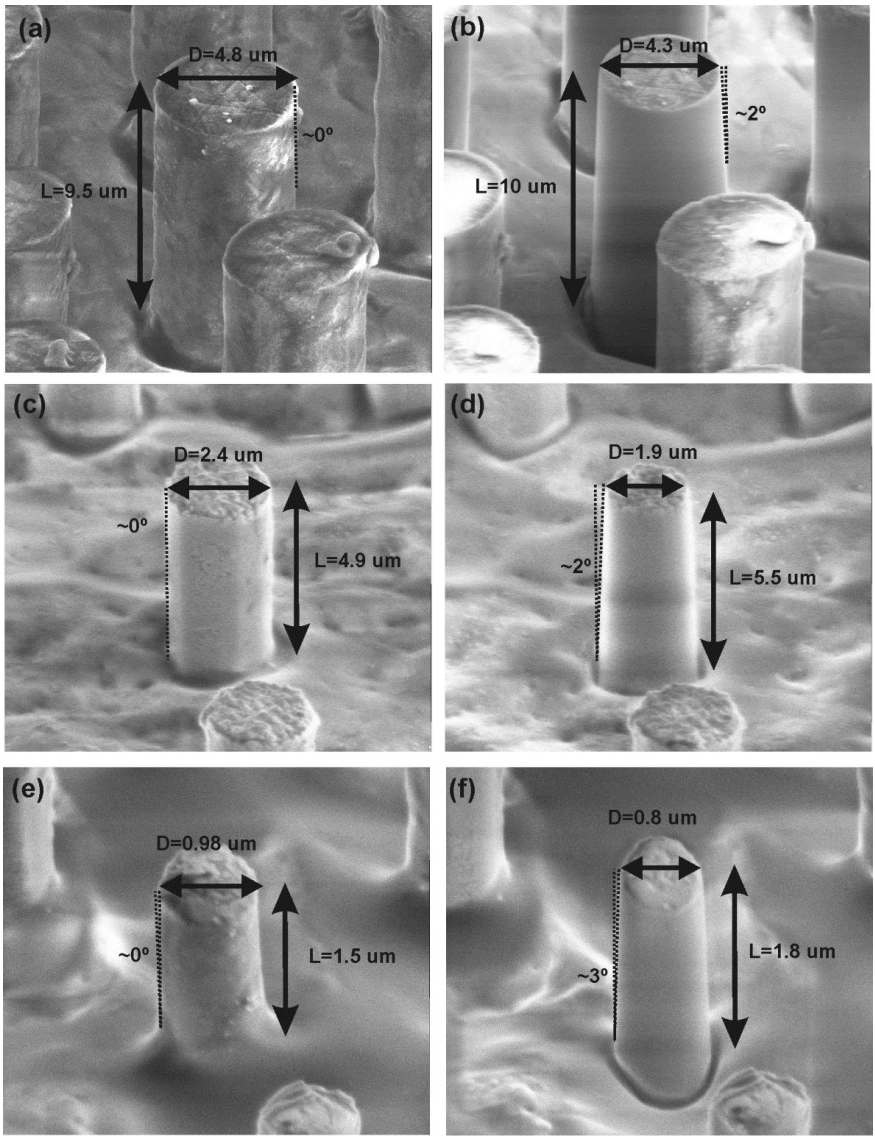

Figure 4.7: SEM images of representative micropillars: (a) and (b) correspond to micropillar of 5 μm in diameter before and after FIB irradiation, respectively. (c) and (d), idem for micropillars of 2.5 μm in diameter and (e) and (f) idem for micropillars of 1 μm in diameter.

Section 4.2.1. Micropillars of 5 μm, 2.5 μm, and 1 μm in diameter were tested. Note after the FIB-milling process, the nominal diameter of each sample size was slightly reduced. In the stress-strain computation, these reduction was accounted for by computing the cross-sectional area as the upper diameter. Multiple specimens were tested for each micropillar size. The same criteria than in the as-grown micro-compression campaign was followed to reduced the scatter, and only micropillars that presented continuous hardening until the maximum strength was attained were considered for the study, as explained in Section 4.2.1. This led to a very good reproducibility in the mechanical response for all micropillar diameters with a noticeable increase of the scatter for the 1 μm pillar diameter. The same behaviour as that found for the as-grown micropillars was observed. Representative stress-strain curves of micropillars of 5 μm, 2.5 μm and 1 μm in diameter subjected to ion-irradiation are plotted in Figure 4.8 (a)-(c), respectively, together with their corresponding stress-strain curves in the as-grown state. As explained in Section 4.2.3 the larger scatter, together with the more jerky behavior, of the 1 μm pillars is related with the available number of dislocation sources, that decreases with the sample size, finding a transition for a critical micropillar size where the stress-strain behaviour no longer present a smooth response. The flow stress at 5% strain, $\sigma_{5\%}$, of as-grown and ion irradiated micropillars is plotted in Figure 4.8 (d), as a function of the micropillar diameter. It shows that ion irradiation increased the flow stress by approximately 30% in all cases. This result is in agreement with previous observations in bulk LiF which have established that the bulk yield stress of LiF is very sensitive to ion irradiation (Johnston and Gilman, 1959).

4.4 Discussion

Our results contrast with previous studies that have shown strong size effects in the plastic deformation of FCC metals (Greer et al., 2005; Uchic et al., 2004; Volkert and Lilleodden, 2006) and ionic compounds (Dimiduk et al., 2010; Nadgorny et al., 2008). In particular, Nadgorny et al. (2008) reported a strong size effect in [100]-oriented LiF micropillars fabricated by FIB when the micropillar

diameter was in the range 1-10 μm. The discrepancies between these results and those reported in this work can be attributed to three causes: differences in the initial dislocation density, FIB machining, and crystal orientation.

The LiF [100]-oriented micropillars of Nadgorny et al. (2008) were machined from bulk crystals with a very low initial dislocation density (10^9 m^{-2}) but it should be noted that the real dislocation density on the FIB-machined micropillars was likely to be much higher than that of the bulk crystals because of the effect of ion irradiation. Otherwise, the micropillars would have been virtually dislocation-free, displaying a whisker-type behavior, which was not the case. Our LiF [111]-oriented pillars were not produced from bulk crystals, but by directional solidification of an eutectic mixture. The initial dislocation density was determined by EPD, showing an approximately value of 10^{13} m^{-2}, a much higher value than that found in the bulk crystal. The measured value seems to be rather high for an undeformed crystal. However, the existence of such a initial dislocation density can be explained by the differences in the thermal expansion coefficients of the two eutectic phases, that developed thermal residual stresses upon cooling. Moreover, the fact that these micropillars did not display a whisker-type behavior, controlled by the nucleation of dislocations (as the one observed in the Mo micropillars of Bei et al. (2008), corroborate the existence of an elevated initial dislocation network. Thus, both LiF micropillars in Nadgorny et al. (2008) and in this investigation contained a network of mobile dislocations prior to testing, which eventually predispose to the same kind of dislocation mechanisms, although their initial densities were dissimilar.

Another possible origin of the differences may be FIB milling. Previous studies in metals have reported that FIB machining leads to Ga^+ ion implantation and to the formation of dislocation networks within a damaged surface layer of several nanometers in depth (Kiener et al., 2007), but that these surface defects are driven out by mechanical annealing upon loading, at least in sub-micron pillars (Shan et al., 2007). As a result, the extended view points to the conclusion that the effect of FIB milling on metallic micropillar compression is negligible provided the pillar has some initial dislocation structure before milling (El-Awady et al., 2009), that provides an initial distribution of dislocation sources. This way the truncation of dislocation sources originates the size effects (Akarapu et al.,

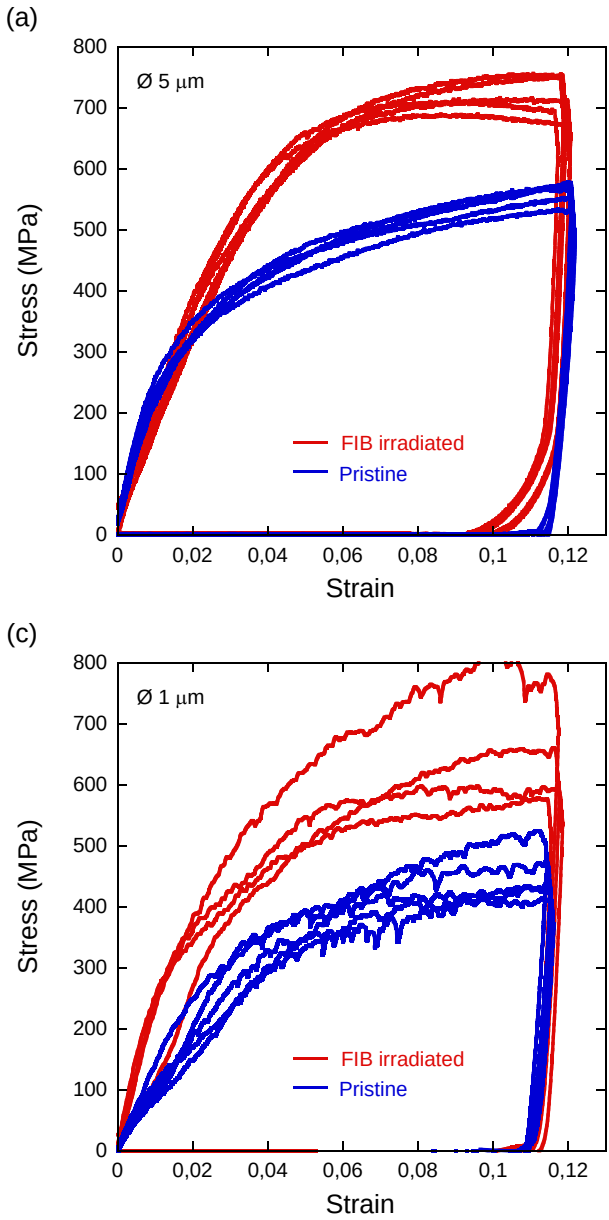

Figure 4.8: Compressive stress-strain curves of micropillars of (a) 5 μm, (b) 2.5 μm and (c) 1 μm in diameter, respectively, before and after ion irradiation. (d) Flow stress

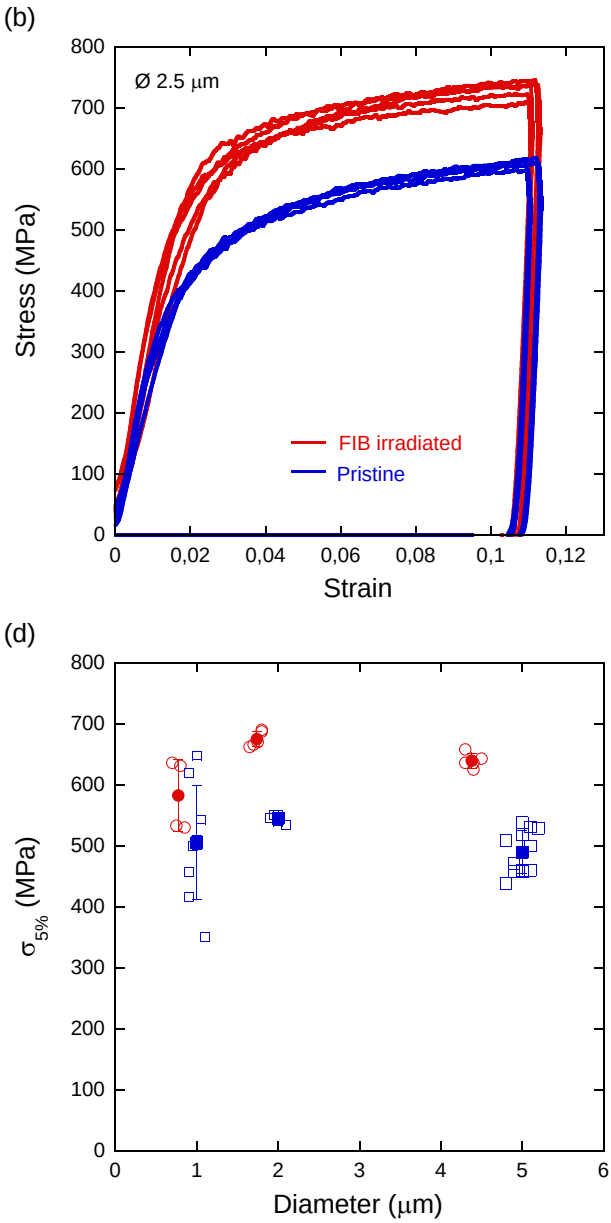

at 5% strain, $\sigma_{5\%}$, as a function of diameter for as-grown and ion irradiated micropillars.

2010; Ngan, 2011; Parthasarathy et al., 2007; Rao et al., 2008). Recent studies in mechanically pre-strained Mo pillars, both with (Schneider et al., 2010) and without FIB milling (Shim et al., 2009), support this view, because size effects are independent of whether the initial defect distribution is due to FIB machining or mechanical pre-strain. This seems also to be the case for the [100]-oriented LiF micropillars, but not the for [111]-oriented LiF pillars reported in this work.

On the contrary, our work shows that the flow stress of [111]-oriented LiF pillars, both in the as-grown and FIB-machined condition, is independent of pillar size and that FIB machining increases the flow stress by approximately 30%, for all pillar diameters. Even though the type of defects that FIB machining introduces in ionic compounds has not been documented up to date, our results point to the conclusion that the mechanical behavior of the [111]-oriented micropillars is not controlled by the distribution of dislocation sources. The origin of this discrepancy has to be found in the high bulk lattice resistance to dislocation glide of active slip systems in the [111]-oriented LiF micropillars. In the case of [100]-oriented LiF micropillars, compression takes place by the activation of the "soft" slip systems, while LiF micropillars perfectly oriented along the [111]-direction deform in compression by plastic deformation along the "hard" slip systems. The critical resolved shear stress obtained by us in LiF [111]-oriented micropillars and by Nadgorny et al. (2008) in LiF [100]-oriented micropillars are plotted in Figure 4.9 as a function of micropillar diameter. Representative values for the bulk critical resolved shear stresses for the "soft" and "hard" slip systems are indicated as reference (Gilman, 1959a; Johnston and Gilman, 1959). The direct comparison of these values with those obtained from micropillar compression should be done with care since they depend on impurity level, dislocation density and strain rate, and the former is not known in the micropillar compression tests. That is why the bulk values are indicated as a range in Figure 4.9. The data in Figure 4.9 suggest that the size effect depends on the magnitude of the bulk shear yield stress, so that the higher the bulk shear yield stress the lower the size effect. This hypothesis was first advanced by Korte and Clegg (2011), as they found a similar behavior in MgO [100]- and [111]-oriented micropillars, a material with the same crystal structure than LiF.

Let us recall the empirical law commonly used to represent size effects:

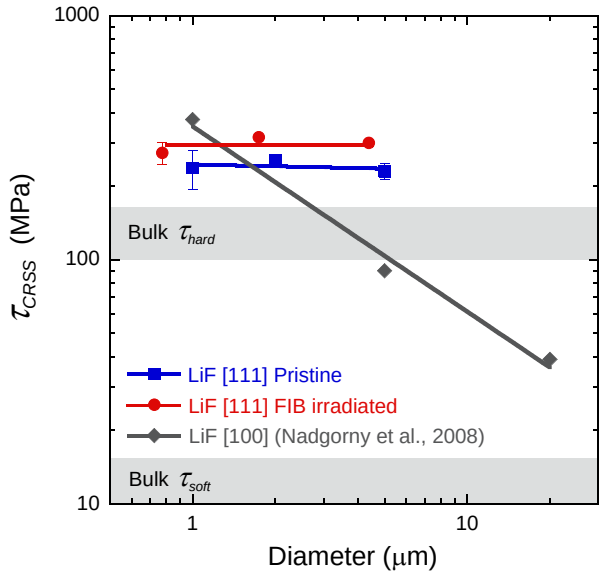

Figure 4.9: Critical resolved shear stress in LiF [111] obtained in this work and in LiF [100] (Nadgorny et al., 2008) as a function of micropillar diameter.

$$\tau_{CRSS} = kd^{-n} \tag{4.6}$$

where τ_{CRSS} is the critical resolved shear stress, k is a constant, and d is the cross-section diameter of the sample. Figure 4.10 plots normalized critical resolved shear stresses and power-law fits for different groups of materials according to the magnitude of their lattice resistance to dislocation motion. When materials have a very small bulk lattice resistance, like in FCC metals, the mechanical response of the micropillars, due for instance to the truncation of dislocation sources, present size effects in the flow stress with power-law exponent n in the range ∼0.6-0.8 (Dimiduk et al., 2005; Frick et al., 2008a; Greer and Nix, 2006; Uchic et al., 2004; Volkert and Lilleodden, 2006) (Figure 4.10 (a)). In the case

of BCC metals, with a higher bulk lattice resistance, the influence of the size effect on the crystal hardening is less marked and lower size effects have been reported, with n in the range 0.21-0.48 (Schneider et al., 2009a,b; Uchic et al., 2009) (Figure 4.10 (b)). This is supported by recent data on various BCC metals suggesting that n was directly linked to the screw dislocation mobility (hence the Peierls potential) at the test temperature (Schneider et al., 2009a,b). Finally, strong solids with very high bulk lattice resistance, like GaAs (Michler et al., 2007) and Si (Moser et al., 2007), show virtually no size effect on the flow stress, with n $\sim$0.1 (Figure 4.10 (c)). This dependency in size effects in the flow stress with the lattice resistance is also observed in materials that show different lattice resistance as a function of their crystal orientation, like MgO (Korte and Clegg, 2011) and LiF (Nadgorny et al., 2008; this work), that show an increase in size effects when the crystal is oriented in the "soft" [100]-orientation (Figure 4.10 (d)). In Figure 4.10 (d) the different groups of materials shown in Figure 4.10 (a)-(c) are represented by envelopes including the respective datasets. It appears therefore that the compressive flow stress of micropillars in materials with high bulk lattice resistance is governed by the bulk yield stress, while size effects associated with the operation of dislocation sources, if any, are of smaller magnitude than the bulk yield stress, and thus irrelevant. One benefit of the lack of size effects is the ability to use micro- and nano-mechanical testing to study the bulk plastic deformation of brittle strong solids without the need of using complex tests, like compression under confining pressure, to avoid cracking.

In view of this, the differences in flow stress between the as-grown and ion-irradiated LiF [111]-oriented pillars (around 30%) can be attributed to the increase in bulk yield stress due to ion irradiation. Although the exact origin and extent of the FIB-induced defects in LiF is unknown, a plausible explanation is the generation of randomly distributed halogen interstitials (the so-called H- and V-centers) that increase the lattice resistance, and that this damage extends deeper in the material than encountered for metallic pillars, contributing to an increase of the bulk yield stress, independently of the diameter of the pillar.

4.5 Conclusions

Compression tests were carried out in LiF single-crystals micropillars oriented in the [111]-direction obtained by etching the matrix away in directionally-solidified eutectic crystals. Micropillars with diameters in the range 1-5 μm, in the as-grown condition or after ion-irradiation by FIB were tested. Ion-irradiation led to an increase of approximately 30% on yield strength and the maximum compressive strength. No effect of the micropillar diameter on flow stress was found in either the as-grown or the ion-irradiated pillars, in contrast to previous studies in LiF micropillars oriented in the [100]-direction and manufactured by FIB which showed a strong size effect on the flow stress (Nadgorny et al., 2008). The discrepancy between both investigations was explained based on the different behavior of the "soft" and "hard" slip systems of LiF, with the "soft" slip systems showing a strong size effect on the flow stress —similar to those found in FCC metals— while the "hard" slip systems did not show any significant size effect. These results are in agreement with previous studies (Korte and Clegg, 2011) pointing out that the extent of the size effect on the flow stress scales with the bulk lattice resistance of the material: i.e. materials with a significant lattice resistance —like bcc metals, Si, GaAs and LiF deformed along the "hard" slip systems— show much less pronounced size effects than materials where the lattice resistance is very small —like FCC metals and LiF deformed along the "soft" slip systems.

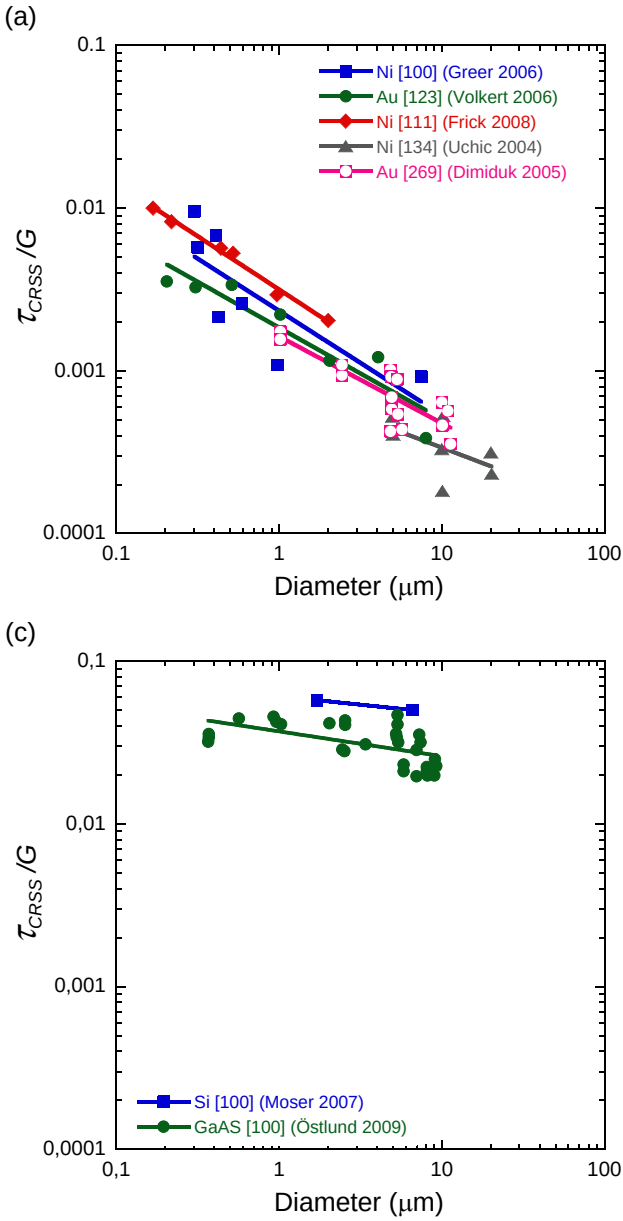

Figure 4.10: Normalised critical resolved shear stresses and power-law fits shown for different groups of materials according to the magnitude of their lattice resistance. (a) FCC metals (low lattice resistance). (b) BCC metals (intermediate lattice resistance).

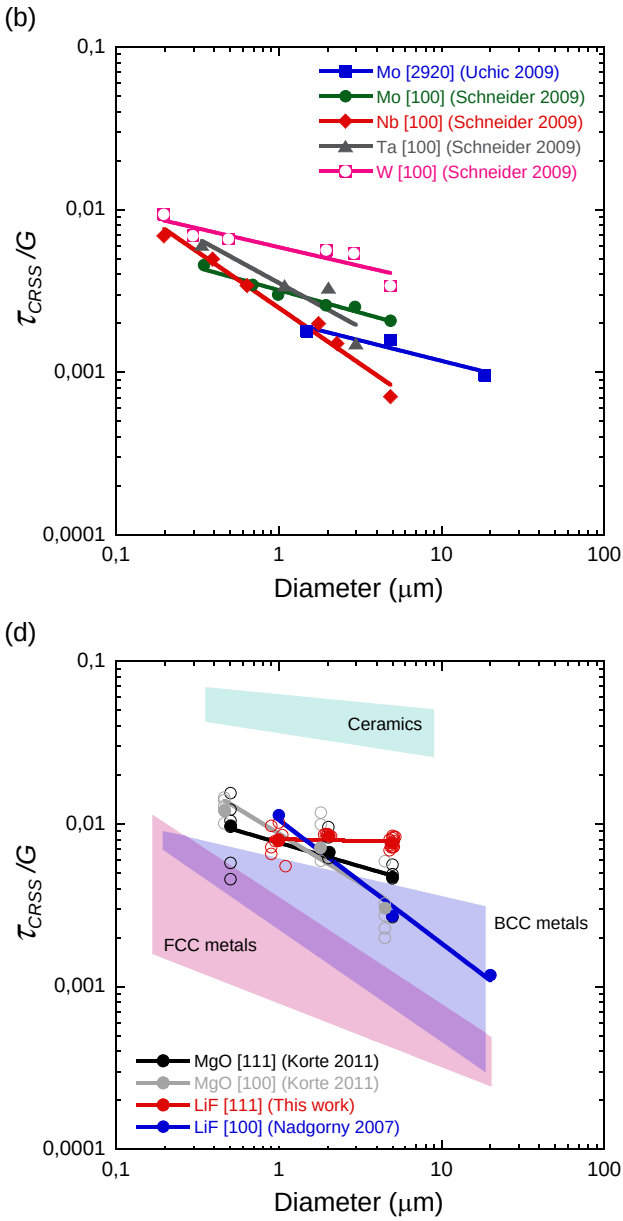

(c) Ceramics (high lattice resistance). (d) LiF and MgO ([100]- and [111]-oriented, low and high lattice resistance, respectively). The different groups of materials shown in (a)-(c) are represented by envelopes including the respective datasets.

5

Temperature-dependent Size Effects in LiF: a New Insight into the Lattice Resistance Contribution

5.1 Introduction

This chapter analyzes for the first time the role of temperature on the size effects observed in the strength of micrometer size single-crystals. In particular, the compression of LiF single-crystal micropillars oriented in the [111]-direction with diameters in the range 1-5 μm is studied in the temperature range between 25

°C and 250 °C. We show that the measured flow stress at 25 °C is in agreement with our previous ex situ study at room temperature, where no significant size effect were observed, but that the rate at which the micropillar strength decreases with temperature depends on the specimen size, the smaller being the stronger. The experimental data obtained at different temperatures is analyze along with the equivalent LiF [111] bulk flow stress. To extend the available bulk flow stress data to the temperature range studied, a model for the dependency of the shear flow stress with temperature is applied. At the lowest temperatures, where micropillars do not show any significant size effect, the predicted bulk flow stress agrees well with the obtained micropillar strengths. However, when temperature is increased, the bulk resistance drops dramatically and at the same time size effects start to appear. This cause-effect relationship is compared with the theoretical critical resolved shear stress (CRSS) required to activate single arm dislocation sources, showing experimentally, for the first time and in the same material, the validity of the model for estimating the role of the lattice resistance on the size effect exponent of small single-crystals.

5.2 In-situ Testing at Elevated Temperatures and Associated Concerns

There are additional considerations for performing accurate in situ micropillar compression experiments at elevated temperatures. For example, a stabilized system, where any environmental changes are already minimized, is required if one is interested in performing accurate mechanical tests. This becomes significantly relevant at the micro-scale, where ambient fluctuations, i.e. heat flow, can induced force and displacement changes on the same order of magnitude than the values to be measured at the specimen. Thermal stabilization of a system at ambient temperature is a good practice in mechanical testing. Usually, the system is held inside an environmentally dedicated enclosure where instrumentation is thermally/acoustically isolated. A high level of thermal stability can typically be achieved through conduction and, in atmosphere, convection, after few hours due to the very small temperature gradients present throughout the

system. However, stabilization of a system at elevated temperatures becomes much more complex. Usually, load and displacement sensors are designed to operate at room temperature —though they can operate adequately within a small range of temperatures—. Thus, in order to obtain accurate measurements at elevated temperatures, heat needs to be confined within the region of interest and kept away form the sensors and any other temperature sensitive components, i.e. positioning stage. Naturally, thermal isolation is not ideal and sensors' temperature slightly increase when increasing the temperature inside the confined region. For example, for the highest tested temperature, 250 °C, the load cell and displacement actuator temperatures increased up to approximately 50 °C and 35 °C, respectively. These temperatures are still within the operation range of the load and displacement sensors, but both load and displacement sensor drifts significantly increased in both magnitude and stabilization time. Moreover, in situ testing inside the SEM adds an extra degree of complexity to the system stability. Vacuum pumping results in cooling of some components, i.e. internal components of the load cell, being affected by the pressure change-induced temperature drop as the interior of the small confined volume is evacuated, according to the ideal gas law. Nevertheless, load and displacement thermal drifts associated with the change in temperature during pumping to vacuum are low compared with thermal drifts induce during heating, and thus are not the limiting factor to obtain a stabilized system at elevated temperatures. We found reasonably high thermal stabilities in all cases after 75 minutes. As expected, the highest tested temperature took the longest time to stabilize, indicating that the higher the imposed thermal gradient the longer the stabilization period.

Another major concern in micro-compression experiments at elevated temperatures is the temperature mismatch between the flat punch tip and the sample. Even if the system has been adequately stabilized, and the sample and the tip temperatures and thermal gradients are highly stable, a temperature mismatch between the sample surface and the tip will result in a thermal drift that only manifests during contact. The magnitude and direction of this drift depends on the direction and magnitude of the heat flow. For example, let us suppose the flat punch tip is colder than the sample. When contact is established, heat will flow from the sample to the tip, resulting in a thermal expansion of the tip

and a thermal contraction of the sample. In load control, as the micropillar is generally much smaller than the tip, the thermal expansion/contraction of both bodies will result in a positive displacement of the tip, at constant load.

In order to close match temperatures between the sample and the tip prior testing, a method proposed by Wheeler et al. (2012) was employed. By this method, a thermally-calibrated tip is used as a temperature probe. The variation in indenter temperature is used as an indicator of the temperature difference between the sample and tip. When a temperature mismatch exits, tip temperature shifts as a function of contact time, indicating whether the sample is hotter or colder than the tip. Then, the tip temperature set-point is adjusted according to the observed shift. This process usually involves varying the tip temperature prior to contact between 3 or 4 times till tip/sample temperatures are matched. Figure 5.1 shows the temperature matching process accomplished for a sample surface temperature of 130 °C.

5.3 Temperature-dependent Size Effects in LiF [111]-oriented Single-crystal Micropillars

5.3.1 Elevated Temperature Micropillar Compression Tests

The in situ, elevated temperature experimental campaign described here has followed best practices introduced in Chapter 3 and Chapter 4 for compressing LiF [111]-oriented single-crystals micropillars. The challenges of compressing highly anisotropic single-crystals micropillars were addressed numerically in Chapter 3. CPFE simulations showed the strong variability in mechanical response this kind of materials may have under some likely experimental uncertainties, namely: geometrical tilt, lattice rotation, or contact misalignment between the flat punch and the top of the pillar. According to the insights given by the numerical analysis, an experimental campaign carried out at room temperature, described in Chapter 4, successfully demonstrated that after correcting, or at least minimizing, these experimental uncertainties, the initial experimental scatter was

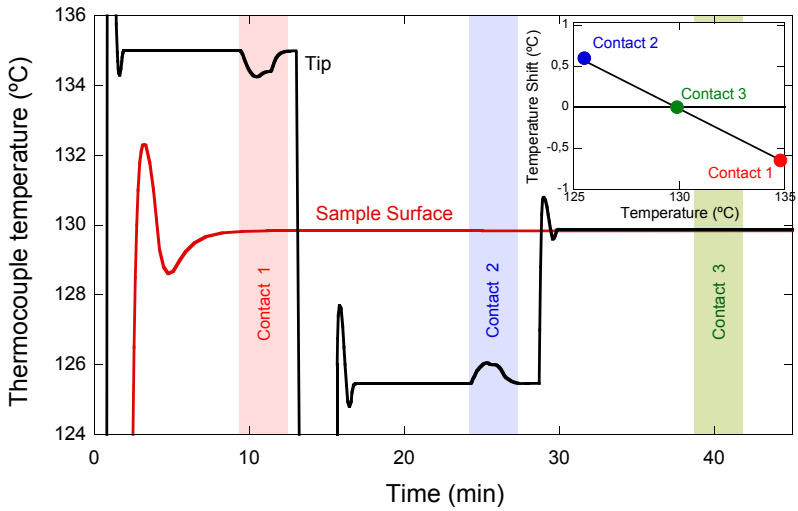

Figure 5.1: An exemplar temperature matching procedure using indenter temperature shift magnitudes to infer the isothermal contact temperature, which coincides with surface thermocouple measurements.

significantly reduced.

The experimental process implemented here follows these good experimental practices. The micropillar selection process becomes much easier when compressing in situ inside the SEM, greatly decreasing specimen uncertainties and increasing testing efficiency. Nevertheless, occasionally some pillars developed marked unsymmetrical deformation states, independently of the strain level attained. Those micropillars were not considered for the analysis. According to CPFE simulations shown in Chapter 3, this non uniform deformation response is indicative of plastic slip on at least one of the "soft" slip systems, and should develop two undesired effects: strain gradients and a dramatic drop in the overall slip resistance of the material. Therefore, only micropillars that remained straight while undergoing plastic deformation were considered for the remaining of this investigation.

Compression tests were carried out inside a Zeiss DSM 962 SEM with an Alemnis In Situ Indenter, first developed by Rabe et al. (2004), which has been modified for operation at elevated temperature, as described elsewhere (Wheeler et al., 2013). The system is inherently displacement-controlled and allows temperature control of both the indenter tip and the sample on independent thermocouple-controlled feedback loops. Compression tests were performed at temperatures of 25 °C, 75 °C, 130 °C, and 250 °C at a constant strain rate, $(\triangle u/\triangle t)/L$, of 10^{-3} s^{-1}, unless indicated otherwise. All the test temperature values reported in this work are the sample surface temperatures as measured by using the thermally-calibrated indenter as a temperature probe, using a technique described previously (Wheeler et al., 2012). The surface temperature measurement precision is typically expected to be on the order of one degree Kelvin. A diamond flat punch tip was used for the experiments. AlN glue was used to mount the samples. This cement is suitable for elevated temperature testing, though it typically requires an elevated temperature cure prior usage. The curing was performed in atmospheric conditions in situ on the sample heater. Micropillars of 5 μm , 2.5 μm , and 1 μm in diameter were tested. The micropillar fabrication technique employed to obtain the samples was previously introduced in Section 2.3.1. Micropillars tested at elevated temperature were obtained from the same set of euctectic samples used to obtain the micropillar tested ex situ at room temperature in Chapter 4. Thus, specimens are quantitatively equivalent to those analyzed previously at room temperature, including their initial dislocation density, found to be of the order of $2.5{\cdot}10^{13}$ m^{-2}.

5.3.2 Stress-strain Response as a Function of Size and Temperature

Under the above mentioned experimental conditions, micro-compression tests were performed on micropillars of 5 μm, 2.5 μm, and 1 μm in diameters in the temperature range between 25 °C and 250 °C, as shown in Figure 5.2 (a)-(c), respectively. Multiple specimens were tested for each micropillar size. A very good reproducibility in the mechanical response was found for all micropillar diameters with a noticeable increase of the scatter for the 1 μm pillar diameter. This

is in agreement with previous results at room temperature and other micropillar compression experiments, as reported elsewhere (Ng and Ngan, 2008a,b,c; Ngan and Ng, 2010), where a larger scatter, together with a more jerky behavior, is found in the smallest pillars, due to the reduction in the available dislocation sources. Additionally, load resolution of the experimental setup used became an issue for the smallest micropillars, as the load required to deform a 1 μm diameter LiF micropillar at high temperature approached the 15 μN load cell noise floor. In fact, this limitation made unfeasible to perform tests at temperatures above 250 °C for the 1 μm diameter micropillars.

To compute stress and strain micropillars' nominal diameter, A_0, and gauge length, L_0, were measured in situ. Due to the as-grown nature of the micropillars slight variations on the diameter (<10%) were found. According to the stress-strain computation shown in Section 4.2.2, the measured load-displacement curves were corrected for the extra compliance associated with the elastic deflection of the matrix at the base of the pillar. To compute this correction a standard shear lag model for load transfer between the matrix and the fiber in an isolated fiber embedded in an infinite matrix was applied (Cox, 1952). Indenter stiffness variation with temperature was not considered. For diamond, Young's modulus change is only a few percent over 500 °C (Aguado and Baonza, 2006). Moreover, LiF modulus is approximately one order of magnitude smaller than that of diamond. Note the system is designed to confine heat within the sample and tip. Thus, no large changes in temperature, and consequently in stiffness, are expected at any other part of the system. Obtained Young's modulus, extracted from the unloading segment of the corrected stress-strain curves, showed a very good agreement with direct elastic modulus measurements carried out at elevated temperatures, as shown elsewhere (Hart, 1977). These results confirm that the system successfully confines heat within the tip and sample, and that tip stiffness variation with temperature is negligible compare with the sample stiffness variation.

Regarding the stress-strain response, the initial elastic loading segment was found to be systematically more compliant than the final unloading segment, regardless of pillar size or testing temperature. As shown in detail in Chapter 3, these discrepancies in stiffness can be explained due to a contact misalignment

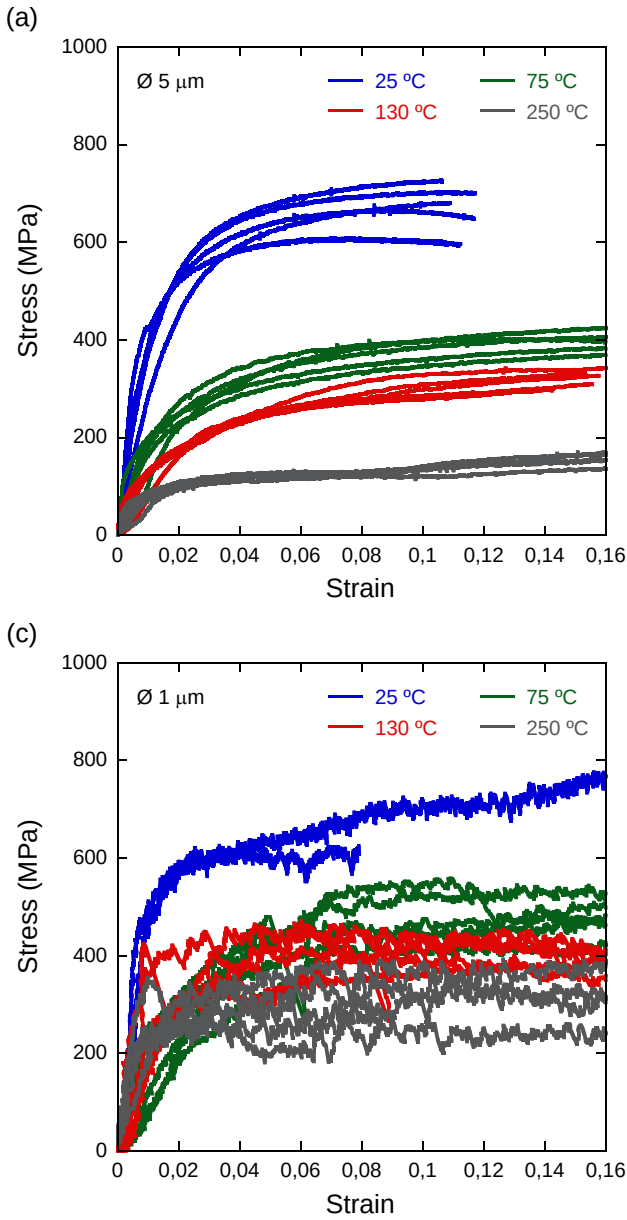

Figure 5.2: Compressive stress-strain curves of micropillars of (a) 5 μm, (b) 2.5 μm, and (c) 1 μm in diameter, respectively, for temperatures of 25 °C (blue lines), 75 °C (green lines), 130 °C (red lines), and 250 °C (grey lines). (d) Flow stress at 10% strain,

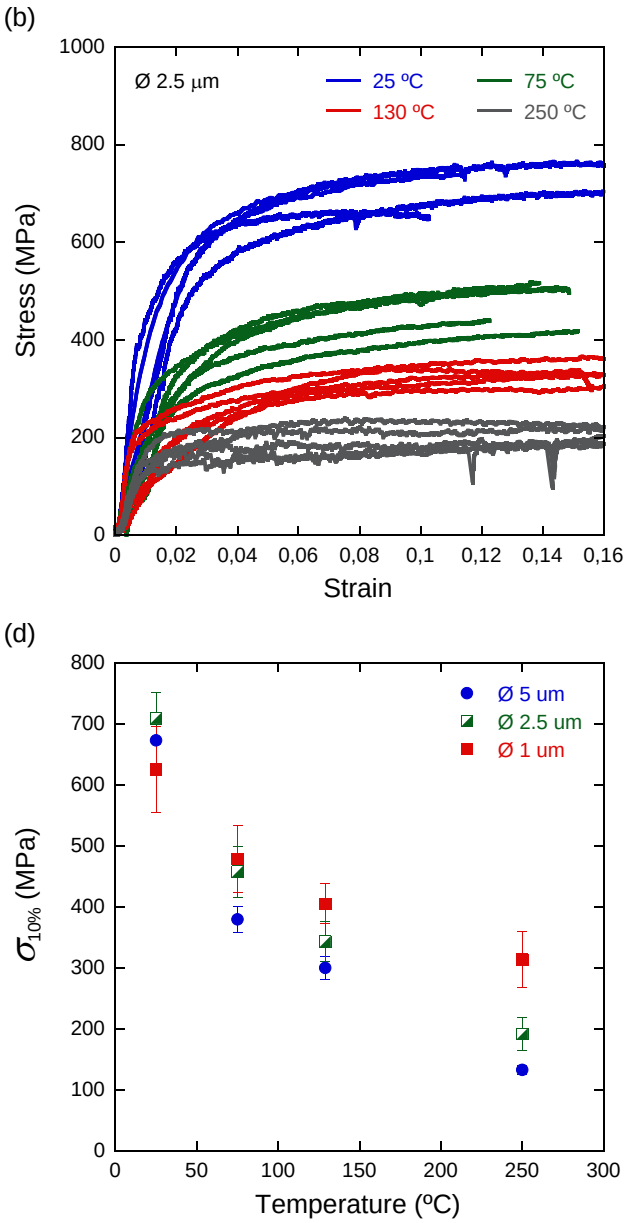

$\sigma_{10\%}$, as a function of temperature for 5 μm (blue dots), 2.5 μm (green dots), and 1 μm (red dots) micropillar diameters.

between the top surface of the pillar and the indenter flat punch tip; stress singularities take place at the contact between the top surface of the pillar and the flat punch tip, leading to an early plastification of the pillar head and the apparent reduction of the initial loading stiffness. This fact made difficult to establish the onset of plastic yield from the stress-strain curves. To avoid uncertainties in the yield stress determination, the flow stress at 10% strain, $\sigma_{10\%}$, has been used throughout this investigation as the reference value to compare the micropillars compressive strength as a function of temperature and micropillar diameter.

Figure 5.2 (d) shows the flow stress at 10% strain, $\sigma_{10\%}$, as a function of temperature for micropillars of 5 μm, 2.5 μm, and 1 μm in diameters. The measured flow stress dependency with sample size at 25 °C is in agreement with our previous ex situ study at room temperature, where no significant size effects were observed. Interestingly, the three sample sizes show a expected reduction of flow stress with temperature, but the rate at which the micropillar strength decreased with temperature depended on the specimen size, the smaller being the stronger. This effect of size is more easily recognized at the highest tested temperature, where 1 μm diameter micropillars are approximately 2.5 times stronger than 5 μm diameter micropillars.

The magnitude of the critical resolved shear stress, τ_{CRSS}, at 10% strain (obtained from the flow stress and the Schimd factor) is plotted in Figure 5.3 as a function of micropillar diameter for different temperatures in the range 25 °C to 250 °C. The plot shows the emergence of a size effect with temperature and the power-law exponent increases from $n \approx 0$ at 25 °C, to $n \approx 0.53$ at 250 °C, and the size effect at 250 °C becomes similar to that displayed by most FCC metals, and also LiF oriented in the $\langle 100 \rangle$ direction, at room temperature. These results demonstrate that the effect of size on the flow stress of LiF [111]-oriented micropillars is strongly dependent on temperature.

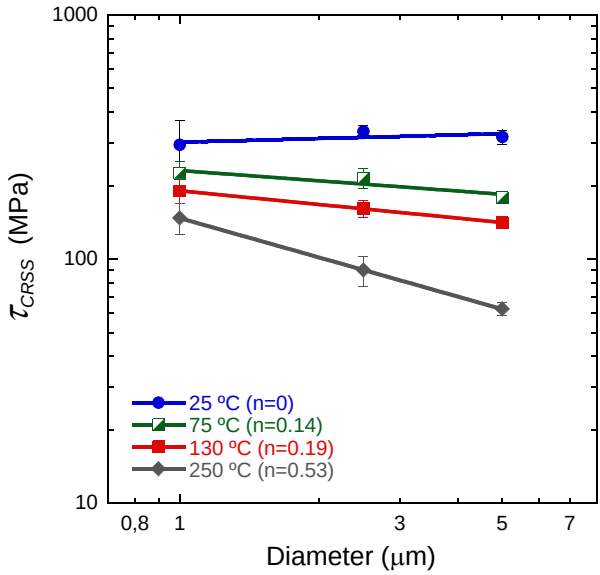

Figure 5.3: Critical resolved shear stress, τ_{CRSS}, as a function of the micropillar diameter in the temperature range between 25 °C to 250 °C . The power law exponent n at each temperature obtained by fitting the experimental results to equation (1) is indicated in the plot.

5.4 Bulk Strength Dependency with Temperature of LiF [111]-oriented

In order to elucidate whether the observed increase in the size effect was associated to the drop in the bulk lattice resistance of the material, as can be extracted from the conclusions driven in Chapter 4, it is necessary to obtain the equivalent LiF [111] bulk flow stress dependency with temperature and analyze it along with the micropillar experimental data obtained at different temperatures. Unfortunately, there is scarce data in the literature on the LiF bulk flow stress dependency with temperature. Gilman (1959b) performed LiF (100) glide torsion tests on macroscopic specimens for testing temperatures ranging from 600

to 900 K (see Figure 2.1). The brittle nature of the LiF when deformed along the hard slip systems made unfeasible to test specimens below 600 K without cracking.

To extend the available bulk flow stress data to lower temperatures a model for the dependency of the shear flow stress with temperature was applied. As derived elsewhere (Bhakhri et al., 2012; Clegg et al., 2006; Pitchford, 1999), a simple model can be developed to express the resolved shear flow stress as a function of both strain rate and temperature. Starting from the well established Orowan equation:

$$\dot{\gamma} = \rho_m \cdot b \cdot \mathrm{v} \tag{5.1}$$

which relates the shear strain rate $\dot{\gamma}$, with the mobile dislocation density ρ_m, the Burgers' vector b, and the average dislocation velocity v. The dislocation velocity v can be defined using a standard approach for a stress activated process:

$$\mathrm{v} = v \cdot b \cdot \left[exp\left(-\frac{(\tau_p - \tau)V}{kT} \right) - exp\left(-\frac{(\tau_p + \tau)V}{kT} \right) \right] \tag{5.2}$$

where v is the attempt frequency, τ_p is the lattice resistance at 0 K, or Peierls' stress, and τ is the resolved shear flow stress. V is the activation volume, and it is assumed to be constant. k is the Boltzsmann's constant, and T the absolute temperature. Combining both equations and solving for τ yields the following relationship:

$$\tau = \frac{kT}{V} sinh^{-1} \left[\frac{\dot{\gamma}}{2 \cdot \rho_m \cdot v \cdot b^2} exp\left(\frac{\tau_p V}{kT} \right) \right] \tag{5.3}$$

Considering τ=τ_0, the intrinsic bulk lattice resistance to dislocation glide, the bulk flow stress τ_{bulk} can be expressed as the additive contribution of τ_0 and the forest dislocations, such that:

$$\tau_{bulk} = \frac{kT}{V} sinh^{-1}\left[\frac{\dot{\gamma}}{2\cdot \rho_m \cdot v \cdot b^2} exp\left(\frac{\tau_p V}{kT}\right)\right] + 0.5\mu b\sqrt{\rho_{tot}} \qquad (5.4)$$

where μ is shear modulus and ρ_{tot} the total dislocation density. The contribution of forest dislocations should be virtually athermal, and as τ_0 size independent, as will be discussed later.

This relationship forms the basis for extending the available bulk flow stress data for LiF [111] single crystals to lower temperatures, with the aid of the room temperature micropillar compression results. Taking advantage of the fact that the flow stress at room temperature is not affected by size effects, i.e. τ_{CRSS}=τ_{bulk}, as shown in Figure 5.3, micropillars were tested at different strain rates in the range 0.00033 to 0.033 s^{-1} at room temperature. Assuming that the activation volume is independent of the strain rate, and that τV remains large with respect to kT, equation 5.4 can be simplified to:

$$\tau_{bulk} = \tau_p + \frac{kT}{V} ln[\dot{\gamma}] - \frac{kT}{V} ln[\rho_m \cdot v \cdot b^2] + 0.5\mu b\sqrt{\rho_{tot}} \qquad (5.5)$$

i.e., the bulk shear stress τ_{bulk} varies linearly with the natural logarithm of shear strain rate. Figure 5.4 shows this is indeed the case and validates the Peierls' model to analyze the strain rate sensitivity of LiF [111] micropillars at room temperature. From the linear slope $\frac{kT}{V}$, it is possible to determine the activation volume V, giving a value of $2.6{\cdot}10^{-28}$ m^3 or 11.41 b^3.

Moreover, the room temperature microcompression data provides the basis for extending the available bulk flow stress data for LiF [111] single-crystals to lower temperatures, with the aid of equation 5.5. Figure 5.5 plots the experimental critical resolved shear stress on the $\{100\}\langle 110\rangle$ hard slip systems of LiF coming from microcompression in this work together with the available bulk shear strengths in literature (Gilman, 1959b; Gilman and Johnston, 1956) from testing single-crystals at high temperature. Both sets of results could be fit by equation 5.5 using the Peierls' stress = 530 MPa as the only adjustable parameter and the corresponding curves are shown as solid lines in Figure 5.5. The

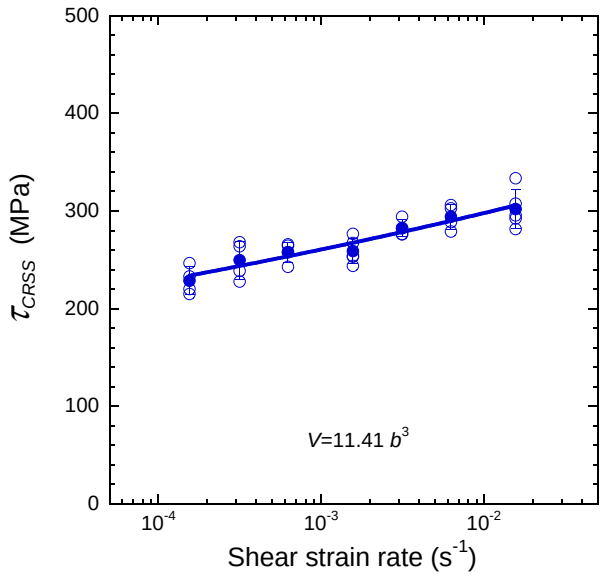

Figure 5.4: Influence of strain rate on the critical resolver shear stress of [111] LiF micropillar single-crystals at ambient temperature. The activation volume V was determined from the linear slope between τ_{CRSS} and the natural logarithm of the shear strain rate.

actual materials and testing parameters used in equation 5.5 are summarized in Table 5.1, where the attempt frequency v was calculated from Debye's frequency equation and the Burgers' vector b was considered constant —its variation with temperature is so small, $\sim 10^{-6}$ K^{-1}, that can be neglected for the range of temperatures studied—. The shear strain rate and the total dislocation density for each data set are reported and the mobile dislocation density was considered 3/12 of the total dislocation density assuming slip along the three "hard" slip systems preferentially oriented for slip (see Section 2.2). The thermal dependency of the shear modulus μ was obtained from Hart (1977).

It should be noted that equation 5.5 captured successfully the influence of temperature on the critical resolved shear stress of micropillars at ambient temperature (blue curve) and bulk crystals (grey curve) at high temperatures. How-

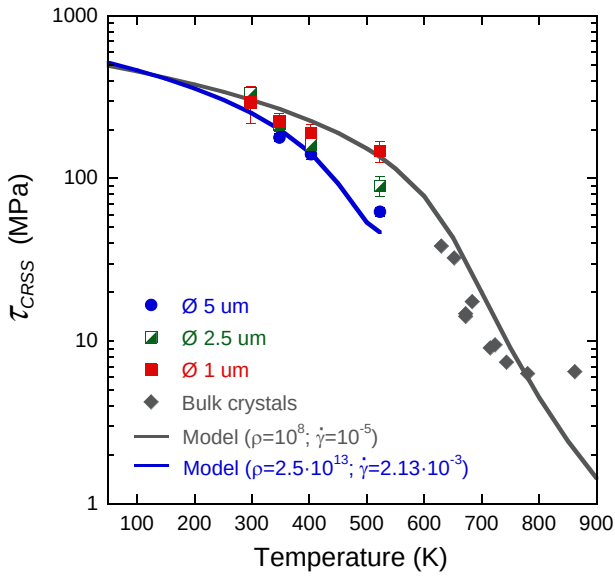

Figure 5.5: Theoretical prediction of the bulk strength τ_{bulk} of the hard $\{100\}\langle 110\rangle$ slip system in LiF as a function of temperature for two different dislocation densities and imposed shear strain rates, as summarized in Table 5.1, following equation 5.5. The dots represent the experimental data for micropillars of different diameter (1 μm in red, 2.5 μm in green, and 5 μm in blue) and bulk LiF (grey dots) from Gilman and Johnston (1956).

Table 5.1: LiF parameters used to define the bulk shear flow stress dependency with temperature, according to equation 5.5.

Testing conditions		
	$\dot{\gamma}$	ρ_{tot} (m^{-2})
Bulk (Gilman and Johnston, 1956)	10^{-5}	10^{8}
This work	$2.13 \cdot 10^{-3}$	$2.5 \cdot 10^{13}$

Material constants			
v (sec^{-1})	b (nm)	V (b^3)	τ_p (MPa)
$8 \cdot 10^{11}$	0.285	11.41	530

ever, it failed to capture the behavior of micropillars at high temperature, where significant size effects are observed. These results reinforce the hypothesis that the observed increase in size effects with temperature is directly linked to the drop in the bulk lattice resistance of the material.

5.5 Discussion

As seen in Chapter 1, for most experimental studies obtained by compressing single-crystal micropillars with diameters in the range between 1 to 10 μm at room temperature, the strength at a given plastic strain between 1 and 10% follows a power-law dependency with diameter D of the form:

$$\sigma = AD^{-n} \tag{5.6}$$

where A is constant, and n is the power-law exponent. It is now widely accepted that for micropillars with a diameter of a few micrometers that are not dislocation free (i.e., which behavior is not controlled by dislocation nucleation and/or

dislocation starvation processes), this power-law dependency arises from the operation of single arm dislocation sources (Rao et al., 2008; Tang et al., 2008), with the power-law exponent ranging from 0.61 to 0.97 (Uchic et al., 2009) for FCC metals, 0.21 to 0.48 (Schneider et al., 2009a) for BCC metals, or ≈0 for strong solids, like GaAs (Michler et al., 2007) and Si (Moser et al., 2007). Moreover, in Chapter 4 we have shown how in solids exhibiting different slip systems depending on crystallographic loading axis, like MgO (Korte and Clegg, 2011) and/or LiF (this work), different power-law exponents have been found depending on the bulk critical resolved shear stress of the operating slip system, with soft slip systems showing larger power-law exponents, while the hard slip systems show a reduced or negligible size effect. Thus, the power-law exponent n is material-dependent, and this dependency has been associated with the magnitude of the lattice resistance (Kim et al., 2009; Korte and Clegg, 2011; Lee and Nix, 2012; this work), the dislocation density (Lee and Nix, 2012), and/or the critical temperature (Schneider et al., 2009b, 2013).

Besides our study on the size effect dependency with the magnitude of the lattice resistance, the dependency of size effects with material properties has been the subject of few other studies (Korte and Clegg, 2011; Lee and Nix, 2012), by comparing the bulk strength of a range of materials with the theoretical stress required to activate single arm dislocation sources. The operation stress of single arm dislocation sources is typically calculated by summing the lattice resistance to dislocation glide, the contribution of forest dislocations, and the line tension stress, as suggested in various papers (Ng and Ngan, 2008a; Norfleet et al., 2008; Parthasarathy et al., 2007). Following Parthasarathy et al. (2007), the critical resolved shear stress τ_{CRSS} for the activation of a single arm dislocation source is given by:

$$\tau_{CRSS} = \tau_0 + 0.5\mu b\sqrt{\rho_{tot}} + \frac{\alpha\mu b}{\bar{\lambda}_{max}(D, \rho_{tot}, \beta)} \tag{5.7}$$

where τ_0 is the lattice resistance to dislocation glide, μ is the anisotropic shear modulus, b is the magnitude of Burgers' vector, ρ_{tot} is the total dislocation density, α is a constant of the order of unity, and $\bar{\lambda}_{max}$ is the statistical average

length of the weakest single arm dislocation source, which is a function of the micropillar diameter D, the dislocation density ρ_{tot} and the slip plane orientation β. The first two terms in equation 5.7 contribute to the bulk strength of the material τ_{bulk} and are size independent, as seen in previous section, but the third term, τ_{size}, gives rise to the size effect, since the average length of the weakest single arm dislocation source scales with the micropillar diameter, as described statistically by Parthasarathy et al. (2007). As pointed out by Korte and Clegg (2011), it is clear from equation 5.7 that in materials with a negligible bulk strength, like FCC metals, the size dependent term amounts for the majority of the strength of the micropillar, while in materials with non-negligible bulk strength, like BCC metals and ceramics, the extent of the size effect would depend on the relative magnitude of the size independent and size dependent terms of equation 5.7. From comparison of equation 5.6, typically used to analyze micropillar compression strengths, and 5.7, it is then expected that in materials with high bulk strength, the contribution of the bulk strength to the operation stress of single arm dislocation sources will be important, giving rise to small or negligible power-law exponents. However, Korte and Clegg (2011) concluded that quantitative comparison between the different terms in equation 5.7 was difficult. This was due to the impossibility of estimating the lattice resistance and the forest hardening contribution in equation 5.7 in those materials for which micropillar compression data was available, as there were many uncertainties in the dislocation densities and/or the strain rate of the tests.

A similar approach has been proposed by Lee and Nix (2012), to carry out a thorough study of the effect of lattice resistance τ_0, the shear modulus μ and the magnitude of the Burgers' vector b on the extent of the size effect, proposing a universal scaling law that worked very well for the majority of FCC and BCC metals, for typical dislocation densities of the order of 10^{12} m^{-2}:

$$\frac{\tau_{CRSS} - \tau_{bulk}}{\mu b} = AD^{-n} \tag{5.8}$$

Based on equation 5.7, Lee and Nix (2012) has also proposed that size effects in strong solids should depend on temperature. As temperature increases, the

lattice resistance τ_0 decreases, while the contribution of forest hardening and single-arm dislocation source operation should be essentially athermal. Temperature will also increase the magnitude of Burgers' vector b, due to thermal expansion, and will decrease the shear modulus μ. Since the effect of temperature on the lattice resistance is typically larger than on the shear modulus and the Burgers' vector, their analysis predicted an increase in the power-law exponent with temperature. However, due to the difficulties inherent to nanomechanical testing at high temperatures, their predictions could not be contrasted with experimental data.

We quantitatively compare this trend in the size effect exponent with temperature, with the reduction of the lattice resistance due to thermal activation, analyzing experimentally the validity of equation 5.7 for estimating the role of the lattice resistance on the size effect exponent of small single-crystals. Exact determination of each of the three terms contributing to the critical resolved shear stress in equation 5.7 requires the precise knowledge of the initial dislocation density of the crystal. Contrary to the majority of the studies on size effects, our micropillars were fabricated without the need of focused ion beam (FIB) milling (see Section 2.3.1). As discuss earlier, FIB machining is well known to introduce defects on the machined micropillars, like the formation of Ga^+ implanted amorphous layers (Kiener et al., 2007) and/or defects that result in lattice distortions and dislocation loops (Maas et al., 2008). Therefore, even if the initial dislocation density of the crystal is measured, the defect structure on the final micropillar after FIB milling can be dramatically different, introducing many uncertainties in equation 5.7 (Korte and Clegg, 2011). Thus, the initial dislocation density measured in this study was free of additional artifacts and/or defects introduced by FIB fabrication, which provided a precise estimation of the dislocation density on the micropillars prior to testing.

The predictions of equation 5.7 for the τ_{CRSS} as a function of temperature are plotted in Figure 5.6, together with the experimental data. As shown in previous section, the bulk lattice resistance τ_{bulk} dependency with temperature of our LiF [111]-oriented system was determined following equation 5.5. The mean value of source length, $\bar{\lambda}_{max}$, was calculated according to the statistical model described by Parthasarathy et al. (2007):

$$\begin{aligned}\bar{\lambda}_{max} &= \int_0^R \lambda_{max} n(\lambda_{max}) d\lambda_{max} \\ &= \int_0^R \left[1 - \frac{\pi(R-\lambda_{max})(b-\lambda_{max})}{\pi R b}\right]^{n-1} \\ &\quad \times \left[\frac{\pi[(R-\lambda_{max})+(b-\lambda_{max})]}{\pi R b}\right] n\lambda_{max} d\lambda_{max}\end{aligned} \tag{5.9}$$

where R is the radius of the pillar, b the Burgers' vector, and n the number of pinning points:

$$n = \text{Integer}[\rho_m \pi R h] \tag{5.10}$$

where ρ_m is the mobile dislocation density, and h is the height of the pillar.

The agreement between the experimental results and the predictions of equation 5.7 is remarkable. The bulk strength dominates over the size-dependent contribution at 25 °C and 75 °C in the range of micropillar diameters tested and no size effects are found. However, both contributions are of the same order at 250 °C and a strong size effect develops at high temperature. These results show that lattice resistance influences the power-law exponents for the size effect of different materials, as proposed by Korte and Clegg (2011); Lee and Nix (2012). Recent results in Mo micropillars (Schneider et al., 2013), a BCC metal with a high lattice resistance, have also shown similar trends, with the size exponent increasing at temperatures close to 250 °C, the critical temperature for Mo at which the lattice resistance is expected to become negligible. However, micropillars were machined by focus ion beam milling in that study and the uncertainty in the initial dislocation density precluded any estimation of the size dependent and size independent terms at each temperature. Our results unambiguously demonstrate the role of the lattice resistance on the size effect of micrometer-size single-crystals, showing experimentally, for the first time and in the same material, that the size effect observed during micropillar compression comes about

as a result of the relative weights of the size independent (lattice resistance plus forest hardening) and size dependent contributions to strength.

5.6 Conclusions

The influence of temperature on the compressive strength of [111] LiF single crystals was measured by means of micropillar compression tests. Micropillars of diameters in the range 1 to 5 μm were obtained by means of directional-solidification and surface etching of eutectic compounds, leading to single crystals with a controlled initial dislocation density of $\approx 2.5 \cdot 10^{13}$ m^{-2}. The micropillar flow strength was independent of the micropillar diameter at ambient temperature but a strong size effect developed with temperature and the micropillars of 1 μm in diameter were twice stronger than those with 5 μm in diameter. The different contributions to the flow stress of the micropillars, namely lattice resistance, forest hardening and the size-dependent contribution due to operation of single arm dislocation sources were rigorously accounted for as a function of temperature and micropillar diameter. It was demonstrated that the size effect observed during micropillar compression comes about as a result of the relative weights of the size independent (lattice resistance plus forest hardening) and size dependent contributions to strength. The former dominated at room temperature (and no size effect was found) while both were of the same order at 250 °C for the micropillar diameters studied, leading to a strong size effect. Thus, the role of the lattice resistance on the size effect of micrometer-size single-crystals was demonstrated unambiguously for this first time. This result rationalizes the different values of power-law exponent for the size effect found in the literature for FCC and BCC metals as well as covalent and ionic solids.

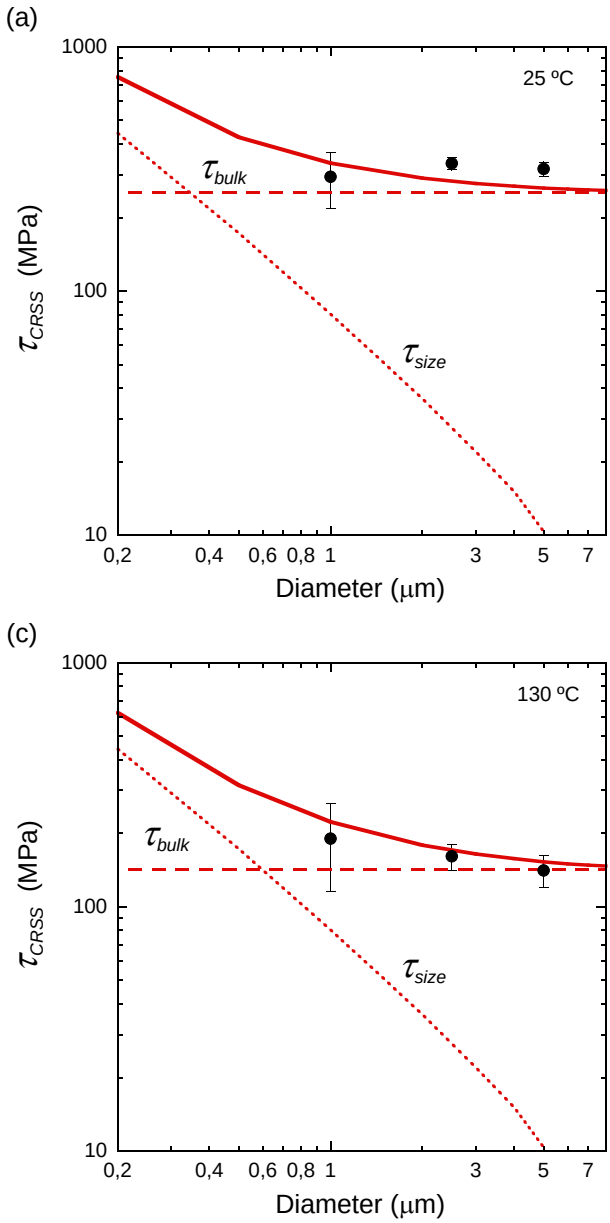

Figure 5.6: Evolution of critical resolved shear stress τ_{CRSS}, according to equation 5.7 and comparison with experimental data. (a) 25 °C; (b) 75 °C; (c) 130 °C and (d) 250 °C. The dashed line represents the size independent contribution at each tempera-

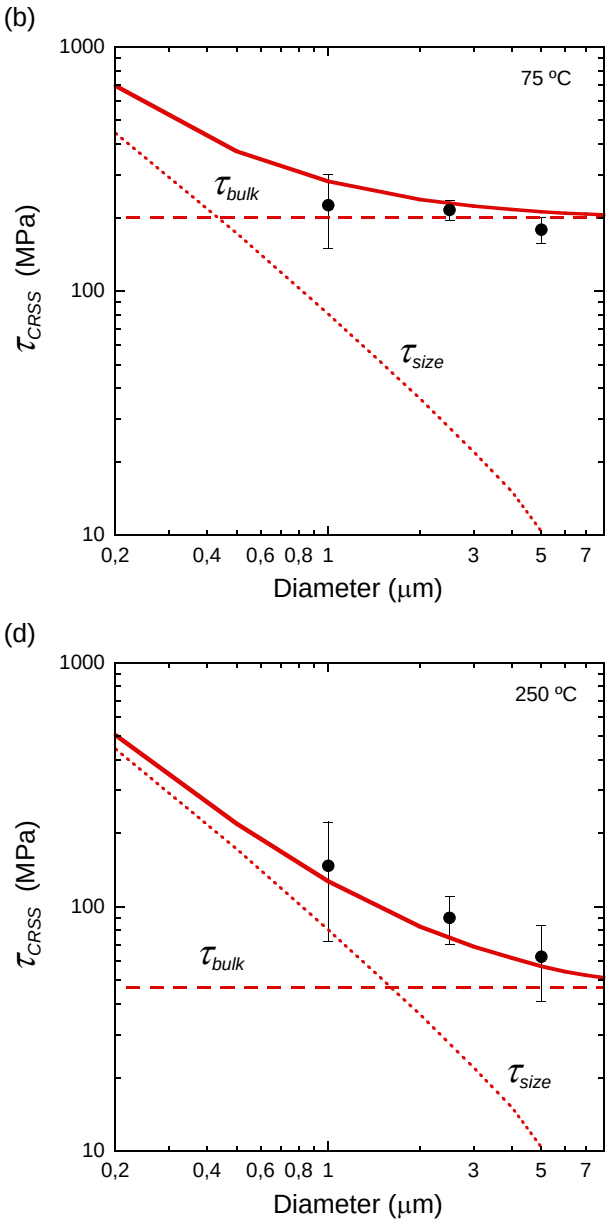

ture (lattice resistance and forest hardening) while the dotted line represents the size dependent contribution due to the operation of single arm dislocation sources.

6
Conclusions

This thesis has been devoted to the study of the size effect in strength of micro-size LiF single-crystalline pillars oriented in the [111]-direction. The following conclusions have been established:

- A novel approach has been proposed to fabricate micro-size single-crystalline pillars for micro-compression testing. In particular, we have shown how to fabricate LiF [111]-oriented single-crystalline micropillars from directionally solidified LiF-NaCl and LiF-KCl eutectics without the need of FIB milling, and thus, without inducing any damage into the specimen, which eventually allows to study the mechanical properties of the material in its as-grown state.

- Plasticity in LiF has been evaluated in terms of crystal orientation and slip systems activation by means of crystal plasticity finite element simulations. Simulations in the [111]-direction confirmed that plasticity occurs in the "hard" $\{100\}\langle 110\rangle$ slip systems. However, simulation of three sources of possible experimental uncertainties —lattice rotation, micropillar tilt,

and contact misalignment— revealed the easy additional activation of the "soft" $\{110\}\langle 110\rangle$ slip systems as a result of the large difference in flow strength between the two sets of slip system. These results highlight the experimental challenges of compressing materials which exhibit a marked plastic anisotropy, and provides a rationale to understand the origin of the experimental scatter initially observed.

- Micro-compression tests carried out on LiF micropillars oriented in the [111]-direction have not shown any significant effect of the micropillar diameter on the flow stress at room temperature. These results contrast with previous studies in the [100]-direction, where plasticity occurs in the "soft" slip systems, that showed a strong size effects on the flow stress (Nadgorny et al., 2008). This discrepancy is in agreement with previous observations that suggest that the extent of the size effect on the flow stress scales with the intrinsic lattice resistance of the material (Korte and Clegg, 2011).

- The influence of focused ion beam (FIB) machining on size effects has been also addressed by further micro-machining of the previously obtained as-grown LiF micropillars. Exposure to FIB revealed that ion-irradiation led to an increase of approximately 30% on yield strength and the maximum compressive strength, but no effect of the micropillar diameter on the flow stress was found either.

- Elevated temperature compression tests carried out in LiF [111]-oriented micropillars in the temperature range between 25 °C and 250 °C demonstrates that the effect of pillar size on the flow stress of LiF [111]-oriented micropillars is strongly dependent on temperature. It was demonstrated that the size effect observed during micropillar compression comes about as a result of the relative weights of the size-independent (lattice resistance plus forest hardening) and size-dependent (operation of single arm dislocation sources) contributions to strength. The former dominated at room temperature (and no size effect was found) while both were of the same order at 250 °C for the micropillar diameters studied, leading to a strong size effect. Thus, the role of the lattice resistance on the size effect of

micrometer-size single-crystals was demonstrated unambiguously for this first time. This result rationalizes the different values of power-law exponent for the size effect found in the literature for FCC and BCC metals as well as covalent and ionic solids.

Bibliography

Inc. ABAQUS. *Users Manual, version 6.7.* ABAQUS, Inc., New York, 2008. 56, 62

F. Aguado and V.G. Baonza. Prediction of bulk modulus at high temperatures from longitudinal phonon frequencies: Application to diamond, c-BN, and 3C-SiC. *Physical Review B*, 73:024111, 2006. 111

S. Akarapu, H.M. Zbib, and D.F. Bahr. Analysis of heterogeneous deformation and dislocation dynamics in single crystal micropillars under compression. *International Journal of Plasticity*, 26:239–257, 2010. 95

A. Argon. *Strengthening Mechanisms in Crystal Plasticity.* Oxford University Press, 2008. 32

E. Arzt. Size effects in materials due to microstructural and dimensional constraints: A comparative review. *Acta Metallurgica*, 46:5611–5626, 1998. xxi, 7, 13

R.J. Asaro. Crystal plasticity. *Journal of Applied Mechanics-Transactions of the Asme*, 50(4b):921–934, 1983. 59

M.F. Ashby. The deformation of plastically non-homogeneous materials. *Philosophical Magazine*, 21 (170):399–424, 1970. 8, 18

B. Backes, K. Durst, and M. Göken. Determination of plastic properties of polycrystalline metallic materials by nanoindentation - experiments and finite element simulations. *Philosophical Magazine A*, 86:5541–5551, 2006. 22

R. Becker. Analysis of texture evolution in channel die compression-I. Effects of grain interaction. *Acta Metallurgica Materialia*, 39:1211–30, 1991. 62

H. Bei, S. Shim, E.P. George, M.K. Miller, E.G. Herbert, and G.M. Pharr. Compressive strengths of molybdenum alloy micropillars prepared using a new technique. *Scripta Materialia*, 57:397–400, 2007. 24, 26, 32

H. Bei, S. Shim, G.M. Pharr, and E.P. George. Effects of pre-strain on the compressive stress-strain response of Mo-alloy single-crystal micropillars. *Acta Materialia*, 56:4762–4770, 2008. 32, 95

V. Bhakhri, J. Wang, N. Ur-rehman, C. Ciurea, F. Giuliani, and L.J. Vandeperre. Instrumented nanoindentation investigation into the mechanical behavior of ceramics at moderately elevated temperatures. *Journal of Materials Research*, 27:65–75, 2012. 116

S.S. Brenner. Tensile strength of whiskers. *Journal of Applied Physics*, 27:1484–91, 1956. 14

S.S. Brenner. Plastic deformation of copper and silver whiskers. *Journal of Applied Physics*, 28:1023–26, 1957. 14

L.M. Brown and R.K. Ham. *Strengthening Methods in Crystals*. Elsiever, Amsterdam, 1971. 7

C.M. Byer, B. Li, B. Cao, and K.T. Ramesh. Microcompression of single-crystal magnesium. *Scripta Materialia*, 62:536–9, 2010. 34

Y.-T. Cheng and C.-M. Cheng. Scaling, dimensional analysis, and indentation measurements. *Materials Science and Engineering Reports: A Review Journal*, 44:91, 2004. 50

K-H. Chia, K. Jung, and H. Conrad. Dislocation density model for the effect of grain size on the flow stress of a Ti-15.2 at.% Mo β-alloy at 4.2-650 K. *Materials Science and Engineering: A*, 409:32–38, 2005. 8

Y.S. Choi, M.D. Uchic, T.A. Parthasarathy, and D.M. Dimiduk. Numerical study on microcompression tests of anisotropic single crystals. *Scripta Materialia*, 57:849–852, 2007. 27, 28, 57

A.H. Chokshi, A. Rosen, J. Karch, and H. Gleiter. On the validity of the Hall-Petch relationship in nanocrystalline materials. *Scripta Metallurgica*, 23:1679, 1989. 9

W.J. Clegg, L.J. Vandeperre, and J.E. Pitchford. Energy changes and the lattice resistance. *Science of Engineering Ceramics III*, 317:271–276, 2006. 116

H.L. Cox. The elasticity and strength of paper and other fibrous materials. *British Journal of Applied Physics*, 3:72–79, 1952. 84, 111

D.M. Dimiduk, M.D. Uchic, and T.A. Parthasarathy. Size-affected single-slip behavior of pure nickel microcrystals. *Acta Materialia*, 53:4065–77, 2005. 25, 29, 99

D.M. Dimiduk, E.M. Nadgorny, C. Woodward, M.D. Uchic, and P.A. Shade. An experimental investigation of intermittent flow and strain burst scaling behavior in LiF crystals during microcompression testing. *Philosophical Magazine*, 90:3621–3649, 2010. 94

R. Dou and B. Derby. A universal scaling law for the strength of metal micropillars and nanowires. *Scripta Materialia*, 61:524–7, 2009. 30

D.J. Dunstan and A.J. Bushby. Theory of deformation in small volumes of material. *Proceedings of the Royal Society: A*, 460:2781–2796, 2004. 19, 20

J.A. El-Awady, C. Woodward, D.M. Dimiduk, and N.M. Ghoniem. Effects of focused ion beam induced damage on the plasticity of micropillars. *Physical Review B*, 80:104104, 2009. 95

A.M. El-Sherik, U. Erb, G. Palumbo, and K.T. Aust. Deviations from Hall-Petch behavior in as-prepared nanocrystalline nickel. *Scripta Materialia*, 27: 1185, 1992. 9

D. Farkas, S. Mohanty, and J. Monk. Strain-driven grain boundary motion in nanocrystalline materials. *Materials Science and Engineering: A*, 493:33–40, 2008. 10

A. C. Fischer-Cripps. *Nanoindentation*. Springer, New York, USA, 2002. 50

N.A. Fleck, G.M. Muller, M.F. Ashby, and J.W. Hutchinson. Strain gradient plasticity: Theory and experiment. *Acta Metallurgica et Materialia*, 42:475–487, 1994. xxi, 18, 19

G.E. Fougere, J.R. Weertman, R.W. Siegel, and S. Kim. Grain-size dependent hardening and softening of nanocrystalline Cu and Pd. *Scripta Metallurgica*, 26:1879, 1992. 9

F.C. Frank and J.H. van der Merwe. One-dimensional dislocations. II. Misfitting monolayers and oriented overgrowth. *Proceedings of the Royal Society: A*, 198: 216–225, 1949. 12

C.P. Frick, S. Orso, and E. Arzt. Loss of pseudoelasticity in nickel-titanium submicron compression pillars. *Acta Materialia*, 55:3845–55, 2007. 34

C.P. Frick, B.G. Clark, S. Orso, A.S. Schneider, and E. Arzt. Size effect on strength and strain hardening of small-scale [111] nickel compression pillars. *Materials Science and Engineering: A*, 489:319–29, 2008a. 29, 99

C.P. Frick, B.G. Clark, S. Orso, P. Sonnweber-Ribic, and E. Arzt. Orientation-independent pseudoelasticity in small-scale NiTi compression pillars. *Scripta Materialia*, 59:7–10, 2008b. 34

H. Gao, Y. Huang, and W.D. Nix. Modeling plasticity at the micron scale. *Naturwissenschaften*, 86:507–515, 1999. 22

W.W. Gerberich, W.M. Mook, C.R. Perrey, C.B. Carter, M. Baskes, R. Mukherjee, A. Gidwani, J. Heberlein, P. McMurry, and S. Girshick. Superhard silicon

nanospheres. *Journal of the Mechanics and Physics of Solids*, 51:979–992, 2003. 22

W.W. Gerberich, M.J. Cordill, W.M. Mook, N.R. Moody, C.R. Perrey, C.B. Carter, R. Mukherjee, and S.L. Girshick. A boundary constraint energy balance criterion for small volume deformation. *Acta Materialia*, 53:2215–2219, 2005. 22

V.Y. Gertsman, M. Hoffmann, H. Gleiter, and R. Dirringer. Grain size dependence of yield of copper. *Acta Materialia*, 42:3539, 1994. 9

D.S. Gianola, S. Van Petegem, M. Legros, S. Brandstetter, H. Van Swygenhoven, and K.J. Hemker. Stress-assisted discontinuous grain growth and its effect on the deformation behavior of nanocrystalline aluminum thin films. *Acta Materialia*, 54:2253–63, 2006. 10

D.S. Gianola, C. Eberl, X.M. Cheng, and K.J. Hemker. Stress-driven surface topography evolution in nanocrystalline Al thin films. *Advance Materials*, 20: 303, 2008a. 10

D.S. Gianola, B.G. Mendis, X.M. Cheng, and K.J. Hemker. Grain-size stabilization by impurities and effect on stress-coupled grain growth in nanocrystalline Al thin films. *Materials Science and Engineering: A*, 483:637–40, 2008b. 10

A. Giga, Y. Kimoto, Y. Takigawa, and K. Higashi. Demonstration of an inverse Hall-Petch relationship in electrodeposited nanocrystalline Ni-W alloys through tensile testing. *Scripta Materialia*, 55:143, 2006. 9

J.J. Gilman. Plastic anisotropy of LiF and other rock salt type crystals. *Acta Metallurgica*, 7:608, 1959a. 41, 63, 67, 79, 80, 89, 98

J.J. Gilman. The plastic resistance of crystals. *Australian Journal of Physics*, 13:327, 1959b. xxii, 41, 42, 115, 117

J.J. Gilman and W.G. Johnston. The origin and growth of glide bands in lithium fluoride crystals. *Dislocations and Mechanical Properties of Crystals*, Conference:116–163, 1956. 117, 119, 120

J.J. Gilman, W. G. Johnston, and G. W. Sears. Dislocation etch pit formation in lithium fluoride. *Journal of Applied Physics*, 29(5):747–754, 1958. 82

J. R. Greer and J. Th.M. De Hosson. Plasticity in small-sized metallic systems: Intrinsic versus extrinsic size effect. *Progress in Material Science*, 56:654–724, 2011. xxi, 11, 30, 50

J.R. Greer and W.D. Nix. Size dependence of mechanical properties of gold at the submicron scale. *Applied Physics A*, 80:1625–29, 2005. Erratum. *Applied Physics A*, 90:203, 2008. 24, 29

J.R. Greer and W.D. Nix. Nanoscale gold pillars strengthened through dislocation starvation. *Physcal Review B*, 73:061024, 2006. 16, 24, 26, 29, 99

J.R. Greer, W.C. Oliver, and W.D. Nix. Size dependence of mechanical properties of gold at the micron scale in the absence of strain gradients. *Acta Materialia*, 53:1821–1830, 2005. 24, 26, 27, 29, 83, 94

E. O. Hall. The deformation and ageing of mild steel: III Discussion of results. *Proceedings of the Physical Society: B*, 64:747–753, 1951. 7, 8

N. Hansen. Hall-Petch relation and boundary strengthening. *Scripta Materialia*, 51:801–806, 2004. 8

S. Hart. The measurement of the elastic constants of four alkali halides. *Journal of Physics D: Applied Physics*, 1(10):1277, 1968. xxv, 65, 66, 87

S. Hart. The high-temperature elastic moduli of alkali halides. *Journal of Physics D: Applied Physics*, 10:261–263, 1977. 111, 118

R. Hill. Generalized constitutive relations for incremental deformation of metal crystals by multislip. *Journal of the Mechanics and Physics of Solids*, 14(2): 95, 1966. 59

R. Hill and J.R. Rice. Constitutive analysis of elastic-plastic crystals at arbitrary strains. *Journal of the Mechanics and Physics of Solids*, 20:401–413, 1972. 59

J.W. Hutchinson. Bounds and self-consistent estimates for creep of polycrystalline materials. *Proceedings of the Royal Society: A*, 348:1001–127, 1976. 60

D. Jang and J.R. Greer. Size-induced weakening and grain boundary-assisted deformation in 60 nm-grained Ni nano-pillar. *Scripta Materialia*, 64:77–80, 2011. 34

D. Jang, C. Cai, and J.R. Greer. Influence of homogeneous interfaces on the strength of 500 nm diameter Cu nanopillars. *Nano Letters*, 11:1743–1746, 2011. 34

P.J.M. Janssen, T.H. Keijser, and M.G.D. Geers. An experimental assessment of grain size effects in the uniaxial straining of thin Al sheet with a few grains across the thickness. *Materials Science and Engineering: A*, 419(1-2):238–248, 2006. 8

K.L. Johnson. *Contact Mechanics*. Cambridge University Press., Cambridge, 1985. xxi, 21

W.G. Johnston and J.J. Gilman. Dislocation velocities, dislocation densities and plastic flow in lithium fluoride crystals. *Journal of Applied Physics*, 30:129, 1959. 41, 94, 98

M. Ke, S.A. Hackney, W.W. Milligan, and E.C. Aifantis. Observation and measurement of grain rotation and plastic strain in nanostructured metal thin-films. *Nanostructured Materials*, 5:689–97, 1995. 10

R-M. Keller, S.P. Baker, and E. Arzt. Quantitative analysis of strengthening mechanisms in thin Cu films: Effects of film thickness, grain size, and passivation. *Journal of Materials Research*, 13:1307–1317, 1998. 12

D. Kiener. Size effects in single crystal plasticity of copper under uniaxial loading. *Dissertation*, University of Leoben, 2007. 29

D. Kiener, C. Motz, T. Schberl, M. Jenko, and G. Dehm. Determination of mechanical properties of copper at the micron scale. *Advance Engineering Materials*, 8:1119–1125, 2006. 29, 89

D. Kiener, C. Motz, M. Rester, M. Jenko, and G. Dehm. FIB damage of Cu and possible consequences for miniaturized mechanical tests. *Materials Science and Engineering: A*, 459:262–272, 2007. 26, 95, 123

D. Kiener, W. Grosinger, G. Dehm, and R. Pippan. A further step towards an understanding of size-dependent crystal plasticity: In situ tension experiments of miniaturized single-crystal copper samples. *Acta Materialia*, 56:580–92, 2008. xxi, 14, 15

D. Kiener, C. Motz, and G. Dehm. Micro-compression testing: A critical discussion of experimental constraints. *Materials Science and Engineering: A*, 505: 79–87, 2009. 15

J-Y. Kim, D. Jang, and J.R. Greer. Deformation mechanisms and size effects in BCC metals: W, Mo, Ta, and Nb. *Acta Materialia*, 58:2355–63, 2010. 33, 34

J.Y. Kim, D. Jang, and J.R. Greer. Insight into the deformation behavior of niobium single crystals under uniaxial compression and tension at the nanoscale. *Scripta Materialia*, 61:300–303, 2009. 121

S. Korte and W.J. Clegg. Discussion of the dependence of the effect of size on the yield stress in hard materials studied by microcompression of MgO. *Philosophical Magazine*, 91:1150–1162, 2011. 24, 89, 92, 98, 100, 101, 121, 122, 123, 124, 130

O. Kraft and C.A. Volkert. Size effects on deformation and fatigue of thin films and small structures. *Presented at CAMTEC, Cambridge, UK*, 2006. 29

O. Kraft, P.A. Gruber, R. Monig, and D. Weygand. Plasticity in confined dimensions. *Annual Review of Materials Research*, 40:293–317, 2010. 13, 14, 50

Y.H. Lai, C.J. Lee, Y.T. Cheng, H.S. Chou, H.M. Chen, X.H. Du, C.I. Chang, J.C. Huang, S.R. Jian, J.S.C. Jang, and T.G. Nieh. Bulk and microscale compressive behavior of a Zr-based metallic glass. *Scripta Materialia*, 58:890–93, 2008. 34

C.J. Lee, J.C. Huang, and T.G. Nieh. Sample size effect on the mechanical behavior of Mg65Cu25Gd10 metallic glass. *Applied Physic Letters*, 91:161913, 2007. 25

G. Lee, J-Y. Kim, A.S. Budiman, N. Tamura, M. Kunz, and K. Chen. Fabrication, structure, and mechanical properties of indium nanopillars. *Acta Materialia*, 58:1361–8, 2010. 34, 35

G. Lee, J-Y. Kim, M.J. Burek, J.R. Greer, and T.Y. Tsui. Plastic deformation of indium nanostructures. *Materials Science and Engineering: A*, 528:6112–6120, 2011. 34, 35

S-W. Lee and W.D. Nix. Size dependence of the yield strength of FCC and BCC metallic micropillars with diameters of a few micrometers. *Philosophical Magazine*, 92:1238–1260, 2012. 121, 122, 124

M. Legros, D.S. Gianola, and K.J. Hemker. In situ TEM observations of fast grain-boundary motion in stressed nanocrystalline aluminum films. *Acta Materialia*, 56:3380–93, 2008. 10

J.C.M. Li. Petch relation and grain boundary sources. *Transactions of the Metallurgical Society of AIME*, 227:239–247, 1963. 8

E. Lilleodden. Microcompression study of Mg (0001) single crystal. *Scripta Materialia*, 62:532–5, 2010. 34

Y.Y. Lim and M.M. Chaudhri. The effect of the indenter load on the nanohardness of ductile metals: An experimental study on polycrystalline work-hardened and annealed oxygen-free copper. *Philosophical Magazine*, 79:2979–3000, 1999. 21

J. Llorca and V.M. Orera. Directionally solidified eutectic ceramic oxides. *Progress in Materials Science*, 51:711–809, 2006. xxii, 44, 45, 57, 64

K. Lu, W.D. Wei, and J.T. Wang. Microhardness and fracture properties of nanocrystalline Ni-P alloy. *Scripta Metallurgica*, 24:2319, 1990. 9

A. Ma, F. Roters, and D. Raabe. A dislocation density based constitutive model for crystal plasticity FEM including geometrically necessary dislocations. *Acta Materialia*, 54:2169–2179, 2006. 69

Q. Ma and D.R. Clarke. Size dependence of the hardness of silver single crystals. *Journal of Materials Research*, 10:853–863, 1995. 20

R. Maas, S. Van Petergem, J. Zimmermann, C. Borca, and H. Van Swygenhoven. On the initial microstructure of metallic micropillars. *Scripta Materialia*, 59: 471–474, 2008. 123

N.A. Mara, D. Bhattacharyya, P. Dickerson, R.G. Hoagland, and A. Misra. Deformability of ultrahigh strength 5 nm Cu/Nb nanolayered composites. *Applied Physic Letters*, 92:231901, 2008a. 34

N.A. Mara, D. Bhattacharyya, R.G. Hoagland, and A. Misra. Tensile behavior of 40 nm Cu/Nb nanoscale multilayers. *Scripta Materialia*, 58:874–7, 2008b. 34

J.W. Matthews and A.E. Blakeslee. Defects in epitaxial multilayers. I. Misfit dislocations. *Journal of Crystal Growth*, 27:118–25, 1974. 12

J.W. Matthews and A.E. Blakeslee. Defects in epitaxial multilayers. II. Dislocation pile-ups, threading dislocations, slip lines, and cracks. *Journal of Crystal Growth*, 29:273–80, 1975. 12

M.A. Meyers and K.K. Chawla. *Mechanical Metallurgy: Principles and Applications*. Prentice-Hall, 1984. 9

J. Michler, K. Wasmer, S. Meier, F. Ostlund, and K. Leifer. Plastic deformation of gallium arsenide micropillars under uniaxial compression at room temperature. *Applied Physics Letters*, 90:043123, 2007. 100, 121

P. Moretti, B. Cerruti, and M-C. Miguel. Yielding and irreversible deformation below the microscale: Surface effects and non-mean-field plastic avalanches. *PLoS ONE*, 6:20418, 2011. xxi, 27

B. Moser, K. Wasmer, L. Barbieri, and J. Michler. Strength and fracture of Si micropillars: A new scanning electron microscopy-based micro-compression test. *Journal Material Research*, 22:1004–1011, 2007. 24, 100, 121

C. Motz, T. Schoberl, and R. Pippan. Mechanical properties of microsized copper bending beams machined by the focused ion beam technique. *Acta Materialia*, 53:4269–79, 2005. 26

W.W. Mullins. The effect of thermal grooving on grain boundary motion. *Acta Metallurgica*, 6:414, 1958. 13

E.M. Nadgorny, D.M. Dimiduk, and M.D. Uchic. Size effects in LiF micron-scale single crystals of low dislocation density. *Journal of Materials Research*, 23: 2829–2835, 2008. viii, xii, xxiii, 34, 35, 37, 80, 89, 94, 95, 98, 99, 100, 101, 130

K.S. Ng and A.H.W. Ngan. Breakdown of schmids law in micropillars. *Scripta Materialia*, 59:796–799, 2008a. 88, 89, 111, 121

K.S. Ng and A.H.W. Ngan. Stochastic theory for jerky deformation in small crystal volumes with preexisting dislocations. *Philosophical Magazine*, 88: 677–688, 2008b. 88, 89, 111

K.S. Ng and A.H.W. Ngan. Stochastic nature of plasticity of aluminum micropillars. *Acta Materialia*, 56:1712–1720, 2008c. 24, 29, 88, 89, 111

A.H.W. Ngan. An explanation for the power-law scaling of size effect on strength in micro-specimens. *Scripta Materialia*, 65:978–981, 2011. 98

A.H.W. Ngan and K.S. Ng. Transition from deterministic to stochastic deformation. *Philosophical Magazine*, 90:1937–1954, 2010. 88, 111

G.W. Nieman, J.R. Weertman, and R.W. Siegel. Microhardness of nanocrystalline palladium and copper produced by inert-gas condensation. *Scripta Metallurgica*, 23:2013, 1989. 9

W.D. Nix. Mechanical properties of thin films. *Metallurgical transactions A*, 20: 2217–2245, 1989. 11, 12, 13

W.D. Nix and H. Gao. *Journal of the Mechanics and Physics of Solids*, 46: 411–425, 1998. 21, 22

W.D. Nix, J.R. Greer, G. Feng, and E.T. Lilleodden. Deformation at the nanometer and micrometer length scales: Effects of strain gradients and dislocation starvation. *Thin Solid Films*, 515:3152–3157, 2007. 22

D.M. Norfleet. Sample size effects related to nickel, titanium and nickel-titanium at the micron size scale. *PhD dissertation*, Ohio State University, 2007. 34

D.M. Norfleet, D.M. Dimiduk, S.J. Polasik, M.D. Uchic, and M.J. Mills. Dislocation structures and their relationship to strength in deformed nickel microcrystals. *Acta Materialia*, 56:2988, 2008. 121

W.C. Oliver and G. M. Pharr. Improved technique for determining hardness and elastic modulus using load and displacement sensing indentation experiments. *Journal of Material Research*, 7:1564, 1992. 50

W.C. Oliver and G. M. Pharr. Measurement of hardness and elastic modulus by instrumented indentation: Advances in understanding and refinements to methodology. *Journal of Material Research*, 19:3, 2004. 50

V.M. Orera and A. Larrea. NaCl-assisted growth of micrometer-wide long single crystalline fluoride fibres. *Optical Materials*, 27:1726–1729, 2005. 45

V.M. Orera, A. Larrea, R.I. Merino, M.A. Rebolledo, J.A. Vallés, R. Gotor, and J.I. Pea. Novel photonic materials made from ionic eutectic compounds. *Acta Physica Slovaca*, 55(3):261–269, 2005. 44, 45

J. Orloff. Fundamental limits to imaging resolution for focused ion beams. *Journal of Vacuum Science and Technology B*, 14 (6):3759, 1996. 49

E. Orowan. *Symposium on Internal Stresses*, page 451, 1947. 6

F. Östlund, R. Ghisleni, P.R. Howie, S. Korte, K. Leifer, W.J. Clegg, and J. Michler. Ductile-brittle transition in micropillar compression of GaAs at room temperature. *Philosophical Magazine*, 91:1190–1199, 2011. 88, 89

T.A. Parthasarathy, S.I. Rao, D.M. Dimiduk, M.D. Uchic, and D.R. Trinkle. Contribution to size effect of yield strength from the stochastics of dislocation source lengths in finite samples. *Scripta Materialia*, 56:313–316, 2007. ix, 16, 98, 121, 122, 123

D. Peirce, R.J. Asaro, and A. Needleman. An analysis of nonuniform and localized deformation in ductile single crystals. *Acta Metallurgica*, 30:1087–119, 1982. 60, 61

D. Peirce, R.J. Asaro, and A. Needleman. Material rate dependence and localized deformation in crystalline solids. *Acta Metallurgica*, 31:1951–76, 1983. 60

N.J. Petch. The cleavage strength of polycrystals. *Journal Iron and Steel Institute*, 174:25–28, 1953. 7

J.E. Pitchford. Effects of structure on mechanisms of high temperature plastic deformation in oxide ceramics. *Master's Thesis*, University of Cambridge, 1999. 116

D. Raabe, D. Ma, and F. Roters. Effects of initial orientation, sample geometry and friction on anisotropy and crystallographic orientation changes in single crystal microcompression deformation: A crystal plasticity finite element study. *Acta Materialia*, 55:4567–4583, 2007. 28, 57

R. Rabe, J.M. Breguet, P. Schwaller, S. Stauss, F.J. Haug, J. Patscheider, and J. Michler. Observation of fracture and plastic deformation during indentation and scratching inside the scanning electron microscope. *Thin Solid Films*, 469-470:206–213, 2004. 53, 110

S.I. Rao, D.M. Dimiduk, T.A. Parthasarathy, M.D. Uchic, M. Tang, and C. Woodward. A thermal mechanisms of size-dependent crystal flow gleaned from three-dimensional discrete dislocation simulations. *Acta Materialia*, 56: 3245–3259, 2008. 98, 121

J.R. Rice. Inelastic constitutive relations for solids: An internal variable theory and its application to metal plasticity. *Journal of the Mechanics and Physics of Solids*, 19:433–455, 1971. 59, 60

A. Rinaldi, P. Peralta, C. Friesen, and K. Sieradzki. Sample-size effects in the yield behavior of nanocrystalline nickel. *Acta Materialia*, 56:511–7, 2008. 34

F. Roters, P. Eisenlohr, L. Hantcherli, D.D. Tjahjanto, T.R. Bieler, and D. Raabe. Overview of constitutive laws, kinematics, homogenization and multiscale methods in crystal plasticity finite-element modeling: Theory, experiments, applications. *Acta Materialia*, 58:1152–1211, 2010. 59, 62

P.G. Sanders, J.A. Eastman, and J. R. Weertman. Elastic and tensile behavior of nanocrystalline copper and palladium. *Acta Materialia*, 10:4019, 1997. 9

G.B. Sarma, B. Radhakrishnan, and T. Zacharia. Finite element simulations of cold deformation at the mesoscale. *Computer Material Science*, 12:105–23, 1998. 62

T.A. Schaedler, A.J. Jacobsen, A. Torrents, A.E. Sorensen, J. Lian, J.R. Greer, L. Valdevit, and W.B. Carter. Ultralight metallic microlattices. *Science*, 334: 962–965, 2011. xxi, 3, 4

A.S. Schneider, B.G. Clark, C.P. Frick, P.A. Gruber, and E. Arzt. Effect of orientation and loading rate on compression behavior of small-scale Mo pillars. *Materials Science and Engineering: A*, 508:241, 2009a. 100, 121

A.S. Schneider, D. Kaufmann, B.G. Clark, C.P. Frick, P.A. Gruber, R. Monig, O. Kraft, and E. Arzt. Correlation between critical temperature and strength of small-scale bcc pillars. *Physical Review Letters*, 103:105501, 2009b. xxii, 32, 33, 100, 121

A.S. Schneider, B.G. Clark, C.P. Frick, P.A. Gruber, and E. Arzt. Effect of prestraining on the size effect in molybdenum pillars. *Philosophical Magazine*, 90: 841–849, 2010. 98

A.S. Schneider, C.P. Frick, E. Arzt, W.J. Clegg, and S. Korte. Influence of test temperature on the size effect in molybdenum small-scale compression pillars. *Philosophical Magazine*, 93:331–338, 2013. 121, 124

C.A. Schuh, T.G. Nieh, and T. Yamasaki. Hall-Petch breakdown manifested in abrasive wear resistance of nanocrystalline nickel. *Scripta Materialia*, 46:735, 2002. 9

B.E. Schuster, Q. Wei, T.C. Hufnagel, and K.T. Ramesh. Size-independent strength and deformation mode in compression of a Pd-based metallic glass. *Acta Materialia*, 56:5091–100, 2008. 34

F. Seitz. *Modern Theory of Solids*. McGraw-Hill, New York, 1940. 40

P.A. Shade, R. Wheeler, Y.S. Choi, M.D. Uchic, D.M. Dimiduk, and H.L. Fraser. A combined experimental and simulation study to examine lateral constraint effects on microcompression of single-slip oriented single crystals. *Acta Materialia*, 57:4580–4587, 2009. 28, 64

Z.W. Shan, R.K. Mishra, S.A. Syed Asif, O.L. Warren, and A.M. Minor. Mechanical annealing and source-limited deformation in submicrometre-diameter Ni crystals. *Nature Materials*, 7:115–119, 2007. 24, 26, 29, 95

S. Shim, H. Bei, M.K. Miller, G.M. Pharr, and E.P. George. Effects of focused ion beam milling on the compressive behaviour of directionally solidified micropillars and the nanoindentation response of an electropolished surface. *Acta Materialia*, 57:503–510, 2009. 24, 92, 98

I. Sneddon. The relation between load and penetration in the axisymmetric boussinesq problem for a punch of arbitrary profile. *International Journal of Engineering Science*, 3:47–57, 1965. 83

I.J. Spary, A.J. Bushby, and N.J. Jennet. On the indentation size effect in spherical indentation. *Philosophical Magazine*, 86:5581–5593, 2006. 22

J.S. Stölken and A.G. Evans. A microbend test method for measuring the plasticity length scale. *Acta Materialia*, 46:5109–5115, 1998. 18

Q. Sun, Q. Guo, X. Liao, J.R. Greer, and J. Sun. Size effects in strength and plasticity of single-crystalline titanium micropillars with prismatic slip orientation. *Scripta Materialia*, 65:473–476, 2011. 34, 35

H. Tang, K. Schwarz, and H.D. Espinosa. Dislocation-source shutdown and the plastic behavior of single-crystal micropillars. *Physical Review Letters*, 100: 185503, 2008. 121

G.I. Taylor. The mechanism of plastic deformation of crystals. Part I. Theoretical. *Proceedings of Royal Society: A*, 145:362–387, 1934. 7, 16, 18

this work. 100, 121

C.V. Thompson. Grain growth in thin films. *Annual Review of Materials Science*, 20:245, 1990. 13

M. D. Uchic, P. A. Shade, and D.M. Dimiduk. Plasticity of micrometer-scale single crystals in compression. *Annual Review of Materials Research*, 39:361–86, 2009. xxii, 14, 30, 31, 50, 100, 121

M.D. Uchic and D.M. Dimiduk. A methodology to investigate size scale effects in crystalline plasticity using uniaxial compression testing. *Materials Science and Engineering: A*, 400:268–278, 2005. 24, 29, 89

M.D. Uchic, D.M. Dimiduk, J.N. Florando, and W.D. Nix. Exploring specimen size effects in plastic deformation of $Ni_3(AlTa)$. *Materials Research Society Symposium Proceedings*, 753:BB1.4.1–6, 2003. 24

M.D. Uchic, D.M. Dimiduk, J.N. Florando, and W.D. Nix. Sample dimensions influence strength and crystal plasticity. *Science*, 305:986–989, 2004. xxi, 2, 3, 14, 23, 24, 29, 94, 99

H. Van Swygenhoven and P.M. Derlet. Grain-boundary sliding in nanocrystalline fcc metals. *Physical Review B*, 64:224105, 2001. 10

H. Van Swygenhoven, P.M. Derlet, and A. Hasnaoui. Atomic mechanism for dislocation emission from nanosized grain boundaries. *Physical Review B*, 66: 024101, 2002. 10

M.R. VanLandingham. Review of instrumented indentation. *Journal of Research of the National Institute of Standards and Technology*, 108:249–265, 2003. 50

E. Voce. The relationship between stress and strain for homogeneous deformation. *Journal of the Institute of Metals*, 74:537–62, 1948. 62

C.A. Volkert and E.T. Lilleodden. Size effects in the deformation of sub-micron Au columns. *Philosophical Magazine*, 86:5567–5579, 2006. 24, 29, 33, 94, 99

C.A. Volkert and A.M. Minor. Focused ion beam microscopy and micromachining. *MRS Bulletin*, 32:389–95, 2007. 25

C.A. Volkert, A. Donohue, and F. Spaepen. Effect of sample size on deformation in amorphous metals. *Journal of Applied Physics*, 103:0883539, 2008. 34

Y.B. Wang, B.Q. Li, M.L. Sui, and S.X. Mao. Deformation-induced grain rotation and growth in nanocrystalline Ni. *Applied Physics Letters*, 92:011903, 2008. 10

J.M. Wheeler, P. Brodard, and J. Michler. Elevated temperature, in situ indentation with calibrated contact temperatures. *Philosophical Magazine*, 92: 25–27, 2012. 108, 110

J.M. Wheeler, C. Niederberger, C. Tessarek, S. Christiansen, and J. Michler. Extraction of plasticity parameters of GaN with high temperature, in situ micro-compression. *International Journal of Plasticity*, 40:140–151, 2013. 53, 110

R.E.A. Williams, A. Genc, D. Huber, and H.L. Fraser. Sample surface preparation for traditional EBSD collection and 3D EBSD collection. *Microscopy and Microanalysis*, 16:706–707, 2010. 26

V. Yamakov, D. Wolf, S.R. Phillpot, and H. Gleiter. Grain-boundary diffusion creep in nanocrystalline palladium by molecular dynamics simulation. *Acta Materialia*, 50:61–73, 2002. 10

F. Yang, L. Peng, and K. Okazaki. Effect of the indenter size on the indentation of aluminum. *Materials Characterization*, 57:321–325, 2006. 22

J. Ye, R.K. Mishra, A.K. Sachdev, and A.M. Minor. In situ TEM compression testing of Mg and Mg-0.2 wt.% Ce single crystals. *Scripta Materialia*, 64: 292–295, 2011. 34

W.M. Yin and S.H. Whang. The creep and fracture in nanostructured metals and alloys. *Journal of the Minerals Metals and Materials Society*, 57:63–70, 2005. 10

J. Yu, J. Liu, J. Zhang, and J. Wu. TEM investigation of FIB induced damages in preparation of metal material TEM specimens by FIB. *Materials Letters*, 60:206–9, 2006. 26

Q. Yu, Z-W. Shan, J. Li, X. Huang, L. Xiao, J. Sun, and E. Ma. Strong crystal size effect on deformation twinning. *Nature*, 463:335–8, 2010. 34, 35

H. Zhang, B. Schuster, Q. Wei, and K. Ramesh. The design of accurate micro-compression experiments. *Scripta Materialia*, 54:181–186, 2006. 24, 28, 69, 92

T.Y. Zhang and W.H. Xu. Surface effects on nanoindentation. *Journal of Materials Research*, 17:1715–1720, 2002. 22

Y. Zhang and A.L. Greer. Thickness of shear bands in metallic glasses. *Applied Physics Letters*, 89:071907, 2006. 34

Z. Zong and W.O. Soboyejo. Indentation size effects in face centered cubic single crystal thin films. *Materials Science and Engineering: A*, 404:281–290, 2005. 22

Dissemination of Results

Publications

R. Soler, J.M. Wheeler, H-J. Chang, J. Segurado, J. Michler, J. Llorca, and J.M. Molina-Aldereguia. Understanding size effects on the strength of single crystals through high temperature micropillar compression. *Submitted*.

R. Soler, J. M. Molina-Aldereguia, J. Segurado, and J. Llorca. Effect of misorientation on the compression of highly anisotropic single-crystal micropillars. *Advance Engineering Materials*, 14(11):1004-1008, 2012. Doi:10.1002/adem.201200019.

R. Soler, J.M. Molina-Aldereguia, J. Segurado, J. Llorca, R. Merino, and V. Orera. Micropillar compression of LiF [111] single crystals: effect of size, ion irradiation and misorientation. *International Journal of Plasticity*, 36:50-63, 2012. Doi: 10.1016/j.ijplas.2012.03.005.

Communications

R. Soler, J.M. Wheeler, H-J. Chang, J. Segurado, J. Michler, J. Llorca, and J.M. Molina-Aldereguia. Temperature-dependent size effects in LiF [111] single crystals. *Dislocation-based Plasticity Symposium*, February 24-27, 2014, Schöntal, Germany. (Poster presentation)

R. Soler, J.M. Wheeler, H-J. Chang, J. Segurado, J. Michler, J. Llorca, and J.M. Molina-Aldereguia. Temperature-dependent size effects in LiF [111] single crystals. *Nanomechanical Testing in Materials Research and Development IV, ECI*, October 7-11, 2013, Olhao, Portugal. (Poster presentation)

R. Soler, J.M. Wheeler, H-J. Chang, J. Segurado, J. Michler, J. Llorca, and J.M. Molina-Aldereguia. Temperature-dependent size effects in LiF [111] single crystals. *European Congress and Exhibition on Advanced Materials and Processes, Euromat*, September 8-13, 2013, Seville, Spain. (Oral presentation)

J.M. Molina-Aldereguia, R. Soler, J. Segurado, J. Llorca, R. Merino, and V. Orera. Effect of ion irradiation on the micropillar compression of LiF single crystals. *Nanomechanical Testing in Materials Research and Development III, ECI*, October 9-14, 2011, Lanzarote, Canary Islands, Spain. (Invited lecture)

J.M. Molina-Aldereguia, R. Soler, J. Segurado, and J. Llorca. Size effects in micropillar compression of LiF single crystals fabricated without exposure to ion irradiation. *Eropean Congress and Exhibition on Advanced Materials and Processes, Euromat*, September 12-15, 2011, Montpellier, France. (Oral presentation)

R. Soler, J.M. Molina-Aldereguia, J. Segurado, J. Llorca, R. Merino, and V. Orera. Micropillar compression of LiF [111] single crystals: effect of size, ion irradiation and misorientation. *Congreso nacional de materiales, Iberomat XII*, May 29-31, 2012, Alicante, Spain. (Oral presentation)